FABRICATION OF ELECTRONIC DEVICES FOR ENERGY STORAGE AND HARVEST USING MICROFIBRILLATED CELLULOSE

A Dissertation
Presented to
The Academic Faculty

By

Xiaodan Zhang

In Partial Fulfillment
of the Requirements for the Degree
Doctor of Philosophy in the
School of Materials Science and Engineering

Georgia Institute of Technology
December 2014

FABRICATION OF ELECTRONIC DEVICES FOR ENERGY STORAGE AND HARVEST USING MICROFIBRILLATED CELLULOSE

Committee members:

Dr. Yulin Deng, Advisor
School of Chemical & Biomolecular Engineering
Georgia Institute of Technology

Dr. Youjiang Wang, Co-Advisor
School of Materials Science & Engineering
Georgia Institute of Technology

Dr. Preet Singh
School of Materials Science & Engineering
Georgia Institute of Technology

Dr. James Carson Meredith
School of Chemical & Biomolecular Engineering
Georgia Institute of Technology

Dr. Zhiqun Lin
School of Materials Science & Engineering
Georgia Institute of Technology

Date Approved: 11/5/2014

To my love parents, Ping Zhang & Yan Wang, for their love and support

ACKNOWLEDGEMENTS

Thanks to the encouragement and support from all my mentors, family members and friends, I was able to complete my dissertation and face all the challenges with courage and faith in the past five years. First of all, I would like to thank my thesis advisor, Professor Yulin Deng. He set up a life model for me for his remarkable attitude of diligence, strictness and curiosity. He inspired me to develop a critical way of thinking about problems, which will benefit me for a lifetime. Also, I am grateful to my co-advisor Dr. Youjiang Wang, who offered me great help and precious guidance for my study. I would not be able to make it this far without his help. Thank Professor Zhiqun Lin for sharing his lab equipment with me and offering significant help for modifying my publications. I would also like to acknowledge my other thesis committee members, Professor Preet Singh, Professor Carson Meredith, for providing intelligent opinions towards my researches. I sincerely appreciate the Renewable Bioproducts Institute for providing me with financial support for making my study at Georgia Institute of Technology possible.

I would like to thank several of my former and current group members that I've worked with, including Dr. Zeshan Hu, Dr. Wei Zhang, Rui Zhao, Wei Mu, Wei Liu, Mike Roy, Sudhir Sharmar, Junli Zhou, Zhe Zhang. I would also like to recognize all of the members of the Yulin Deng group from 2009-2014, who have provided me with strong support and advice continuously. I would like to acknowledge my undergraduate student,

Bo Chen, who showed great enthusiasm and with whom I grew up and developed more deep understanding towards the project.

Lastly, I want to show my great gratitude to my dear parents, who taught me how to think and to be a self-motivated person and who showed unconditional love to me no matter if I was in difficulty or success. My parents guided me to the right and optimistic direction and are my life motivation to be an upright and excellent person to make them proud.

Table of content

LIST OF TABLES

LIST OF FIGURES

LIST OF ABBRAVIATIONS

AC	Activated Carbon
AFM	Atomic Force Microscope
BET	Brunauer-Emmett-Teller
CNT	Carbon Nanotubes
C_m	Specific Mass Capacitance
C_s	Specific Areal Capacitance
CV	Cyclic Voltammetry
CVD	Chemical Vapor Deposition
DI water	Deionized Water
DSSCs	Dye Sensitized Solar Cells
EDLC	Electric Double Layer Capacitors
ERS	Equivalent Series Resistance
EIS	Electrochemical Impedance Spectroscopy
FF	Fill Factor
GO	Graphene Oxide
IPCE	Incident Photon-to-Current Efficiency
I-V curve	Current-Voltage Curve
ITO	Indium Tin Oxide
J_{sc}	Short Circuit Current Density
MWCNT	Multi-Walled Carbon Nanotubes
NP	Nanoparticles

PANI	Polyaniline
PDMS	Polydimethysiloxane
PEO	Polyethylene Oxide
PVA	Polyvinyl Alcohol
PVDF	Polyvinylidene Fluoride
PPY	Polypyrrole
SEM	Scanning Electron Microscope
SPEs	Solid-Polymer Electrolytes
SSA	Specific Surface Area
SSM	Stainless Steel Mesh
SWCNT	Single-Walled Carbon Nanotubes
UV-vis	Ultraviolet–visible Spectroscopy
V_{oc}	Open Circuit Voltage
XRD	X-Ray Diffraction

SUMMARY

Cellulose, as the most abundant biopolymer in the world and the main component of paper, is a polysaccharide consisting of thousands of β-linked glucose unit. Modern society requires electronic devices to be more flexible and environmental friendly, which makes cellulose as a good candidate for next generation of green electronics. However, lots of researches employed "paper-like" petroleum-based polymers to fabricate electronics rather than using real cellulose paper. Cellulose, as representatives of environmental friendly materials, caught into people's attention because of their sustainable nature, ease of functionality, flexibility and tunable surface properties, etc. There are some general challenges about using cellulose for electronics, such as its non-conductivity, porosity and roughness, but these features can be taken advantages of on certain occasions.

This thesis focuses on the study of cellulose-based electronic devices by chemical or physical modification of microfibrillated cellulose (MFC). Particularly, three electronic devices were fabricated, including ionic diodes, electric double layer supercapacitors, pseudocapacitors. In addition, a rational design of dye-sensitized solar cell was investigated, although it was not directly cellulose-based, it led the way to the next generation of cellulose-based solar cells.

(1) Flexible and transparent paper-based ionic diodes

For the first time, paper-based ionic diodes (PIDs) were fabricated to control the electrical current to flow unidirectionally, in the principles of using the electrostatic force to control the ionic movement. PIDs were made by combining together two oppositely

charged microfibrillated cellulose sublayers. The asymmetric charge distribution between the two sublayers helped selectively transport cations and anions under positive and negative bias. The current rectification ratio (the ratio of forward current to backward current under the same voltage but different direction) was around 15 at ±5 V and exhibited good repeatability at room temperature. The PIDs made by MFC had many advantages. First, the cost of PIDs were much lower than inorganic-based devices and fossil-based polymeric membranes. Second, the cellulose-based nature made it more environmental-friendly. Third, PIDs had much better mechanical strength than hydrogel-based p-n junctions.

(2) Solid-state and flexible multi-walled carbon nanotubes(MWCNTs)/MFC based electric double layer supercapacitors

Flexible and free-standing paper-based supercapacitors were fabricated for energy storage. The paper-based supercapacitors were designed using MFC as supporting skeleton for both electrode sheets and separator sheets, solid electrolyte (polyethylene oxide and lithium chloride) as electrolyte and carbon nanotubes as the active electrode materials. The specific areal capacitance was calculated to be 154.5 mF/cm^2 at 20mV/s from cyclic voltammetry, which was higher than most of the other solid-state supercapacitors normally ranged from a few to 109 mF/cm^2. The paper-based supercapacitors were superior to conventional supercapacitors in terms of tunable electrode sheet thickness for adjustable areal capacitance. Usually for conventional supercapacitors, the electrode materials, such as carbon materials or conductively polymers, were simply casted or brushed-on on substrates, thus would be easily peeled off. The paper-based supercapacitors employed MFC as a good film-forming material, which prevented this from happening. In addition,

the porous nature of MFC was beneficial for the ionic transportation and for the absorption of electrode materials. The free-standing paper-based supercapacitors had great advantages when it came to packaging and could be stacked together to get high capacitance without taking much space.

(3) Solid-state and flexible polyaniline/silver/MFC aerogel pseudosupercapcitors

Flexible and solid-state MFC aerogel based supercapacitros were fabricated with employing MFC aerogel as supporting materials, polyaniline as electrode materials, silver particles as conducting agents and polyvinyl alcohol/phosphoric acid as solid electrolyte. The specific areal capacitance was calculated to be 176mF/cm^2 at 10mV/s from cyclic voltammetry, which was significantly higher than most flexible supercapacitors reported in literatures. Due to the high specific surface of MFC aerogel, large amount of polyaniline could be held in its network for substantial charge storage. In addition, the design of multiple-synthesis of Ag particles onto MFC aerogel had greatly boosted the conductivity of the supercapacitors, thus overcame the most challenging problem for paper-based electronics, which was conductivity. The MFC aerogel supercapacitors were also solid-state and flexible, which great facilitated the packaging of the devices.

(4) Hybrid dye-sensitized solar cells (DSSC) composed with double photoanodes

Parallel-connected titanium dioxide dye-sensitized solar cells were fabricated to harvest a broader range of light in the solar spectrum. The hybrid solar cells consisted of two photoanodes and one counter electrode. One photoanode was based on dye N719 sensitized TiO_2 on ITO glass and the other photoanode was based on dye N749 sensitized TiO_2 on Ni/Ti mesh. The two dyes absorbed the solar energy in a complementary range, which greatly improved the power conversion efficiency of the hybrid solar cells. The

power conversion efficiency of the hybrid cell could reach to 6.6%, which was significantly higher than that of the single cell. Moreover, the porous nature of the second photoanode substrate, Ni/Ti mesh, enabled the crafting of the hybrid cells in a single compartment, by allowing the electrolyte to penetrate the whole device, which effectively avoided the use of interconnecting layers for conventional hybrid/tandem solar cells. These hybrid dye-sensitized solar cells provided valuable insight for exploring the possibility of paper-based solar cells, because the structure of Ni foam was very similar to that of porous MFC network. If Ni foam photoanode were successfully applied on dye-sensitized solar cells, this technique would be very promising to be transferred to fabricate MFC based dye-sensitized solar cells.

In sum, environmental-friendly, low-cost cellulose based or potential cellulose based green electronics were fabricated with excellent performances. As pioneering work for biopolymer-based electronics devices, this thesis made significant contribution in the following aspects: (i) rationally leveled the high specific surface area of micro/nano-sized MFC to serve as ionic gateways and systematically investigated how the surface charge density, the thickness and the specific surface area influenced the ionic transportation in MFC and further affected the device performances; (ii) Provided inspiring methods to solve one of the major problems for paper-based electronics, which was the conductivity, either by chemical or physical methods; (iii) Aimed to solve the packaging and flexibility problems of the current electronic devices, by replacing the liquid-based systems with their solid-state counterparts, meanwhile maintaining the excellent performances. (iv) Explored novel designs and fabrication methods of the electronic devices to enhance their properties.

Chapter 1

LITERATURE REVIEW

1.1 Introduction of cellulose

1.1.1 Structure of cellulose

Cellulose is the most abundant bipolymer and finds applications in various areas, including composite materials, textiles, drug delivery systems, personal care, etc [1-5]. In general, cellulose is a fibrous, strong, water-insoluble, hydrophilic substance that plays an important role in the structure of green plant cell walls. Since it was first characterized in 1838[6], this inexpensive, biodegradable and renewable resource have received a great deal of attention for its physical properties and chemical reactivity. The polymeric structure of cellulose was demonstrated in Figure 1.1. Figure 1.1 shows that cellulose is generated from repeating β-D-anhydroglucopyranose units that are joined together covalently through acetal groups between the equatorial group of the C4 and C1 atom. Each cellulose chain exhibits a directional asymmetry with respect to its molecular axis: one end is chemically reductive (i.e., a hemiacetal unit) and the other end has a pendant hydroxyl group, which is non-reductive. The number of glucose units or the degree of polymerization (DP) of cellulose can reach up to 20000. The DP varies by the sources of cellulose.

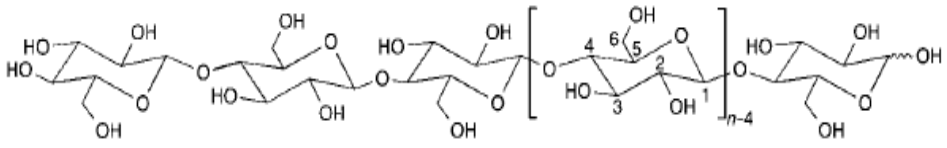

Figure 1.1 Molecular structure of cellulose

Cellulose has a hierarchical structure. The cellulose microfibrils are the basic structural unit of the plant cell walls; each microfibril can be considered as a string of cellulose crystallites, linked along the chain axis by amorphous domains (see Figure 1.2). The microfibrils are glued by other polymers like lignin and hemicelluloses and built up further to form lignocellulosic fibers. The crystalline part of cellulose is almost defect-free, which gives cellulose crystallites great mechanical properties. The theoretical estimation of Young's modulus for cellulose crystallites is about 167.5 GPa by Tashiro and Kobayashi[7]. While experimentally, Sakurada et al. studied the crystal deformation of cellulose I using highly oriented fibers of bleached ramie and reported a value of 137GPa[8]. The elastic Young's modulus value of cellulose was reported by Sturcova et al., which was around 143GPa by Raman spectroscopy technique. The elastic Young's modulus of the single microbril was reported to be around 150GPa[9].

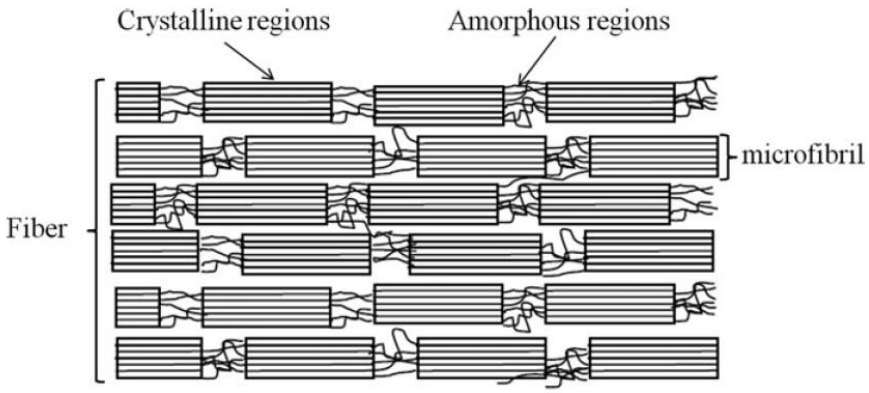

Figure 1.2 Schematic diagram of the physical structure of a semicrystalline cellulose fiber[10].

1.1.2 The molecular bonding and morphology of cellulose

Both types of intramolecular hydrogen bonding and intermolecular hydrogen bonding occur in cellulose, as shown in Figure 1.3 and Figure 1.4. The intramolecular

hydrogen bonding is illustrated in Figure 1.3. All β-D-anhydroglucopyranose rings adopt 4C1 chair conformation, as a result, the hydroxyl groups are located in the equatorial plane, while the hydrogen atoms are in the axial position. This structure is stabilized by an intra-molecular hydrogen bond network extending from the O(3')-H hydroxyl to the O(5) ring oxygen of the next nit across the glyosidic linkage and from the O(2)-H hydroxyl to the O(6') hydroxyl of the next residue[11]. Intermolecular hydrogen bonding happens between the hydroxyl groups on different chains of cellulose as shown in Figure 1.4. The hydrogen bonding affects the morphology and properties of cellulose dramatically.

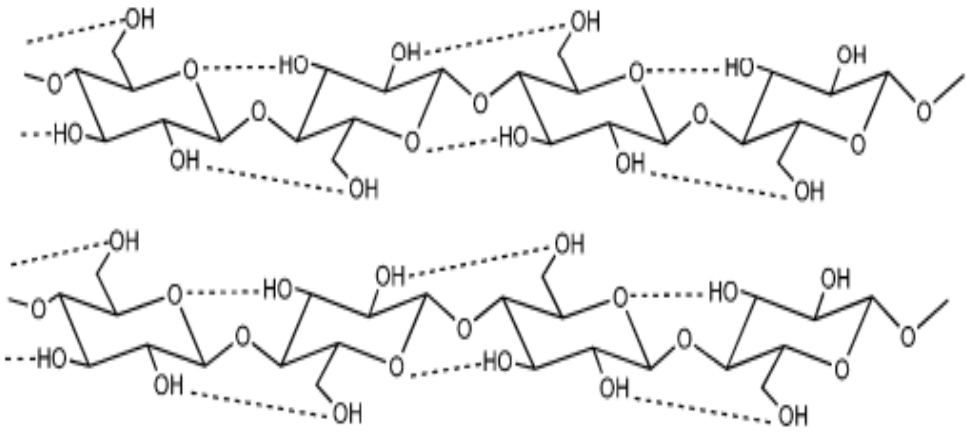

Figure 1.3 Intramolecular hydrogen-bonding network in a representative cellulose structure[12]

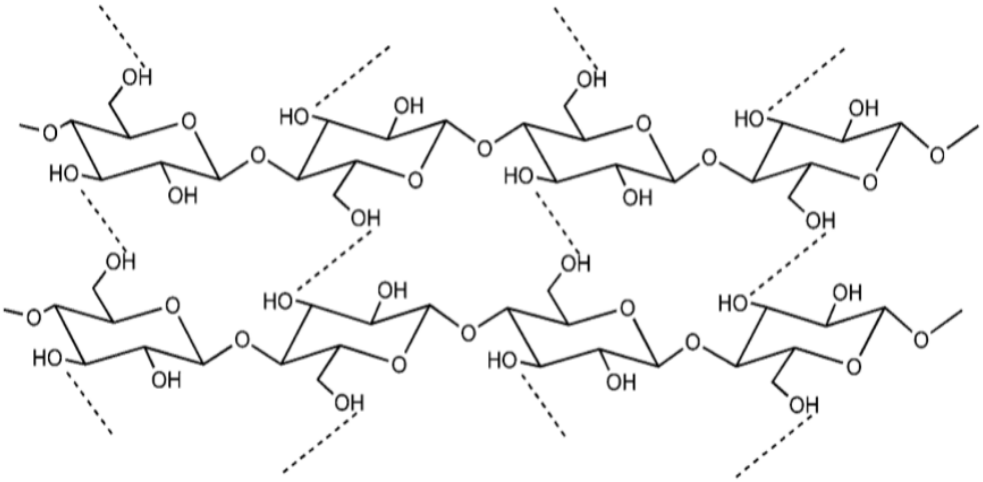

Figure 1.4 Intermolecular hydrogen-bonding network in a representative cellulose structure[12]

The hydrogen-bonded network and molecular orientation in cellulose can vary greatly, which can lead to polymorphs or allomorphs, depending on the particular source, methods of extraction, or treatment[7, 13]. Native cellulose is mostly in the form of cellulose I, termed Iα and Iβ, which was proved in 1984 by cross polarization magic spinning(CP-MAS)[7]. In these types of cellulose, the chains within the unit cell are in a parallel conformation. Special treatments of native cellulose result in other forms of cellulose, namely cellulose II, III, IV. Conversion from one form of cellulose to another form can be realized.

1.1.3 Reactivity of cellulose

Cellulose is a reactive chemical due to the presence of three hydroxyl groups in each glucose residue. The degree of substitution (DS) is defined as the average number of hydroxyl groups in an anhydroglucose units which have been substituted. Thus, the maximum DS for cellulose is 3. However, the reactions of the cellulose cannot simply be

regarded as trihydric alcohol reactions. This is because that cellulose is fibrous-like and has high molecular weight. In most cases, the hydroxyl groups at the 2 and 3 positions are less reactive than the ones at 6 position. In addition, the reactions of cellulose nearly always take place under heterogeneous conditions. That is because that only a few solvents can dissolve cellulose, so that in most cases, cellulose is suspended in the liquid medium. Moreover, different domains in cellulose, say amorphous domains or crystalline domains, have different accessibilities to the same reagent.

Many factors can influence the reactivity of cellulose, including the constitution of cellulose molecules, the morphology of cellulose fibers, the degree of crystallinity, the interfibrillary bonds, the voids and capillaries. However, the reactivity of cellulose can be tuned by the following procedures: (i) open surface cannulae, internal pores and cavities; (ii) disintegrate the fiber aggregates to increase the surface area of cellulose; (iii) disturbe the crystallinity of cellulose; (iv) alter the crystal modification to interrupt the hydrogen bonds in cellulose, exposing more reactive hydroxyl groups.

Accessibility of cellulose can be improved by several ways, including swelling, solvent exchange, inclusion, degradation and mechanical grinding. Out of these methods, swelling is the most often used method to open the structure of cellulose. Cellulose swelling can happen in acid, base, salts as wells as organic solvents. These agents can penetrate into highly ordered cellulose regions, breaking interaction between chains and fibers. Aqueous sodium hydroxide is the most common used swelling agent for cellulose. After alkali treatment, the cellulose remains fibrillar but the disorder increases. In addition, the crystalline type of cellulose can be altered from cellulose I to cellulose II.

The reactivity of cellulose is very diverse, hereby, the grafting process to produce functional cellulose is highlighted for the purpose of further fabrication of electronic devices.

The grafting of the cellulose can always be achieved by covalently bonding small molecules or copolymers onto the surface of cellulose to impart specific properties,

without changing its intrinsic properties. The grafting processes of small molecules or copolymers onto cellulose can be generally classified into three major methods: (i) free radical polymerization, (ii) ionic and ring opening polymerization and (iii) living radical polymerization.

The methods of cellulose grafting can also been categorized into three approaches, “grafting-to” the cellulose, “grafting-from” the cellulose, and “grafting-through” the cellulose.

The “grafting-to” approach. An end functional group of copolymers reacts with a functional group on cellulose. The “grafting-to” approach is illustrated in Figure 1.5.

The “grafting-from” approach. The growth of polymer chains initiates from the sites on the cellulose backbone. The “grafting-from” approach is illustrated in Figure 1.6.

The “grafting-through” approach. A macromonomer is copolymerized with a low molecular weight co-monomer as illustrated in Figure 1.7.

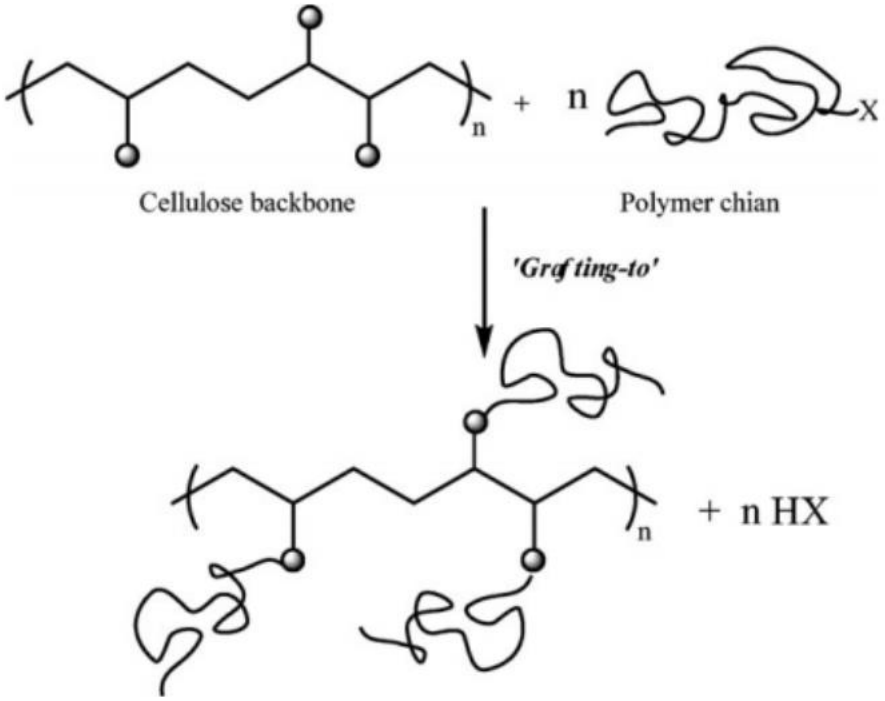

Figure 1.5 A schematic representation of the "grafting-to" approach[12]

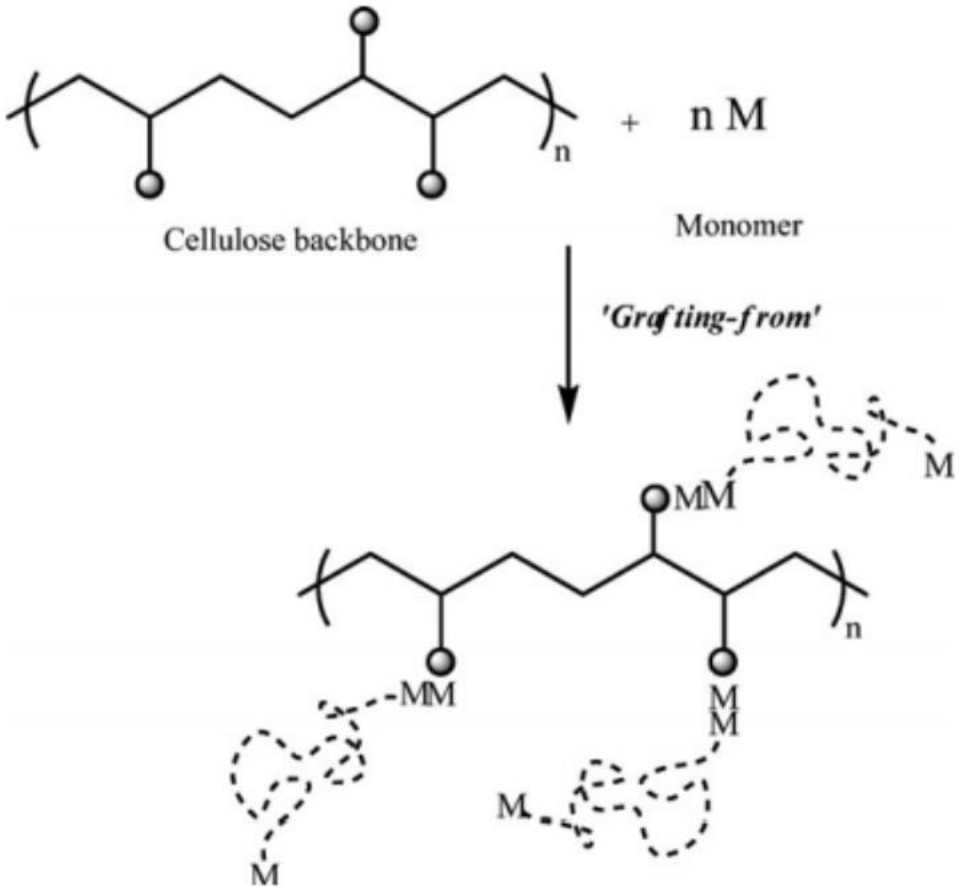

Figure 1.6 A schematic representation of the "grafting-from" approach[12]

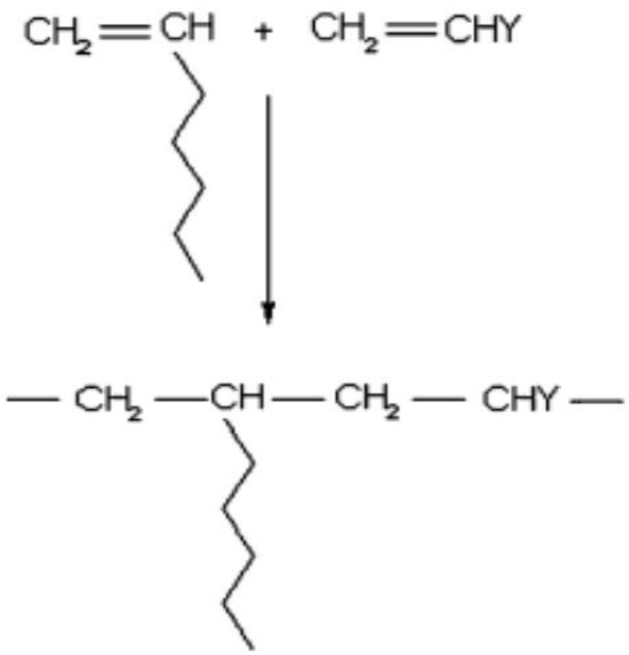

Figure 1.7 The "grafting-through" approach[12]

Among these approaches of grafting, the “grafting-from” approach is the most commonly used procedure and will be the main approach used in this thesis for the modification of cellulose. One of the major advantages of this approach is that a high graft density can be achieved due to the easy access of the reactive groups of the grafting molecules.

In sum, the hydroxyl groups provide reaction sites for modification of cellulose, which can help realize functionality of cellulose. The reactivity of cellulose can be affected by multiple factors. Grafting of small molecules or copolymers are effective ways to achieve desired surface properties of cellulose without destroying its intrinsic properties.

1.2 Introduction of microfibrillated cellulose (MFC)

1.2.1 Structure of MFC

Microfibrillated cellulose (MFC) can be also termed as cellulose microfibril, microfibrillar cellulose. Attention on MFC has been soaring recently[14-16]. The micro/nano-size effect of MFC and its ability to form a highly entangled micro/nano porous network enables MFC to be applied in new high-valued applications. In addition, MFC is one of the excellent reinforcement fillers for various polymeric substrates. New sources, new prepare routes and new pre-, post- treatments of MFC have been extensively studied in order to produce MFC materials on an industrial level[10, 16].

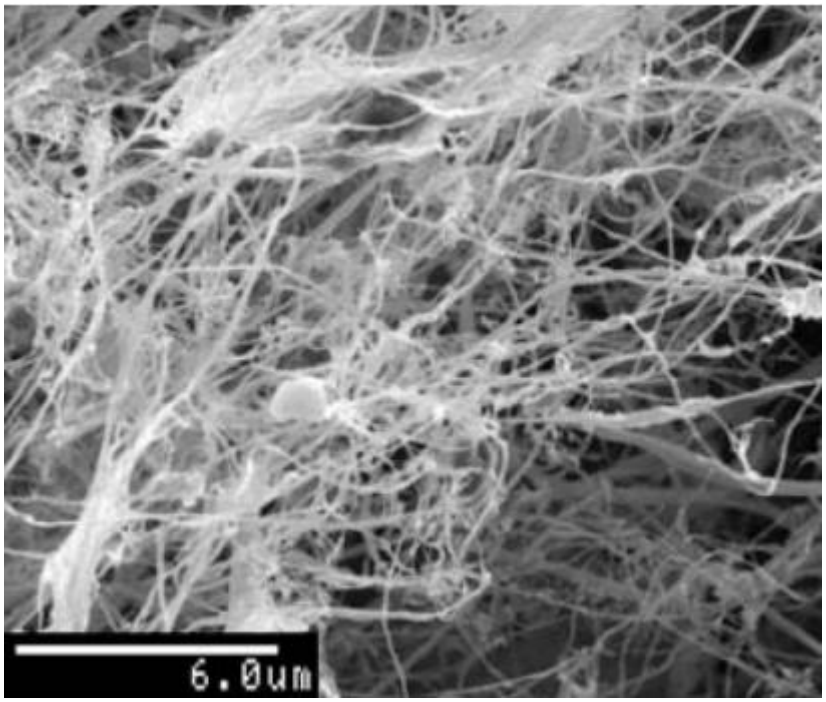

Figure 1.8 Scanning electron microscopy of MFC[13].

MFC can be considered as a cellulosic material, made of fibrillated high-volume cellulose, moderately degraded and greatly expanded in surface area, normally produced by a homogenization process. The ratio of L/D of MFC is very high, which makes the microfibrils very easy to get entangled. MFC can readily form a rigid network. The diameters of MFC are usually ranged tens of nanometers and length ranged several

micrometers. MFC consists of both amorphous and crystalline parts and exhibits a web-like morphology [17]. The morphology of MFC is shown in Figure 2.5.

1.2.2 Sources and preparation methods of MFC

Different cellulosic materials can serve as sources of MFC. Wood is the most common source of MFC in the industrial perspective, and is thus the main source for MFC. Bleached kraft pulp is usually the starting material for production of MFC[18-21], followed by bleached sulfite pulp[22, 23].

MFC is obtained by the mechanical disintegration of cellulosic material without chemical hydrolysis. Turbak et al. first produced MFC by making wood fiber suspension to go through a narrow gap under high pressure for several times, yielded a viscous gel. This marked the emergence of the rising researches focusing on either optimizing the mechanical procedure or analyzing the properties of this newly found material [24-26].

The preparation methods of MFC include homogenizer, microfluidizer, grinding, cryocrushing and electrospinning. The method used in our research group is homogenizer. In the homogenizing process, the cellulose slurry is pumped at high pressure and run through a spring-loaded valve assembly. The valve opens and closes quickly and continuously, so the slurry is pushed through a small hole under high shear force. The shear force exerted on the fibers yields a high degree of fibrillation. The slurry can be fed into the homogenizer several times to get the desired fibrillated fibers. Other alternative ways are available for MFC production, we will not state each of them in details. Spence et al. performed a very precise study of physical properties of MFC prepared by different procedures, such as a homogenizer, a microfluidizer and a grinder[16]. They concluded that MFC produced by a homogenizer had the highest specific surface area and lowest water vapor transmission. Meanwhile, MFC produced by a microfluidizer and a grinder had superior optical and water interaction properties, which rendered them a good candidate for packaging. However, among each of the

mentioned mechanical treatment, the energy consumption is very high. Eriksen et al. determined, for examples, the energy consumed by a homogenizer could reach up as 70,000kWh/t[27]. As a result, how to reduce the energy consumption for MFC production has become a priority. The combination of pre-treatments and mechanical treatments were suggested by researches. Pretreatment can help to make the fibers less stiff and cohesive, thus reduce the energy needed for fibrillation. The most comment pre-treatments include enzymatic pre-treatment, TEMPO mediated oxidation pre-treatment, carboxymethylation and acetylation. The principles of the treatments are: (i) weaken the hydrogen bonds, and or (ii) add a repulsive charge, and or (iii) lower the DP or breakdown the amorphous link between MFC[28].

1.2.3 Modification of MFC to achieve desired functionalities

The surface modification of MFC is of great interest in order to realize new functionality of MFC. MFC is hydrophilic, thus cannot be well dispersed in most non-polar polymer media. Its aqueous slurry is gel-like at low concentration and it will form films upon drying. The surface of MFC can be modified by two ways: (i) by physical absorption of molecules or macromolecules onto MFC surface; (ii) by chemically bonding the grafting agent onto the MFC surface. By the physical method, the surface of MFC can be tuned by surfactant or polyelectrolyte adsorption. The surfactants used are usually amphiphilic organic compounds with hydrophobic groups on one end and hydrophilic groups on the other end. For example, the TEMPO-MFC with anionic surface can be modified with a cationic surfactant, say cetyltrimethylammonium bromide (CTAB) aqueous solution. Polyelectrolyte solution is also common for modification of surface properties of MFC. Martins et al. designed a layer-by layer structure by absorbing polyelectrolyte onto MFC to attach Ag particles onto paper for anti-bacteria use[29]. By alternatively absorbing cationic polyelectrolyte and anionic polyelectrolyte onto MFC, Ag particles were able to attach onto MFC. Physical adsorption is an effective method to

change the hydrophilicity of MFC, however, this procedure can induce migrations of physically absorbed moieties. As a result, chemically modification of MFC also developed by covalently bonding molecules onto its surface. Because of the abundance of hydroxyl groups at the surface of MFC, numerous modifications can be achieved, including esterification, etherification, oxidation, silylation, polymer grafting, etc. All the chemical functionalizations have been done to (i) introduce stable negative or positive electrostatic charges on the surface of cellulose to obtain better dispersion and (ii) adjust the surface characteristics of cellulose to improve compatibility, especially when used in nonpolar or hydrophobic matrix to make nanocomposites. For example, esterification process could change the properties from hydrophilicity to hydrophobicity. Acetylation on MFC before mechanical disintegration can help to make MFC easier to be processed. Also charged molecules or polymers can be grafted on to MFC to endow charges on MFC surfaces.

1.3 Development of ionic p-n junctions

1.3.1 Development of ionic diodes

Rectification is well known to happen in the silicon-based materials, which use electrons and holes as charge carries [30, 31]. This phenomenon has wide applications in semiconductor devices. However, rectification is also found to happen in ionic conductors, which use ions as their charge carriers. Ionic rectification effect underlies the operation of future man-made devices, whose nature is much more compatible with biological tissues. Labes and Zain were first ones to observe ionic rectification. They observed the difference in current under opposite but equal voltage in a colloid membrane placed between two electrolyte solutions of different salt concentrations[32]. Later on, Reiss pointed out that the excess and deficiency of protons in water corresponding to acidic and basic solutions had a strong similarity to electrons and holes in elemental semiconductors[33]. In these membranes, the fixed charge in “acidic” and

"basic" ion exchangers came close to imitating the donor and acceptor doped semiconductor crystals; consequently, these bilayer membranes also rectified electric current in a manner very similar to the p-n junctions of semiconductor devices. These systems were the ion analogs of the semiconductor junctions. For example, Bockris et al. reported that a double membrane consisting of a cation and an anion exchange membrane showed rectification of alternating current even when an identical salt solution was separated [34, 35]. A typical rectification curve obtained by them is shown in Figure 1.9.

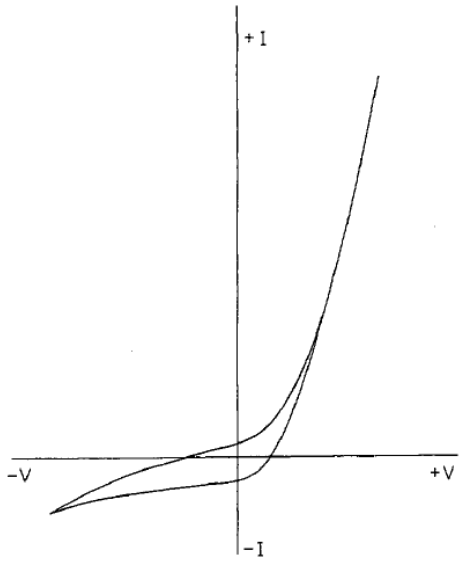

Figure 1.9 An ionic rectification curve obtained by Bockris et al[34].

Later on, Lauger et al. found another alternative electrolytic junction formed by using positively and negatively charged polymer[36]. A junction could be formed on the interface between a solution of a polymeric acid and a solution of a polymeric base, with mobile protons (H^+) and hydroxide ions (OH^-), respectively. Under an applied alternating current, this type of junction showed considerable rectification of ionic current. Cayre et al. further explored ionic rectifier in hydrogel systems[37]. They reported the formation of a fixed rectifying junction by bringing together two aqueous gels containing oppositely charged polyelectrolytes. They claimed that the anisotropic distribution of positive and

negative ions within the device was mainly responsible for the nonlinear current effect across the gel junction.

The similarity of the ionic diodes and the semiconductor p-n junctions is quite obvious and they can also partially borrow theories from each other. But also, they bear some differences. The major differences between these two are the type and number of the carriers. In the semiconductor systems, there are two kinds of charge carries, electrons and holes, whereas, the ionic diodes use ions as their charge carries (usually four kinds, the two counter ions, hydroxide and proton from water). The electrons and holes can recombine with each other when they cross the interfacial area, while the counter ions are injected across the interfacial area, they will exist as "co-ions", which cannot be combined like electrons and holes. The transportation of charges in semiconductors and ionic diodes are also quite different. The diffusion length of ions is much smaller compared to holes and electrons. In addition, the applied potential will have a great influence on the number of charge carriers in ionic diodes, but will have ignorant effect on semiconductors. In ionic diodes, when the potential is high enough, hydrolysis of water will happen and generate a large amount of H^+ and OH^-, these newly generated ions will further affect the electrical behavior of the system. On the other hand, the amount of electrons and holes are irrelevant of the applied potential, except in the extreme case of "breakdown".

1.3.2 Types of ionic diodes

Nonlinear current effect can be found in electrolyte and hydrogels by controlling the ion transportation in the interfacial area. Fabrication of ionic diodes can be realized by numerous ways.

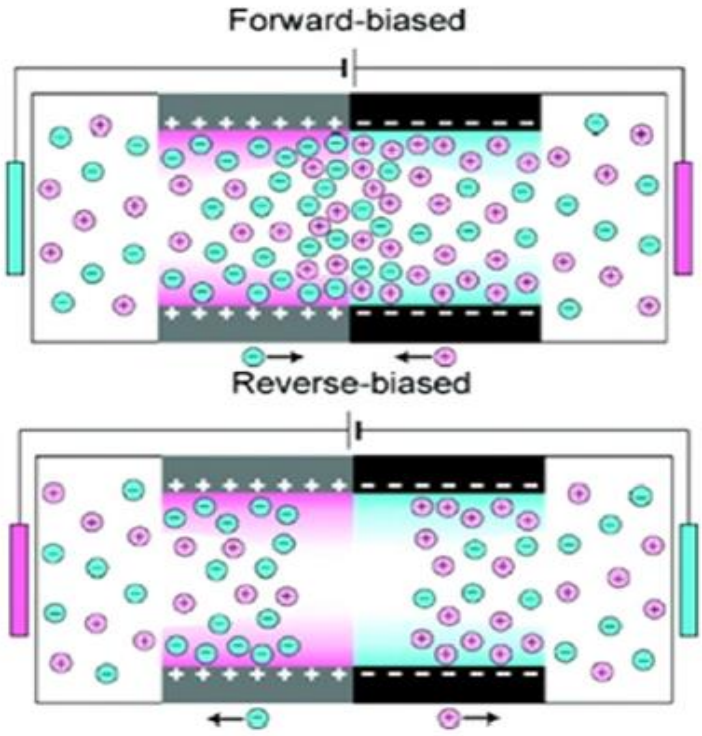

Figure 1.10 Ionic current rectification in a nanochannel with asymmetric charge distribution[38].

Daiguji et al. demonstrated that ionic non-linear current could be controlled by locally modifying the surface charge density of wall in a nanochannel, which is 30nm high and 5μm long as shown in Figure 1.10[38]. When the electrical double layers of the nanochannel were overlapped, it was only possible to control the flow of counterions. If the electrical double layers were not overlapped, both the coions and counterions could be controlled and the channels might have various current characteristics similar to diodes and transistors. Karnik et al. demonstrated rectification of ionic transport in a nano-fluidic diode fabricated by introducing a surface charge discontinuity in a nano-fluidic channel[39]. A one-dimensional model was built to simulate the current voltage characteristics of the devices and yielded agreeable results. Gracheva et al. proposed a design of an electrically tunable rectifying membrane by p-n semiconductor layers[40].

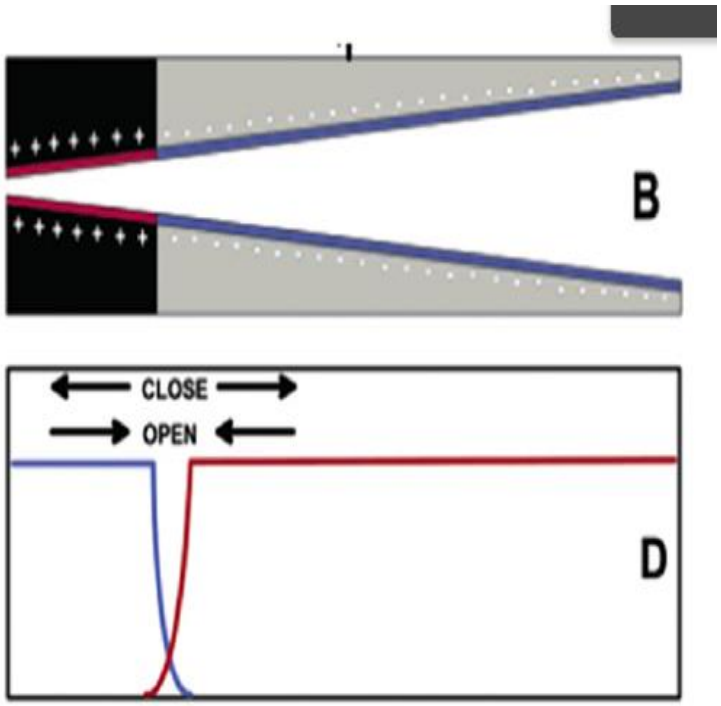

Figure 1.11 A cone-shaped nanotube with asymmetric charge distribution[41].

Asymmetrically shaped nanochannels with charged walls also enabled the ionic current to go in only one way as shown in Figure 1.11[41]. Siwy et al. did both theoretical and experimental study on the current-voltage characteristic behavior in cone-shaped nanochannels[42, 43]. Extensive researches on inversion of ionic rectification on the surface charge density of the cone-shaped channels were conducted by Yan et al[44]. A pH-tunable ionic diode with a cone-shaped channel was also built up[45]. Tapered openings were created on nanopores to get the current-voltage behaviors[46, 47]. These designs could control a small volume of ionic flow with specified nanostructures. The flow could be simply interpreted by kinetic theories in a laminar regime. Difference across nanopores could result in controlled mass transport and selective ion flow. Yusko et al. described a method for generating ion current rectification by employing

electroosmotic flow to fill the narrowest constriction of a pore with either a solution of low or high ionic conductance[48].

Bipolar membrane is another type of ionic diode which appears non-linear current effect under potential and can find wide applications in separating acid and base for industrial use. Bipolar membranes consist of a layer of cation selective membrane joined together by an anion selective membrane. Numerous models and hypothesis have been proposed to calculate the electric properties of bipolar membranes. Bassignana et al. claimed that although there were four ions in the system which could carry the current, on most of the case, the current was carried mainly by two ions, which two depended on the voltage range of the system[49]. Ramirez systematically studied the current-voltage behavior both theoretically and experimentally[50]. The effect of temperature on the membranes was taken into consideration by introducing Arrhenius-type relationship. When the bipolar membranes were reversely biased, they could be used for generation of acid and base. Nagasubramanian et al. stated the optimization of the conditions for generation of acid and base from an engineering and economic perspective[51].

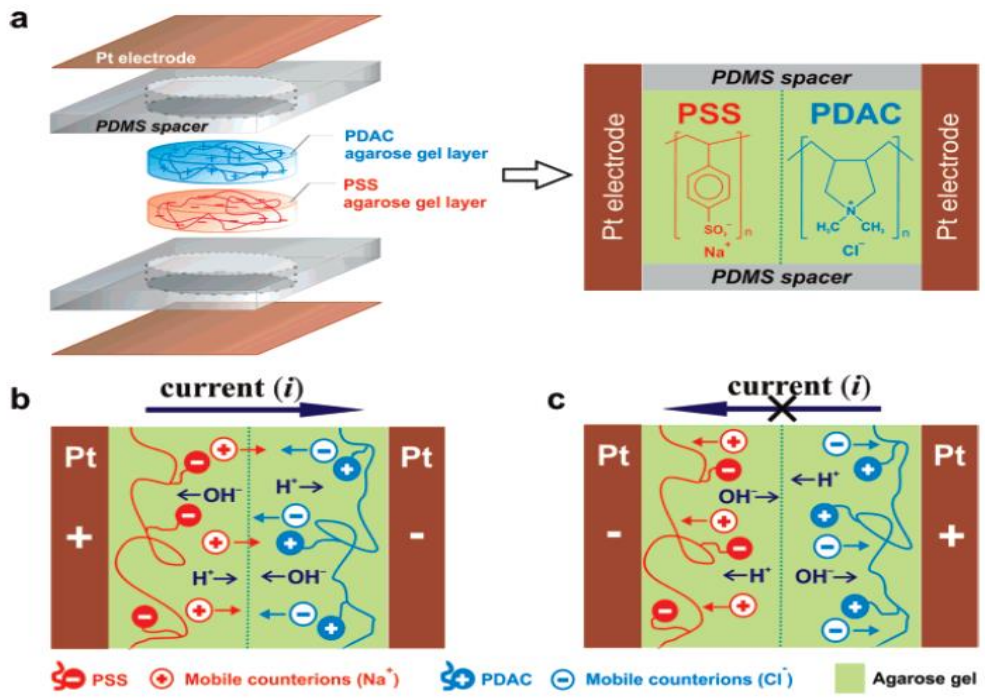

Figure 1.12 Schematic of polyelectrolyte ionic diode devices. Schematic of the ion migration in the diode (b) at forward bias and (c) at backward bias[37].

Polyelectrolyte hydrogel can serve as a stable device to output non-linear current response. Cayre et al. brought together two kinds of polyelectrolyte hydrogel together: one was positively charged polyelectrolyte with negatively charged counterions, the other was negatively charged polyelectrolyte with positively charged counterions as shown in Figure 1.12[37]. When the device was positively biased, the counterions in the system would move towards each other to the opposite electrode, so that current could be conducted. When the device was negatively biased, the counterions could be drawn to the nearest electrode, so that a depletion region was formed at the interfacial area. Conroy et al. performed in-depth researches on a hysteretic current response when a reserve potential was applied on a bipolar hydrogel membrane[52]. They illustrated that the hysteretic effect was due to the incomplete depletion of mobile ions at the junction

between the membranes; the thickness of the depletion region depended on the applied voltage and the surface charge densities. Han et al. demonstrated a microchip-based polyelectrolyte diode and prototypes of integrated ionic circuits[53]. They first monitored the dynamic distribution of ions on a real-time basis using fluorescent ions. More interestingly, logic gates were fabricated by integrating several nanofluidic diodes on a microchip.

The rectification ratio is defined as the ratio of forward current to the reverse current under same voltage value but different direction. It is one of the important index to evaluate the performance of a diode. The rectification ratios of different ionic diodes are summarized in Table 1.1. The rectification ratio is generally lower than that of conventional inorganic diodes. This results from the inefficient control of the backward current under reverse bias. However, these ionic diodes shed a light on exploring new ways of fabrication of diodes and made them more promising to be used in biocompatible fields.

Table 1.1 Comparison of rectification ratios of ionic diodes in the literatures[31]

Description of diodes	Authors and publication year	Rectification ratios
Acid-based electrolyte junctions	Hegedus, 1999	~40(±5V)
Locally charged nanochannels in conical shape	Vlassiouk, 2007	217(±5V)
Oppositely charged Polyelectrolyte hydrogels	Cayre, 2007	~40(±5V)

Conical nanochannels with charged polymer brushes	Yameen, 2009	22(±2V)
Nanochannels with asymmetrically charged inner walls	Cheng, 2009	321(±1V)
Nanochannels with asymmetric shape and polarization	Jung, 2009	~2(±3V)
Polyelectrolyte microchip	Han, 2009	~100(±1V)
Asymmetric charged nanochannels	Yan, 2009	~5(±5V)
SiO_2 nanofilm/agarose gel interface	Koo, 2010	38000(±5V)
Voltage and pH-dependent insulating oxide layers	So, 2012	~14(±5V)

1.4 Introduction of supercapacitors

1.4.1 Structure of supercapacitors

Supercapacitors or ultracapacitors are the terms used for the same type of electric components whose capacitance value can reach thousands of Farads. Supercapacitors and batteries are two main kinds of state-of-art energy storage devices. Figure 1.13 shows a

comparison of Ragone plot of various energy storage devices[54]. Ragone plot is used to show how much energy a device can store and how quickly the energy can be storied or released. Compared to batteries, supercapacitors have significantly lower specific energy density, but higher specific power density, higher cycle life, faster charging-discharging properties[55-58]. Based on the energy storage mechanism, supercapacitors can be classified into two groups, electrochemical double layer capacitors (EDLCs) and pseudocapacitors. EDLCs store charges by electric double layers, for which no chemical reactions will happen[59]. In contrast, pseudocapacitors store charges by fast and reversible redox reactions. In the following section, the structure of both of these types of supercapacitors will be introduced.

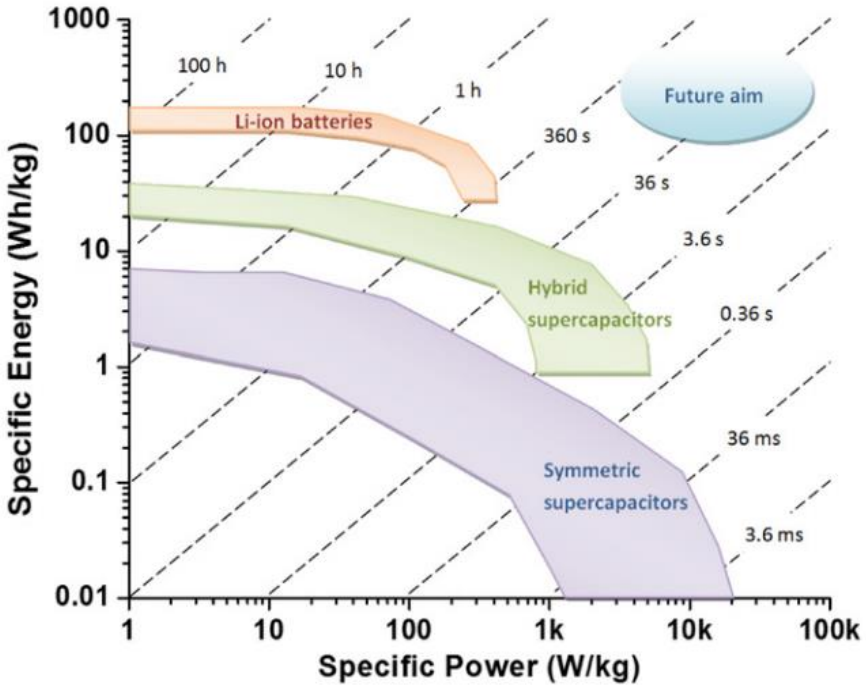

Figure 1.13 Ragone plot of three major electrochemical energy storage devices[54].

Figure 1.14 is an illustration of the structure of a charged supercapacitor[60]. As shown in Figure 1.14 the capacitor has two metallic substrates, called current collectors.

Porous material electrodes (3, 4) are provided and a separator layer (5) is interposed between electrodes to prevent electrical contact. The porous separation layer (5) and the pores (7) from porous electric conductive electrodes are impregnated with liquid electrodes. When bias voltage is applied between the two electrodes, positive charge at the exposed pore surface of one electrode attracts the negative ions (9) from the electrolyte and the negative charge (10) at the exposed pore surface of the other electrode attracts the positive ions (11) from the electrolyte existing in the pores. Thus, an electric double layer is formed at the internal electrode surface and high capacitance value is reached in comparison with other types of conventional capacitors based on dielectric materials, because the distance between the two layers of electric opposite charge is low.

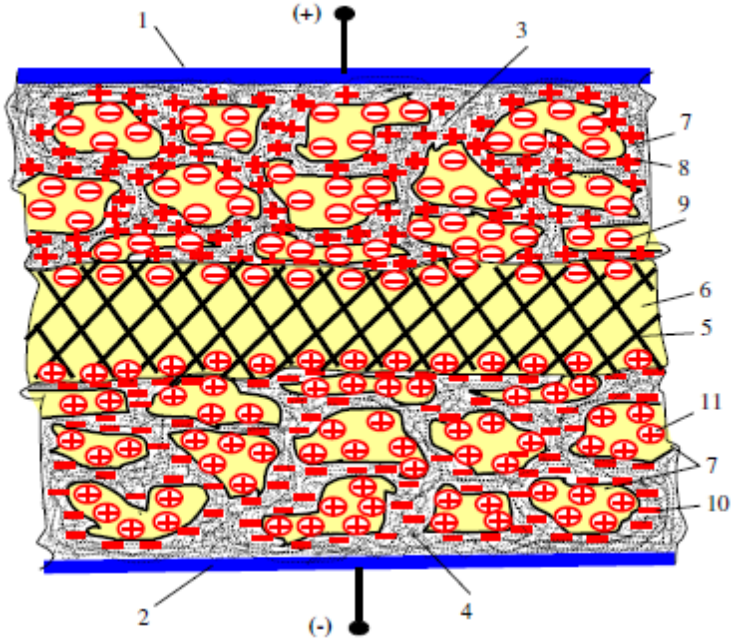

Figure 1.14 Schematics for a charged supercapacitor: 1 and 2—current collectors; 3 and 4—electrodes; 5—separator; 6—electrolyte; 7—pores in the electrode material; 8—positive charge; 9—negative ion; 10—negative charge(electrons); 11—positive ion[60].

The structure of pseudocapacitors is quite similar to EDLCs expect for the electrode materials (4). The electrodes of EDLCs will not chemically react with electrolyte, so that the charges are stored by physical electric double layer absorption. The electrodes of pseudocapacitors, on the other hand, will undergo a faradaic pseudocapacitance of sufficiently reversible redox reactions. There are two main types of faradaic processes in pseudocapacitors. One is redox reactions of metal oxides, for examples, RuO_2 and MnO_2. The other one is reversible electrochemical reactions of doping-dedoping, such as conducting polymers.

1.4.2 Carbon materials based supercapacitors

Carbon materials, metal oxides and conducting polymers are the most frequently used electrode materials for supercapacitors. The principle of carbon materials supercapacitors is based on the EDLCs mechanism; while metal oxides and conducting polymers supercapacitors are working based on the faradiac reactions, used for pseudocapacitors.

Carbon materials have gained much attention as electrode materials for EDLCs, because of their high surface area, electrical conductivity, chemical stability and low cost[61]. The first carbon-based EDLC was discovered in 1957 by Becker[57]. Since its discovery, various carbon materials with different structure have been used to fabricate supercapacitors, such as fibers, powers, tubes, etc. Current technology of activation carbon enables the production of carbons with high surface area, providing extensive electrode/electrolyte interface for charge storage.

Active carbon (AC) materials have mesoporous and nanoporous structures and are excellent electrode materials for EDLCs. The activation of carbon refers to the process to increase surface area and porosity from a carbonized organic precursor. The most used chemical to activate template mesoporous carbon is potassium hydroxide [62, 63]. The activation is performed by heating a mixture of potassium and mesoporous carbon at a

temperature of 400-1000˚C under nitrogen gas. KOH will dehydrate into K_2O at about 400˚C and then reduce to metal K by carbon at a higher temperature. Thus, reduction of K_2O by carbon and the intercalation of metallic K into graphitic layers are considered to be the two key processes to create the surface area for the AC[64]. The mass ratios of KOH/carbon and the activation temperature great influence the properties of activated carbon.

The capacitive behavior of AC depends on several interlinked parameters, which includes specific surface area, the pore size distribution and the conductivity of the electrode, etc. AC has different size of the pores. The pore size of electrodes can be divided into three main categories: (i) micro(<2nm); (ii) meso-(2-50nm); (iii) macro (>50nm)[65]. These three types of pores interact with the electrolyte in different ways, so the electrodes with different size scale of pores behave differently. The studies of influence of pore size on the capacitive behavior of electrodes have been reported by Simon[59, 65].

Nakamura et al. reported EDLCs using polarized AC as electrodes.[66] In their research, coconut shell, phenolic resin and coal were utilized to produce AC by steam treatments, and the EDLCs exhibited specific area of 1860-2012m^2/g with different activation time. They pointed out that the oxygen content and concentration of acidic groups on the surface of AC would affect the electrochemical properties of AC. Endo et al. fabricated EDLCs with AC from different sources and 64F/g at the current density of 1mA was reached for EDLCs with a specific surface area of 700m^2/g. The relationship between the specific capacitance and specific surface area was studied. Yang et al. improved the properties of commercial available AC by CO_2 reactivation[67]. A high specific capacitance of 210F/g was reached for AC EDLCs with a specific surface area of 1050m^2/g after activation, compared with 46.3F/g for untreated AC. Zhou et al. used coconut shell to produce AC and showed a specific capacitance of 79F/g[68].

Carbon nanotubes (CNTs) have been extensively used for supercapacitors because of their excellent conductivity, mesoporous structure and unique physicochemical properties[54, 69-72]. Carbon nanotubes (CNTs) are seamless cylinders of one or more graphene layers, with open or closed ends. They can generally be categorized as single-wall, SWCNT, or multiwall MWCNT. Diameters of SWCNTs and MWCNTs are typically 0.8 to 2 nm and 5 to 20 nm, respectively. Although CNT diameters vary from different production methods and the diameter of MWCNT can exceed 100 nm. The lengths of CNTs range from less than 100 nm to several centimeters. CNTs usually entangle up to form a mesoporous network with a surface area of 100-400m^2/g. There are usually three technical routes to synthesize CNTs, which are arc-discharge, laser-ablation and chemical vapor deposition (CVD). The former two processes need high temperature up to 2000-3500˚C for the metal and carbon to evaporate, while CVD needs only 500-1200˚C. The sources of carbon can be CO, hydrocarbon, alcohol, and so on.

The supercapacitors fabricated from pure MWCNTs typically show specific capacitance ranged from 4-135F/g[73, 74], while the ones fabricated from pure SWCNTs typically show maximum capacitance of 180F/g[75]. Lee et al. fabricated MWCNT supercapacitors exhibited an initial specific capacitance of 128F/g while stabilized after 50 cycles at 58F/g [76]. Yoon et al. directly synthesized CNTs on Ni substrate by CVD. Cyclic voltammetry showed that the devices could work at high scan rate up to 1000mV/s[77]. The specific capacitance was measured to be 38.7F/g, but could be improved by ammonia plasma treatment to 207.3F/g. Ye et al. claimed that oxidation of CNT could significantly improve the surface area of CNT by cutting off the tips, thus improved the specific capacitance of the CNT-based supercapacitors. The devices fabricated by oxidized MWCNT showed capacitance of 335.2F/g, which was 11 times higher than devices fabricated by unmodified MWCNT of 32.7F/g[78]. Similar electrochemical oxidation researches were done by Liu et al. on SWCNT[79]. The results

showed that the electrochemical process could successfully control the pore size distribution of SWCNTs, i.e. much higher specific surface area could be achieved by electrochemical treatment. The EDLCs fabricated by the treated SWCNTs showed three-fold higher in terms of specific capacitance than those made of untreated ones. CNTs could also form composites with metal oxides or conducting polymers to serve as excellent electrode materials for supercapacitors.

Graphene-base materials are newly rising intriguing electrode materials for supercapacitors because of their superior electricity conductivity, high surface area and unique chemical and physical properties[80, 81]. Graphene consists of a 2D layer of sp^2 bonded carbon atoms, and it is considered as the basic construction material for carbon materials[82, 83]. There are several effective ways to synthesize graphene-based materials, including (i) epitaxial growth and CVD growth of graphene on SiC and matched metal surfaces; (ii) exfoliation of graphite by micromechanical methods, such as atomic force microscopy (AFM) or adhesive tapes; (iii) exfoliation of graphite in organic solvents;(iv) substrate-free gas phase synthesis of graphene platelets in a microwave plasma reactor; (v) arc-discharge synthesis of multi-layered graphene; (vi) reduction from graphene oxide(GO). The methods of preparation of graphene-materials vary, but the most practical and common way to fabricate graphene-based materials is the chemical exfoliation of graphite to GO, followed by controllable reduction of graphene oxide to graphene[84-86]. This method is widely adopted and used because (i) GO can be easily produced in a large scale and its functional groups make it easy to be handled in solution, (ii) numerous ways can be used to reduce GO to graphene with controllable morphology.

Ruoff et al. first explored using chemically modified graphene as electrode materials to fabricate EDLCs. Although they found that graphene tended to agglomerate into particles around 15-25μm during the reduction process, the supercapacitors still showed excellent electrochemical properties due to the relatively high specific surface area ($705 m^2/g$) of graphene. The devices in aqueous and organic electrolytes showed

specific capacitance of 135 and 99F/g respectively. In addition, the smaller variation in capacitance with the change of scan rates was observed because of the high conductivity of the graphene (~200S/m). Their original work showed great potential of graphene to be used in energy storage areas and led more studies to improve the capacitance for graphene-based supercapacitors. To solve the problem of aggregation of graphene, Chen et al. explored a gas-solid reduction method to prepare graphene[87]. The as fabricated supercapacitors showed an energy density of 28.5Wh/kg in aqueous solution and 90% of specific capacitance remained after 1200 cycle tests. Ma and co-workers reported using hydrobromic acid as reducing agent for GO exfoliation[88]. Because hydrobromic acid is a weaker reduction agent, the yielded oxygen functional groups are relatively stable. Thus the oxygen containing groups not only promoted the wettability of the graphene, but also improved the penetration of the aqueous electrolyte into the pores of graphene. A maximum specific capacitance of 348F/g in aqueous solution was achieved at the current density of 0.2A/g. Surprisingly, the specific capacitance did not decay but improved after cycle tests. This may be because that oxygen containing groups were further reduced during the cycling tests and improved the capacitive properties of the devices. Graphene could also be prepared by thermal exfoliation of GO. Rao et al. prepared graphene through thermal exfoliation of GO at 1050˚C. The SSA was reported as large as 925m^2/g and specific capacitance was reported to be 117F/g. However, the high temperature exfoliation was energy consuming. In order to solve this problem, Yang et al. performed the exfoliation at 200˚C under high vacuum[89]. The results showed that the graphene exfoliated at low temperature tended to aggregate and form larger pores, so that the electrolyte could easily penetrate the surface of graphene. The specific capacitance was tested to reach 264 and 122F/g for aqueous and organic electrolyte.

1.4.3 Metal oxide based supercapacitors

Metal oxides are promising electrode materials for supercapacitors because of their high capacitance, ease of large-scale fabrication. The capacitance of metal oxides based supercapacitors is usually 2-3 times higher than those of carbon-based supercapacitors, because of the rich redox reactions [90, 91]. Most of the metal oxides, such as irons and manganese oxides are abundant, thus low cost. The easy control of the morphology of metal oxides makes them good candidate to study the structure-properties relationship. Researchers have designed various morphology of metal oxides to optimize their electrochemical properties as shown in Figure 1.15[92]. From the view of surface electrochemistry, the tailored designs of electrode, such as 1-D array, or core shell structure, can effectively decrease the surface energy of the nanomaterials, obtain better electron-transfer rates, etc. [93-95]. The common metal oxides used in supercapacitors include ruthenium oxide, iridium oxide, manganese oxide, cobalt oxide, nickel oxide, tin oxide, iron oxide, pervoskites, fermrites, etc. In the following section, manganese oxide and ruthenium will be discussed in more details as examples for metal oxides.

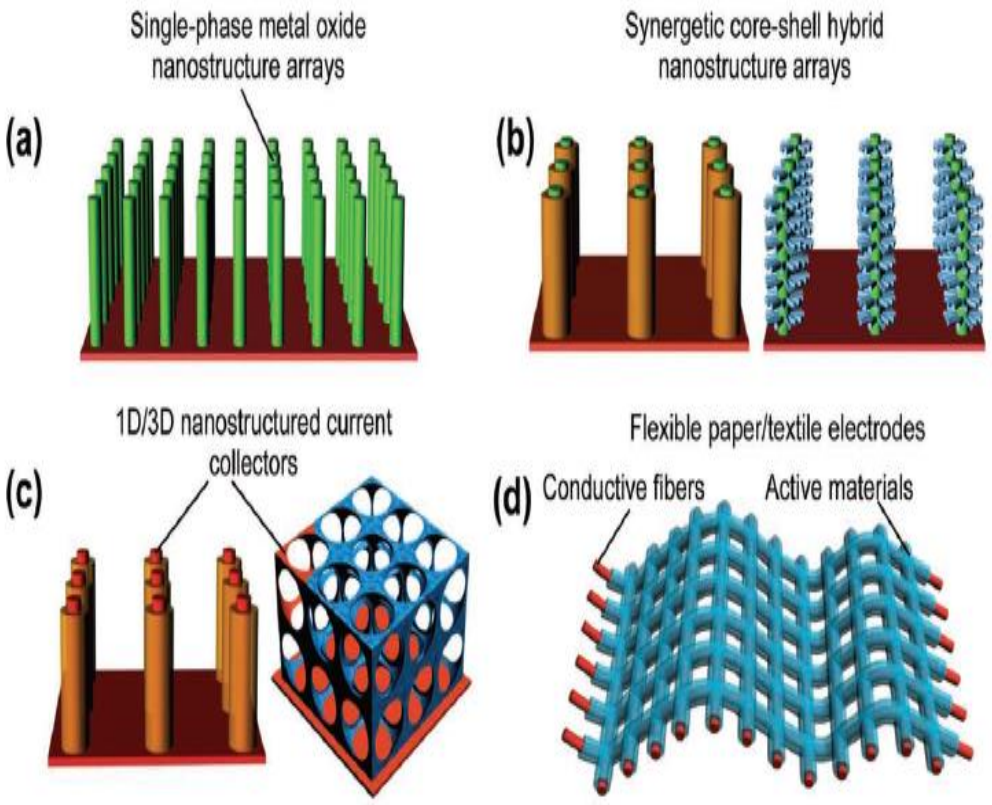

Figure 1.15 Schematics of various shapes of metal oxides and their hybrids[92].

Manganese oxides are low cost and non-toxic electrode materials. Manganese has several oxidation states, Mn(0), Mn(II), Mn(III), Mn(IV), Mn(V), Mn(VI), Mn(VII). The conversion between different oxidation states can effectively store charges in supercapacitors. Figure 1.16 showed a typical cyclic voltammetry (CV) of chemically deposited MnO_2 electrode at different scan rates in 1M Na_2SO_4 electrode[96]. There were two factors which were found to affect the cycle life of MnO_2 significantly. The first one was the dissolution of MnO_2. The other one was the oxygen evolution reaction of MnO_2. Most of the MnO_2 supercapacitors showed a decrease of 20 percent in specific capacitance after 1000 charge and discharge cycles. In addition, water content for MnO_2 thin film was known to affect the electrochemical reactivity and thermodynamic stability

of MnO_2, because it caused a variation in crystal lattice and a consequent variation in electrical conductivity and electrode potential [97].

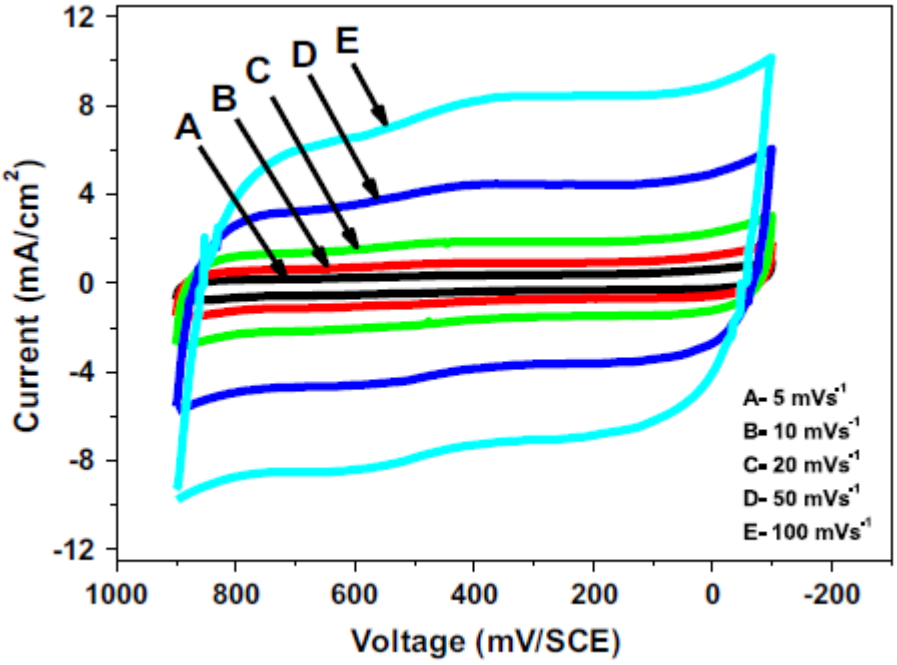

Figure 1.16 A typical cyclic voltammetry (CV) of MnO_2 electrode at different scan rates; (A) 5, (B) 10, (C) 20, (D) 50 and (E) 100mV/s in 1.0 M Na_2SO_4 electrolyte[96].

Ruthium oxides have been intensively studied for supercapacitors because of their high theoretical specific capacitance (1358F/g) and high electrical conductivity (300S/cm). RuO_2 can be in either crystalline or amorphous form. The high capacitance was known to result from under-potential hydrogenation and oxygenation in acidic and alkaline electrolyte[98]. Specific capacitance of up to 750F/g for electrodeposited RuO_2 and 800-1200F/g for hydrous RuO_2/carbon composites had been reported[99]. The high capacitance was due to pseudocapacitance from the reactions between Ru ions and H ions. The typical CV plot of RuO_2 is shown in Figure 1. 17. Zheng claimed that there are several processes which determine the capacitive performance of $RuO_x \cdot nH_2O$: (i) electron hopping within $RuO_x \cdot nH_2O$ particles; (ii) electron hopping between particles; (iii)

electron hopping between electrode materials and current collectors; and (iv) the proton diffusion within $RuO_x \cdot nH_2O$ particles[100]. The advantages of using RuO_2 supercapacitors include their high specific capacitance, high electrical conductivity and good electrochemical reversibility. However, the high cost and toxic nature of ruthenium oxides prevent them from large-scale production and wide application.

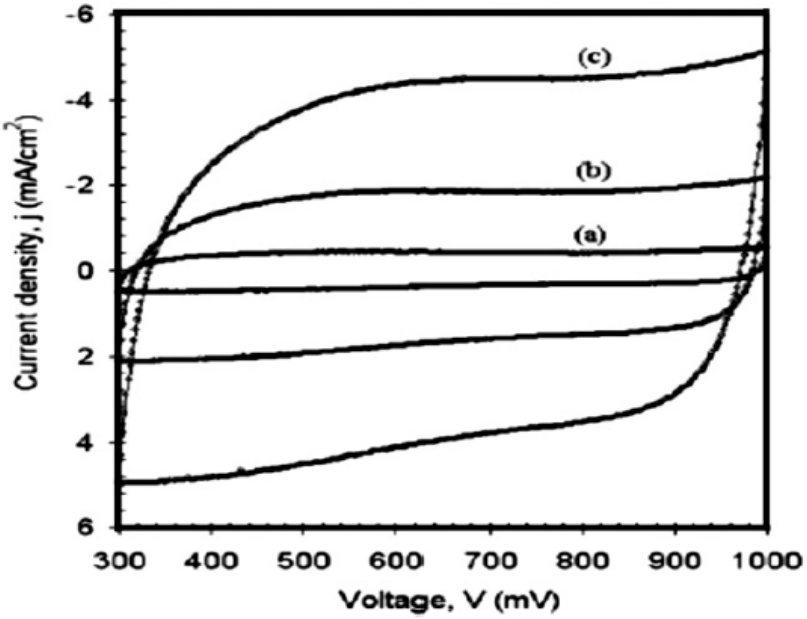

Figure 1.17 The typical CV plot of sprayed ruthenium oxide electrode at different scan rate: (a) 5, (b) 25, (c) 50mV/s in 0.5M H_2SO_4 electrolyte[100].

1.4.4 Conducting polymer based supercapacitors

Conducting polymers are pseudo-capacitive materials, which store charges by fast redox reactions. Conducting polymers show high specific capacitance, high electrical conductivity, high power density, however they also exhibit low cycling performances. The electrical conductivity of conducting polymer is realized by a conjugated bond system along the polymer backbone. The most commonly studied polymers are polyaniline, polypyrrole, etc. They can be normally synthesized by chemical oxidation of

monomers or electrochemical oxidation of monomers. During the synthesis process, the oxidation of monomers and the oxidation of polymers occur simultaneously, leaving the dopant/counter ions inserted in the polymers. The doping level is typically below 1 dopant per unit: usually 0.3-0.5.

Conducting polymers have good intrinsic conductivity, ranging from a few S/cm to 500S/cm in doped states [101, 102]. They have low band gaps (1-3eV) compared with other polymeric materials (10eV)[101]. Conducting polymers can be p-doped with anions when oxidized, and n-doped with cations when reduced. The illustrations of these processes are indicated as below:

$Cp \rightarrow Cp^{n+}(A^-)_n + ne^-$ (p-doping); $Cp + ne^- \rightarrow (C^+)_n Cp^{n-}$ (n-doping);

The discharge reactions are reserves of the above equations. However, many conducting polymers, such as polyaniline and polypyrrole, can only be p-doped. This is because that they cannot reach the negative potentials required for n-doping. An example of n-doped material is polythiophene and its derivatives.

The conducting polymers can be doped and undoped quickly, which render them high power capabilities. However, they also have the drawback of low energy density. This is because that the diffusion rate of ions into the bulk electrodes materials is low. Nevertheless, conducting polymers can still bridge the gap between batteries and EDLCs. In the other hand, because of the doping and dedoping processes of conducting polymers during charge and discharge, the materials swell and contract in the meantime, which gives them poor cycling performances. They often tend to degrade within 1000 cycles. But interestingly, the researchers found that when working with ionic liquid as electrolyte, the conducting polymers showed better life time[103, 104].

Polyaniline has been studied extensively as an electrode material for supercapaictors. Polyaniline belongs to the family of semi-flexible rod polymers. The structure of polyaniline is indicated as in Figure 2. 16. It has many desirable properties,

such as high electrical conductivity, high hoping level, excellent stability and a high specific capacitance [105, 106]. A major drawback of polyaniline is that it need a proton to be charged and discharged, thus a protonic solvent is required.

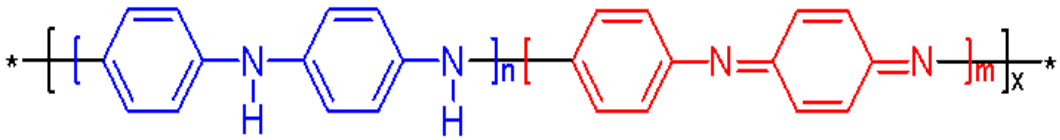

Figure 1.18 Structure of polyanline. n+m=1; x=degree of polymerization. [www.en.wikipedia.org/wiki/polyanline]

Polyaniline (PANI) have three oxidation states: leucoemeraldine, which appears white/clear colored; emeraldine, which appears green or blue colored; pernigraniline, which appears blue or violet colored. The chemical synthetic method to produce polyaniline is quite simple, which can be illustrated in Figure 1.19. The monomers will first draw anions from the solution to form aniline anions, and then grow into nucleates on the substrate. Polyaniline will further grow on the nucleates and then form the final long chain structure.

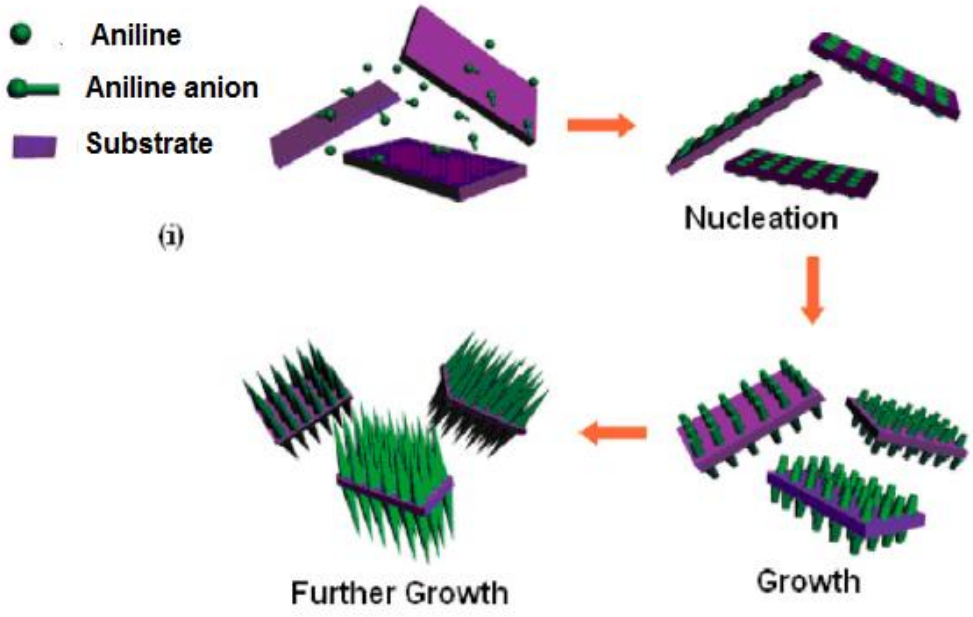

Figure 1.19 The growth mechanism of PANI on a substrate[107].

A wide capacity range has been reported for polyaniline, from 44-270mAh/g[105]. The variation in capacity can be related to many factors, such as different synthetic routes, polymer morphology, the amount and type of binders and additives, the thickness of the polymers, etc. For example, the polyaniline synthesized by electrodeposition usually had higher specific capacitance than that synthesized by chemical route. The electrical conductivity of polyaniline also varied from 0.1-5S/cm[107]. The CV and charge-discharge plots of PANI based supercapacitors under different scan rates are shown in Figure 1.20.

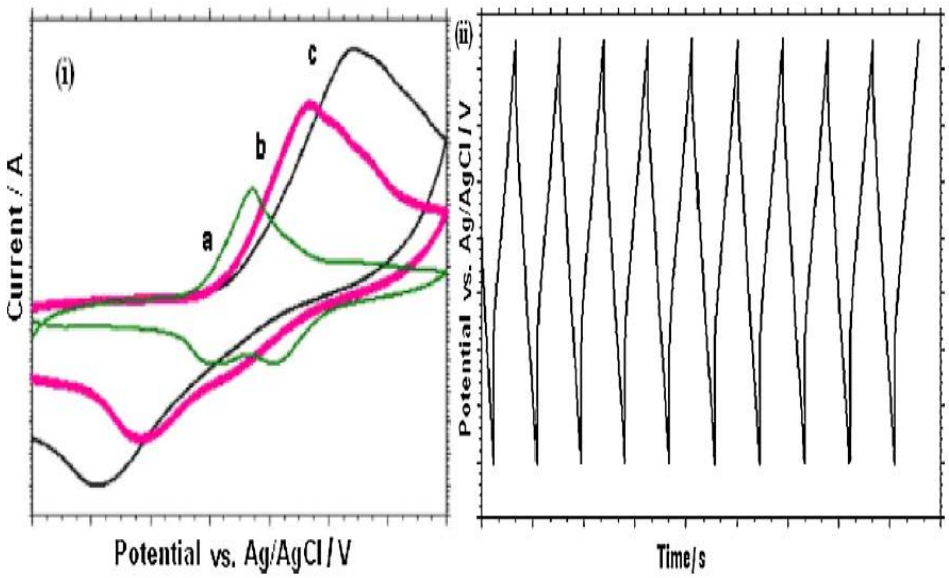

Figure 1.20 (i) Schematic depiction of CV for PANI based SCP at different scan rate c>b>a (a) 100mV/s, (b) 300mV/s and (c) 500mV/s and (ii) charge discharge response[108].

Chaudhari et al. fabricated PANI nanofibers web as electrode materials for supercapacitors[109]. The scanning electron microscope showed the web was made up of fibers with high aspect ratio (>50). The diameters were about 200nm. The electrochemical properties of thus made PANI web were compared with those of PANI powders. The specific capacitance of PANI web was 267F/g, which was superior that PANI powders of 208F/g. The cycle tests showed the PANI web could retain 86% of its specific capacitance (to 230F/g), which was much better than PANI powders of 48% capacitance retention. Shaikh et al. synthesized template free PANI nanobuds by anodic electrochemical polymerization method[110]. The nanobuds were perpendicular to the substrate and were broader at their bottoms and narrower at the tops. A specific capacitance of 128F/g was measured for the PANI nanobuds at 10mVs scan rate in aqueous electrolyte.

Polypyrrole (Ppy) is another kind of important conducting polymer for energy storage. Its flexibility is much better than most of other conducting polymers[108]. Its disadvantage is that it cannot be n-doped, thus it can only serve as a cathode material. Ppy has greater density, so that it has a high capacitance per unit volume (400-500Fcm^{-3})[108]. However, this also leads to limited access to the interior surface of the polymer for the counter ions. That is also the reason why ppy has low capacitance in terms of per gram. Ppy is typically doped with single charged anions such as Cl^-, ClO_4^- and SO_3^-, but when doped with multiple-charged anions, like SO_4^{2-}, ppy can physically crosslink together[111]. Suematsu et al. claimed that once ppy crosslinked, it would have higher diffusivity and higher capacitance, due to the porosity formed during the process of crosslinking[111]. However, he did not support this point by reporting the capacitance per gram, but reported capacitance per volume. This value (100-200Fcm^{-3}) was lower than typical capacitance of ppy reported (400-500cm^{-3}).

Sun et al. reported ppy films doped with ClO_4^- on Ni modified 3D Si substrate[112]. The supercapacitors fabricated showed ideally rectangle-like CV curves when scanned from 5-200mv/S. The specific capacitance was calculated to be 0.03F/cm^2 at scan rate of 100mV/s from CV. Lee et al. fabricated ppy nanorods using aluminum oxides as templates[113]. The ppy was electrochemically synthesized and gold was thermo-evaporated as current collectors. After removing aluminum oxide template in alkali solution, a well-arranged ppy nanorods with large SAA was produced. Higher specific capacitance was observed with longer nanorods due to larger surface area. Oliveira et al. synthesized ppy in the presence of functionalized graphene sheets by an interfacial method[114]. The synergistic interaction between the p-typed ppy and the carboxylate functionalized graphene sheets resulted in a higher capacity than either of the material used alone. The high conductivity of p-doped ppy and the high surface area of graphene could improve the capacitance of the composite supercapacitors. A high capacitance of 277.8F/g was reported.

1.4.5 Flexible supercapacitors

Flexible electronics, like flexible supercapcitors have been recently caught great attention because of their applications in wearable, portable, miniaturized areas. Flexible electrodes are one of the keys for fabrication of supercapacitors. Nowadays, the primary materials used for flexible electrodes are carbon materials. Carbon materials can be of various shapes in microscopic and macroscopic perspective, as shown in Figure 1.21(a). Zero-dimensional carbon materials include fullerene and carbon particles, one-dimensional include carbon nanotubes and carbon fibers, two-dimensional include graphene and graphite sheets. Out of these materials, 1D and 2D carbon materials have been extensively used for flexible electrodes because they can readily form carbon networks, such as carbon fabric, carbon film, carbon paper and carbon textile, as shown in Figure 1.21(b).

Carbon network can roughly be divided into two categories: single carbon electrodes and carbon composite electrodes. Single carbon electrodes are only made of various shapes of carbon; whereas composite electrodes are made of composites of carbon with other pseudocapacitive materials.

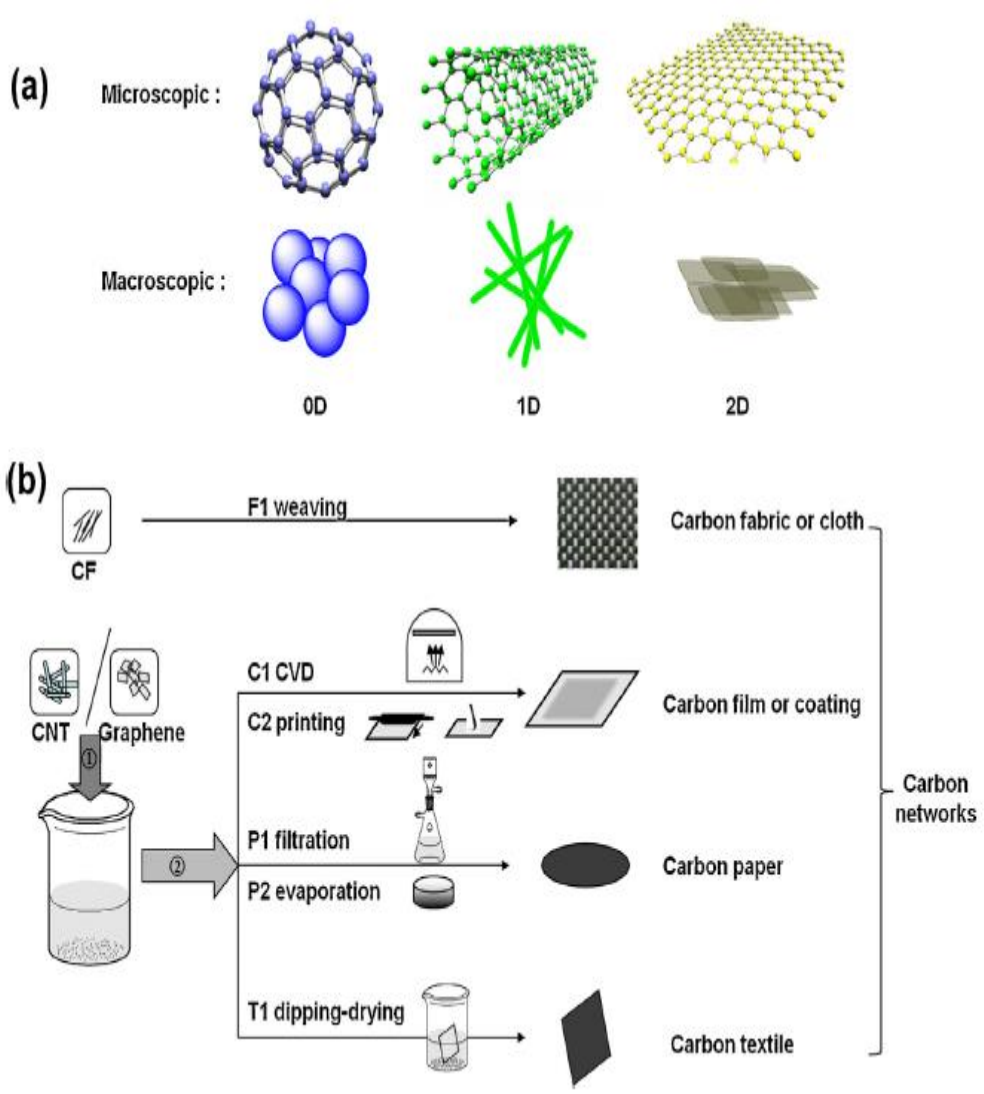

Figure 1.21 (a) Schematic illustration of 0D, 1D, and 2D carbon materials at the microscopic and macroscopic scale. (b) Fabrication of carbon networks with carbon fibers (CF), carbon nanotubes(CNT), and graphene as starting materials[110].

Single carbon electrodes include carbon fabric, cloth, film, coating, paper or textiles. They are usually formed by aggregation of 1D or 2D carbon materials through hydrogen bonds or van der Waals forces. The most common flexible electrode is carbon fabric, which can be formed by weaving carbon fibers in a commercial way. In addition, fibers can be mixed with other pseudocapacitive materials to obtain hybrid fabric. For

example, Reddy et al. fabricated asymmetric carbon fabric-based supercapacitors[115]. One side of the electrodes were made up polymer/MWCNT carbon fabric, the other side of the electrodes are made of metal oxide/MWCNT carbon fabric. Nafion membranes were sandwiched with the two kinds of fabric electrodes to make flexible supercapacitors. Carbon films were usually fabricated by a CVD method and a printing process. Yu et al. prepared buckled SWCNTs on an elastomeric polydimethysiloxane (PDMS) substrate followed by the relaxation of the prestrained substrate[116]. The electrochemical properties of the supercapacitors fabricated by these electrodes were not affected by bending of the devices. Printing process to make carbon films could be realized by using Meyer rods, brushes, ink-jet printer or spin-coating tools. The substrates for printing were usually flexible plastics or paper. He et al. reported the conductance as low as 10Ω/sq on printed paper using a scalable Meyer rod coating[117]. However, sometimes the pores on the paper were too large, which would lead to short-circuited after the printing. Kaempgen et al. pretreated the surface of the paper with polyvinylidene fluoride (PVDF) to solve this problem[118]. Carbon paper could be made by filtration or evaporation method. Special paper was made by carbon materials through hydrogen bonds or van der Waals forces. Carbon paper could be directly used as an electrodes or be treated before application. For example, graphene was added into cellulose pulp to make graphene/cellulose paper sheet. In addition, Kang et al. fabricated supercapacitors by assembling two pieces of graphene/cellulose papers in an organic electrolyte, showing a high specific capacitance about 252F/g at a current density of 1A/g[119]. Najafabadi et al. made self-standing carbon paper by evaporating solvent in a Petri dish[120]. Carbon textiles can be fabricated by dipping-drying technology. A piece of fabric was dipped into a pre-made solution, and then dried until all the solution was removed. Pasta et al. used this method to make a SWCNT textile with a low sheet resistance of 1Ω/sq and showed specific capacitance of 70-80F/g at current density of 0.1A/g[121]. Wu et al. fabricated flexible carbon textile through a solvent free method by drawing a graphite rod onto

cellulose paper. The supercapacitors exhibited a specific capacitance of 23F/g at a current density of 0.2A/g[122]. Carbon textiles could be used as electrodes with great flexibility and high specific capacitance.

Since the specific capacitance of single carbon electrode was small, carbon composite electrodes were studied to incorporate high-capacitance pseudocapacitive materials into carbon. Much effort has been devoted to coat metal oxides or conducting polymers onto carbon networks by solution based methods as shown in Figure 1.22[123]. The pseudocapacitive materials can be coated onto carbon networks by electrodeposition, in situ growth methods, electropolymerization or chemical polymerization. For example, graphene/Ppy composite films were made by simple electrodeposition of graphene oxides and pyrrole under acid condition[124]. The composite films were directly used as electrodes because of the fast redox properties of ppy and high conductivity of graphene. A high specific capacitance of 335F/g was obtained with 85% retention at the current density of 1A/g. Yuan et al. designed a carbon nanoparticles/MnO_2 hybrid structure using an electrodeposition method. They further built up solid, flexible supercapacitors with the hybrid composites[125]. Giri et al. combined transition metal into MWCNTs first and then in situ oxidation polymerized polyaniline onto MWCNTs[126]. The specific capacitance of the composite supercapacitors was reported to be 920F/g at scan rate of 2mV/s. Wu et al. produced carbon-based composite paper the way same as production of carbon paper[122]. Graphene/PANI paper was made by filtration of a solution of graphene and PANI. A specific capacitance of 210F/g and 198F/g was reported for a current density of 0.3A/g and 3A/g respectively.

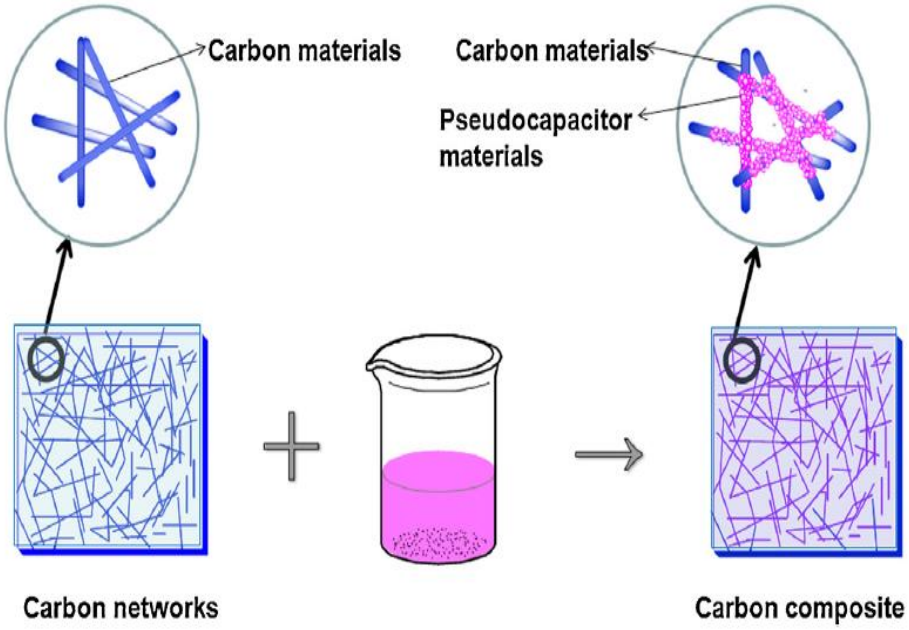

Figure 1.22 Fabrication of carbon composites by coating pseudocapacitive materials onto carbon networks through a solution-based method[123].

In the section of 1.4.1, we have introduced the structure of conventional supercapacitors, which consist of current collectors, positive and negative electrodes, electrolyte, and separators. However, the structure of flexible supercapacitors does not need current collectors or binders as shown in Figure 1. 23[123]. The reason is that the carbon networks have both high conductivity and flexibility, which make them serve as both current collectors and active electrodes. Soft and bendable plastic films are widely used for flexible supercapacitors as the packages. The simplified architecture is light and compact compared with the conventional supercapacitors.

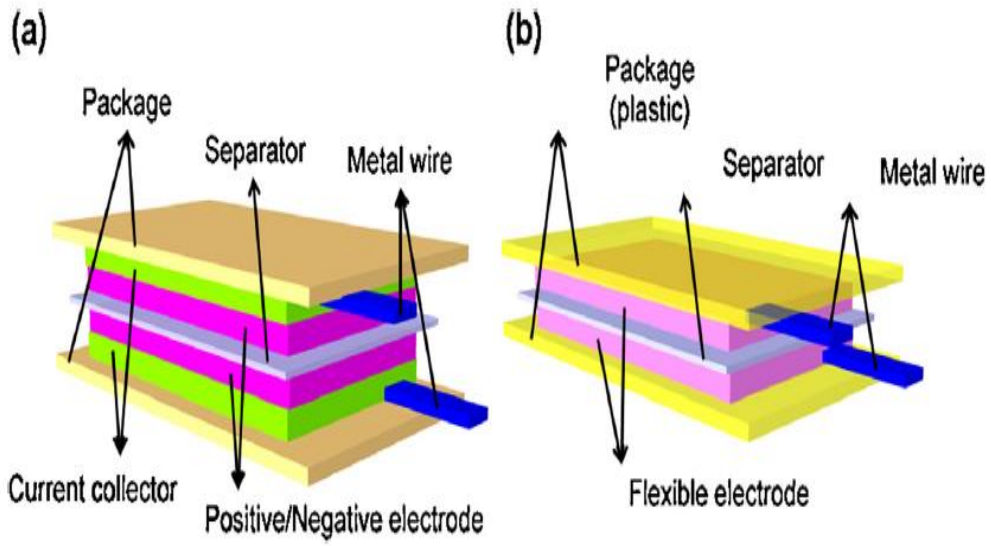

Figure 1.23 Schematic illustration of (a) a traditional supercapacitor and (b) a flexible supercapacitor[123].

In addition to the electrodes, electrolyte in flexible supercapacitors is also an important component. The electrolyte in flexible supercapacitors can be categorized into two types: liquid electrolyte (including aqueous liquid electrolyte and organic electrolyte) and solid electrolyte. Common liquid electrolyte can be aqueous and organic solvent. Aqueous electrolyte can be acid electrolyte (for example, HCl or H_2SO_4 aqueous solution), mild electrolyte (for example, KCl, LiCl, Li_2SO_4 aqueous solution), or alkaline electrolytes (for example, NaOH, LiOH, or KOH aqueous solution). Organic electrolyte is usually made of salt dissolved in organic solvent. For example, LiPF6 in ethylene carbonate/diethylene carbonate. Solid state electrolyte is usually made of a gel, a solute and a solvent. The gel agents can be PVA, PVDF, or poly(vinylidene fluoride-co-hexafluoropropylene). The solute can be salt or acid. The solvent can be water, etc. For example, H_3PO_4 is added to PVA/water to form solid state electrolyte. The electrolyte and separator used in flexible supercapacitors are listed in Table 1.2.

Table 1.2 Electrolyte and separators used in flexible supercapaictors.

	Electrolyte	Separators
Liquid electrolyte	Aqueous solution; acid electrolyte (H_2SO_4,H_3PO_4 solution),mild electrolyte (KCl, LiCl, etc), alkaline electrolyte(KOH, LiOH solution, etc)	Cellulose/glassy paper, PTFE membrane, polyacrylonitrile membrane.
Solid-state electrolyte	Acid solution/PVA(like H_3PO_4/PVA), Nafion membrane, $EMIBF_4$/P(VDF-HFP)	Paper

1.5 Introduction of dye-sensitized solar cells (DSSCs)

1.5.1 Fundamental concepts and principles of DSSCs

Photovoltaic cells, also called solar cells, transform solar energy directly into electricity. Because people's increasing awareness of exploring clean energy, great focus has been put onto the development of solar cells. Since the concept was first pulled up in 1839, solar cells have mainly went through three generations of development. The first generation of solar cells were based on p-n junction silicon materials, although this kind of solar cells were quite expensive and hard to realize commercialization, they set up the fundamental principles of solar cells (i.e. the process in which photo-induced electrons jump from the valence band to conduction band and are then transferred though out the circuit). The first generation of solar cells consisted of (i) n-type layer (i.e.,

semiconductors doped with atoms which have more valence electrons than the matrix) working as the electron donating anode; (ii) p-type layer (i.e., semiconductors doped with atoms which have less valence electrons then the matrix) working as the electron accepting cathode; and (iii) the p-n junction, which is the interface of the two layers. Light absorption happened in the p-n junction, and the electrons and holes were separated with the electron excitation and were transported in the opposite direction to form the electricity. For the purpose of lowering the cost of fabrications of solar cells while maintaining their performance, second generation of solar cells appeared. The second generation of solar cells were based on thin film technology. These cells were also built upon p-n junctions to separate the photo-induced charge carriers. Examples of this kind included amorphous and crystalline Si on glass, polycrystalline CdTe, etc. Nowadays, researches have begun to work on the third generation of solar cells. The third generation of solar cells are aimed to further lower down the fabrication cost while improving or maintaining the conversion efficiency. Examples of the third generation solar cells are dye-sensitized solar cells and organic solar cells. Interestingly, these cells do not follow the same principle of the first two generations of solar cells. In this thesis, dye-sensitized solar cells will be extensively studied and their working principles will be introduced in the following section.

DSSCs represent new generations of photovoltaic devices[127], as low cost alternatives to the conventional p-n junction photovoltaic devices. In 1991, Michael Gratzel and Brian O'Regan first pulled up the concept of DSSCs[128]. Instead of strict requirements for fabrication of silicon solar cells, Gratzel and O'Regan designed this new solar cells based on the low-cost titanium dioxide nanoparticles with a dye, which could expand the solar absorption region to visible light. A schematic illustration of DSSC is shown in Figure 1.24[129]. On a conducting class, a mesoporous oxide layer of nanometer-sized particles were sintered together to allow electronic conduction. The oxide materials need to have wide band gaps, such as TiO2, ZnO, Nb2O5, etc. A thin

layer of charge transfer dye was absorbed on the surface of the nanocrystalline oxide film.

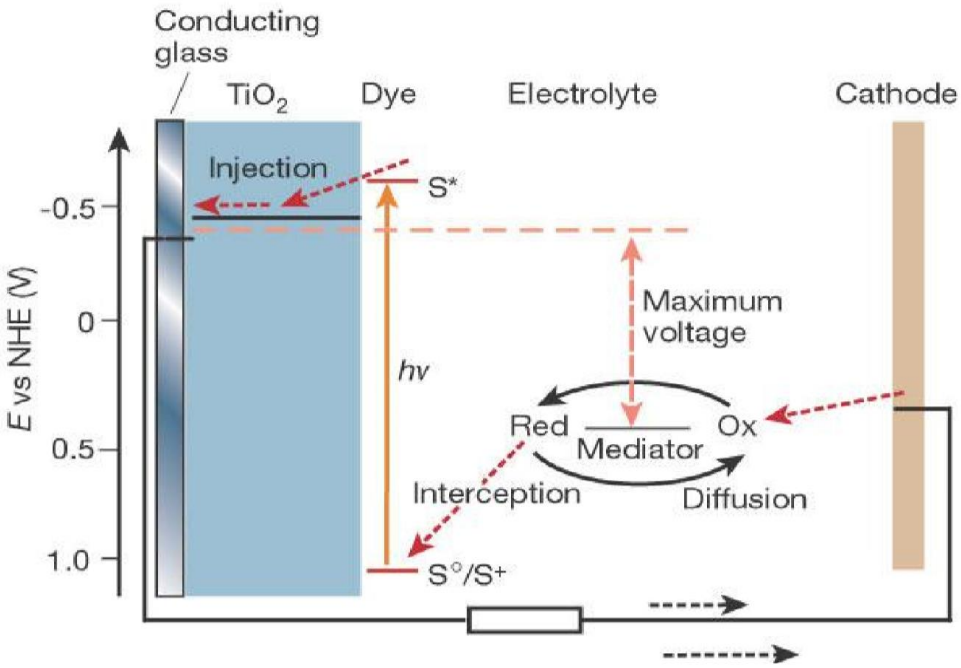

Figure 1.24 Principles of operation and energy level scheme of the dye-sensitized nanocrystalline solar cells[129].

Upon incident light, the electrons of the sensitizer (dye) jumped from the ground state to the excited state. Since the excited state was not stable, the electrons of the sensitizer were injected to the conduction band of the mesoporous oxide semiconductors and then to the charge collectors, which were conductive glasses in this case. The electrons collected by conductive glasses passed through the external circuit to the counter electrode and were then captured by the redox electrolyte. The redox electrolyte received the electrons and helped to regenerate the sensitizers back to their original state, completing the whole charge transfer circle. The open-circuit was determined by the difference between the redox potential of the electrolyte and the Fermi level of the

nanocrystalline film. Overall the devices transformed the solar energy into electrical energy without any permanent chemical alternation.

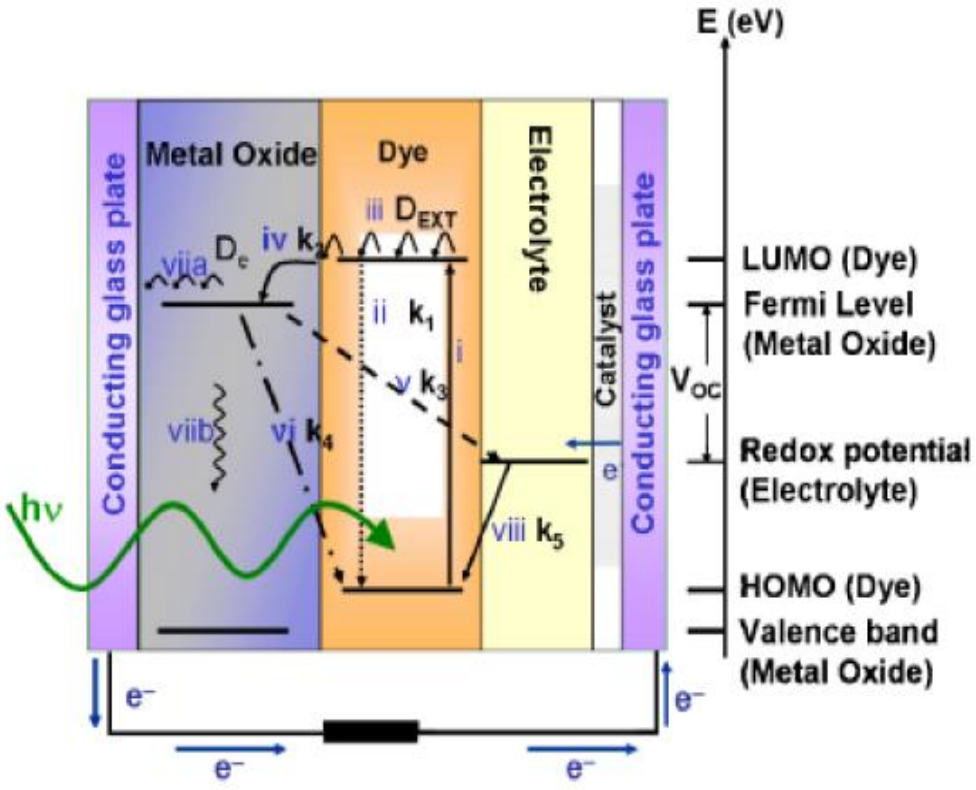

Figure 1.25 Functional diagram of DSSCs. The dashed arrow show the possible losses in DSSCs. The vertical line on the right shows the energy scale in eV. The energies of each functional material are represented by horizontal lines[130].

Based on the mechanism of DSSC, more detailed process was discussed by Jose et al. as shown in Figure 1.25[130]. They summarized all the fundamental processes happened in DSSCs as following:

i. Photon absorption, which is determined by the absorption wavelength window, intensity of solar radiation at that window, and absorption cross-section of the dye (a).

ii. Radiative recombination, i.e., the relaxation of the excited dye directly into its ground state, and its rate constant (k_1). This process typically occurs in a time scale of several nanoseconds.

iii. Exciton diffusion length

iv. Interfacial electron transfer, i.e., injection of electron from the dye to the photoelectrode, and its rate constant (k_2). The interfacial electron transfer occurs typically in a time scale of several picoseconds.

v. Electron back transfer, i.e., the capturing of conduction band electrons by the oxidized species in the electrolyte, and its rate constant (k_3).

vi. Interfacial charge recombination, i.e., the capturing of conduction band electrons by the oxidized dye molecules, and its rate constant (k_4).

vii. Electron transport through the photoelectrode material controlled by (a) diffusion coefficient of electron (De), (b) phonon relaxation through which an electron loses its energy through electron–phonon interaction.

viii. Redox potential of the electrolyte and rate constant of (k_5) of electron transfer to the oxidized dye.

From the description of the above process, it can be concluded that how to prevent the electron recombination and electron back transfer is the key to improve the power conversion efficiency of the solar cells. In addition, although the different components of the solar cells interact together to function, metal oxide photoelectrode involves in more process than the electrolyte and dyes. The study of photoelectrode is very important for the final efficiency of the cell.

1.5.2 Characterization of DSSC

To compare different solar cells in different laboratories around the world, the efficiency of the solar cells should be measured under a set of standard conditions. The temperature of the cells should be 25°C and the total power density from the solar

radiation on the cell should be 1000W/m^2, with a spectral power distribution characterized as AM 1.5. Under the standard test conditions, there are mainly three methods to characterized DSSCs. They are photoelectric current-density/voltage measurement (J-V curves), electrochemical impedance spectroscopy (EIS) and incident photon-to-current conversion efficiency (IPCE).

There are four key parameters can be obtained from the J-V curves, which are open circuit voltage (V_{oc}), short-circuit density (J_{sc}), fill factor and power conversion efficiency η. As has introduced before, V_{oc} is determined by the difference between the Fermi level of the electrode and the electrochemical potential of the electrolyte, i.e. V_{oc} should be a constant. However, in practical, the V_{oc} is found to depend on the recombination rate of cell, as well as the sensitizer. The sensitizer absorption pattern will induce a decrease of conduction band energy of the metal oxides, thereby influencing the V_{oc}. J_{sc} is the current density when the applied voltage of the cell is zero. The J_{sc} of the cell is determined by (i) the electrochemical properties of the nanocrystalline oxides in the environment of an electrolyte, (ii) the amount of dye absorbed onto the metal oxides and (iii) the molecular structure of the dye. The FF measures the ideality of the devices and is defined as the ratio of the maximum power output to the product of V_{oc} and J_{sc}, $FF=(I\bullet V)max/(J_{sc}\bullet V_{oc})$. Ideally, the power output of the cell should be consumed by the external circuit. However, processes such as electron back transfer (k_3) and the charge combination (k_4) can lead to the degradation of cell performance by reducing FF. An ideal cell should have high internal resistance (>1000Ω), characterized by a shunt resistance. The magnitude of the shunt resistance can be calculated from the slope of the J-V curve near when the applied voltage is close to zero. High series resistance, which includes the resistance of the electrodes and the resistance of the interfacial connection, should also be a reason of low FF. The power conversion efficiency η, is defined as $\eta=P_{max}/P_{in}= J_{sc}\bullet V_{oc}\bullet FF/P_{in}$. From the equation, it is seen that higher J_{sc}, V_{oc} and FF under low solar power input are the way to increase η.

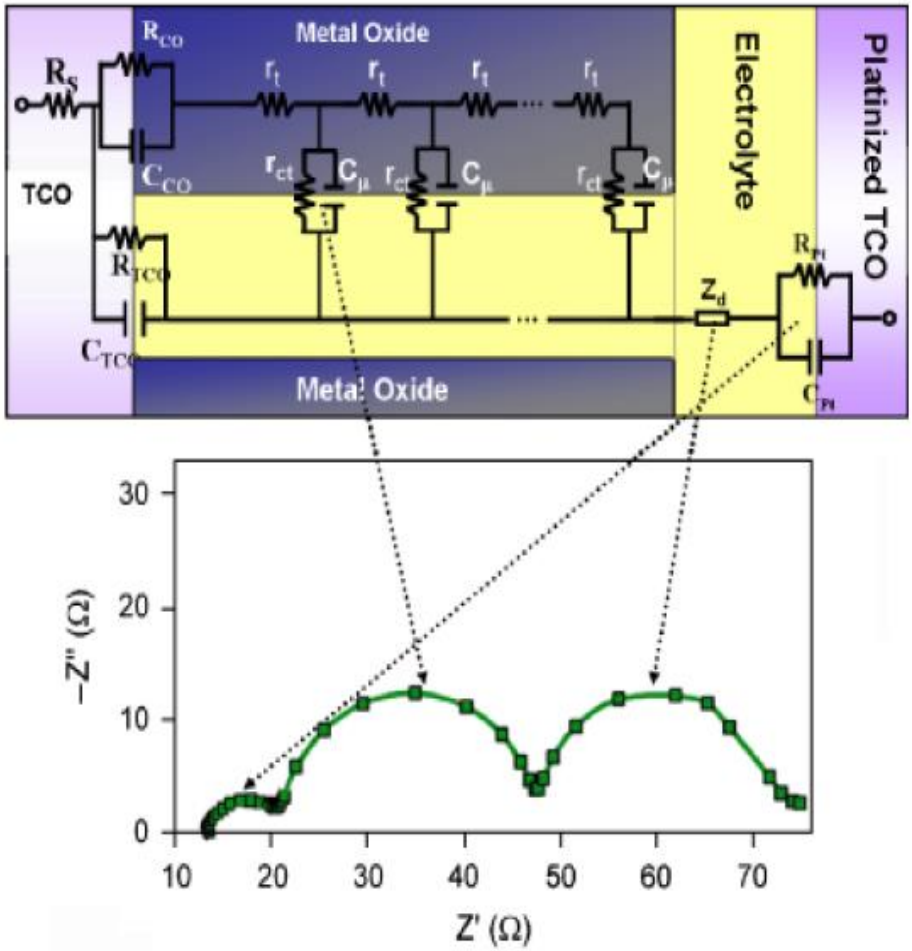

Figure 1.26 Typical impedance spectrum of DSSCs (bottom panel) in which the imaginary part of the complex impedance is plotted against the real part. The electrical equivalent circuit of DSSC (top panel) [130]

EIS is a powerful technique to examine the kinetics of the electrical transport in DSSCs. A typical impedance spectrum for DSSCs and its equivalent circuit model is shown in Figure 1.26[130]. The DSSCs can be electrically viewed as a serious of resistance and capacitors combined together. In Figure, the r_{ct} is the charge-transfer resistance of the charge recombination process between electrons in the mesoporous metal oxide film and ions in the electrolyte; C_m is the chemical capacitance of the mesoporous metal oxide film; r_t is the transport resistance of the electrons in the

mesoporous metal oxide film; Z_d is the Warburg element showing the Nernst diffusion of ions in the electrolyte; R_{Pt} and C_{Pt} are the charge-transfer resistance and double-layer capacitance at the counter electrode (platinized transparent conducting oxide plate(CO)), respectively; R_{TCO} and C_{TCO} are the charge-transfer resistance and the corresponding double-layer capacitance at the exposed CO-electrolyte interface, respectively; R_{CO} and C_{CO} are the resistance and the capacitance at the CO–TiO_2 contact, respectively; R_s is the series resistance, including the sheet resistance of the TCO glass and the contact resistance of the cell. Using IPCE, kinetic parameters, such as steady-state transport resistance through the mesoporous network, transient diffusion coefficient, chemical capacitance at the metal oxide–electrolyte interface, and recombination resistance could be characterized.

IPCE is defined as the number of electrons flowing through the external circuit under short circuit conditions per incident photon at a given wavelength.

$$IPCE(\lambda) = \frac{n_{electron}(\lambda)}{n_{photons}(\lambda)} = \frac{I(\lambda)hc}{P_{in}(\lambda)e\lambda},$$

Where I(λ) is the measured current, Pin(λ) is the input power, λ is the wavelength of the irradiation in nanometer. The IPCE is another index to evaluate the photon to electron conversion efficiency.

1.5.3 Attempts for harvesting a broader solar spectrum for DSSC

DSSCs have been extensively studied for the past two decades in order to achieve a high efficiency. Multiple methods have been explored for harvesting a broader range of light in the solar spectrum[131]. For examples, tandem structured cells were fabricated to capture more solar energy, however, the construction by stacking series of cells together had great limitation. DSSCs with different dyes for complementary solar absorption were also explored, but there were a lot of problems. For examples, if multiple dyes were applied onto one DSSC, there would probably be negative interaction between different

dyes; or if multiple-layered semiconductors with different dyes on each layer was applied, the electrons will be hard to reach the current collectors.

In order to capture a broader spectrum from solar light, it is very important to choose the appropriate dyes. Dyes are the main components to receive the photons and determine the color of the working electrode. Considering there is no single dye which is capable of responding to a panchromatic spectrum of solar energy, researchers have tried to apply more than one dye to DSSCs. The cocktail method including different dyes in a solution has been explored. For examples, Deng et al. employed tetrasulfonated gallium phhthalocyanine (GaTsPc) and tetrasulfonated zinc porphyrin (ZnTsPP) sensitizers in a single cells[132]. Strong absorption peaks from 600nm to 700nm and from 400nm to 450nm were seen for ZnTsPP and GaTsPc respectively, however, no power conversion efficiency on this cocktail cell was reported. Generally speaking, simply mixing two dyes or more in a solution for dye absorption might not be optimized for cell performance. There might be negative interaction between different dyes and it might decrease the total number of the dyes anchored in the working electrode.

Other than incorporation of multiple dyes in a cocktail solution, stepwise coating method by including different layers of metal oxides with different dyes has been manufactured. Lee et al. applied three different dyes in three different layers in a cell, by using selectively etching method as shown in Figure 1.27[133]. The current density of the cell was significantly boosted.

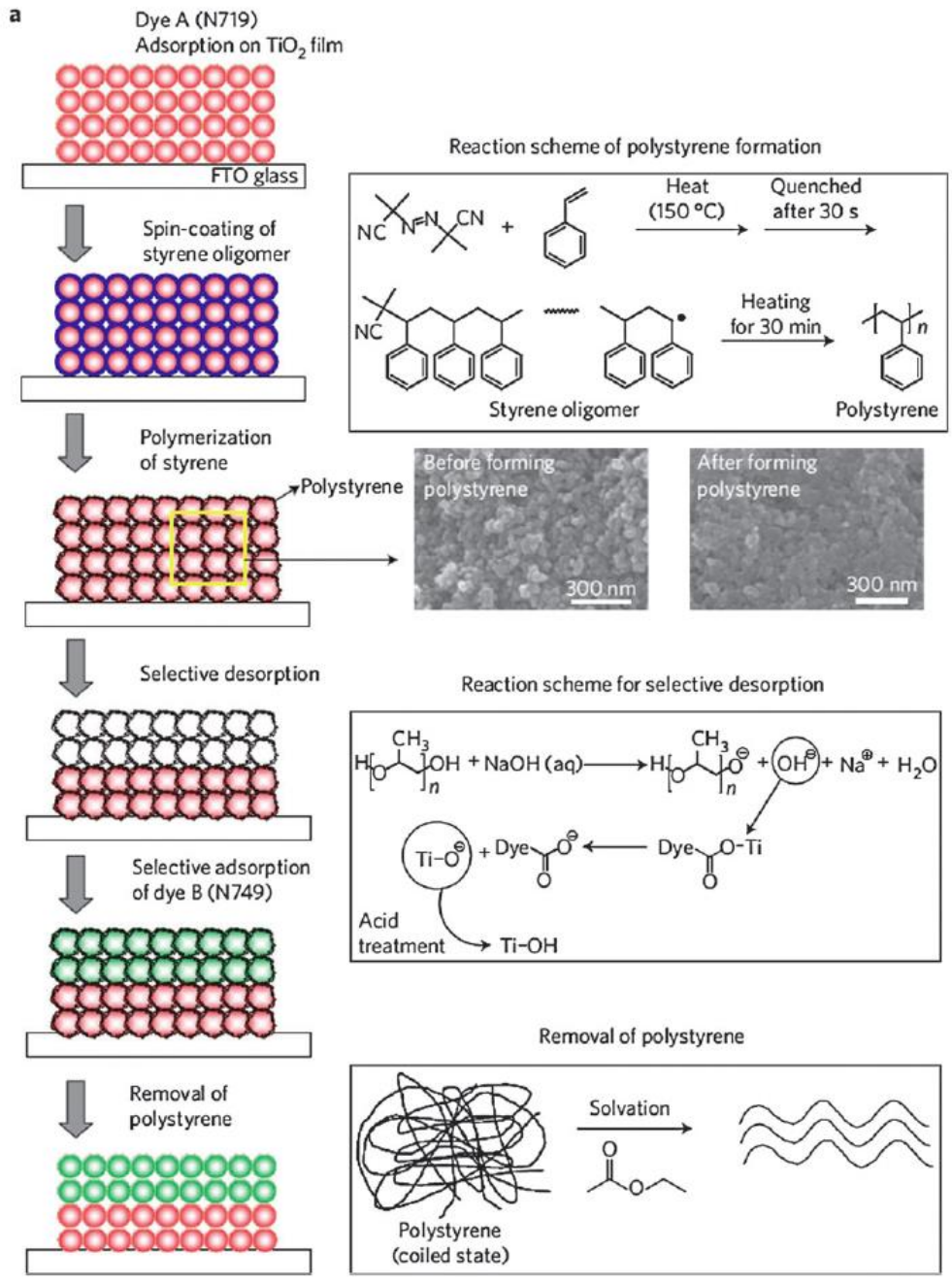

Figure 1.27 Schematic representation and reaction scheme of the bi-layer working electrode fabrication done by Lee et al.[133].

Huang et al. also introduced a "stamping" method to stack two TiO_2 layers together[134]. Two layers of TiO_2 with dyes were prepared and treated separately and then the un-pressed TiO_2 layers were transferred to the pressed TiO_2 layers as shown in Figure 1.28. Also, the dye-sensitized TiO_2 layers with and without stamping were prepared as shown in Figure 1.29.

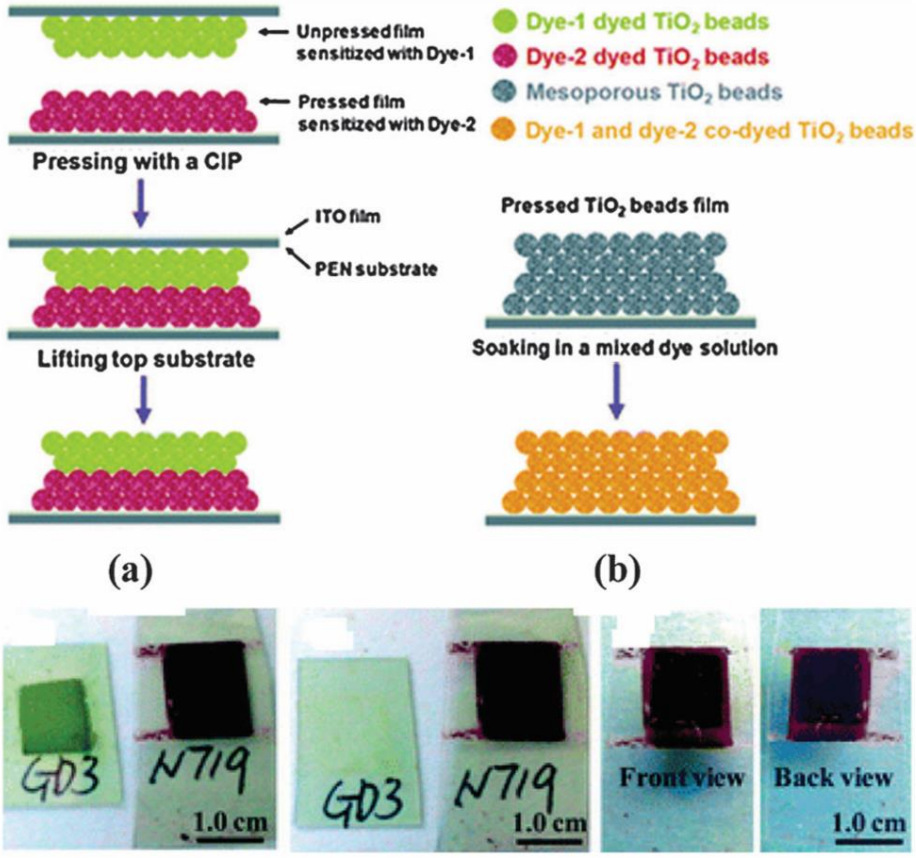

Figure 1.28 (a) Schematic representation of a double dye layer sensitized electrode prepared by the stamping method. (b) Mixed dye-sensitized electrode prepared by the cocktail method. (c) Photos of the individual GD3 and N719 sensitized films: before stamping (left); after stamping (middle); the front and back views of a combined N719/GD3 sensitized film after sintering (right)[134].

Parallel and series connected tandem solar cells aimed to broaden the harvest of the solar spectrum have also been tried in different groups. Nelles et al. fabricated a parallel connected DSSC in two different (upper and lower) compartments for the improvement of power conversion efficiency[135]. The upper compartment consisted of TiO_2 layer with red dye corresponding to longer wavelength light absorption and the lower compartment consisted of black dye sensitized TiO_2 layer corresponding to shorter wavelength light absorption as shown in Figure 1.29. The final conversion efficiency could reach as high as 10.5% with the short-circuit current density of 21.1 mA cm^{-2}.

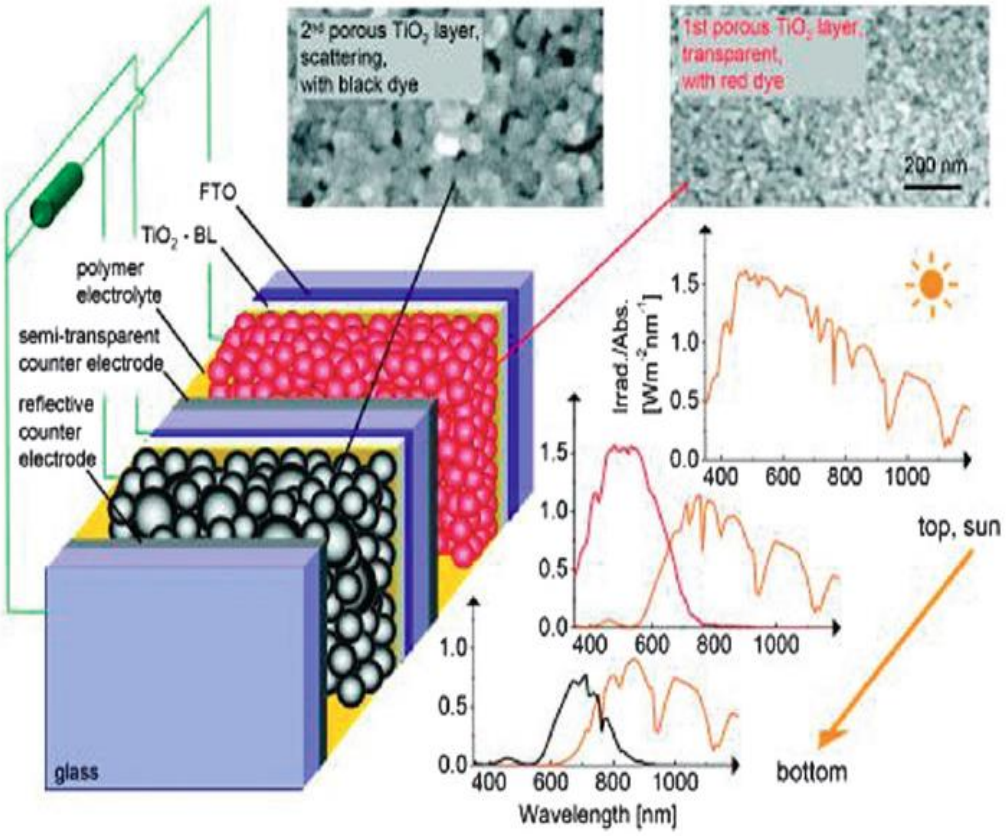

Figure 1.29 Schematic representation of parallel-connected tandem DSSCs done by Nelles et al.[135]

A novel face to face tandem DSSC was designed by Murayama and Mori, with two dye-sensitized TiO_2 working electrodes sandwiching a porous platinum counter electrode as shown in Figure 1.30[136]. The two TiO_2 working electrodes were first parallel connected and then series connected with the counter electrode. They tried to employ both homogeneous and heterogeneous dyes in the devices, and a higher current density and efficiency with heterogeneous dyes absorption were reported to be 11.4mA cm^{-2} and 3.9%.

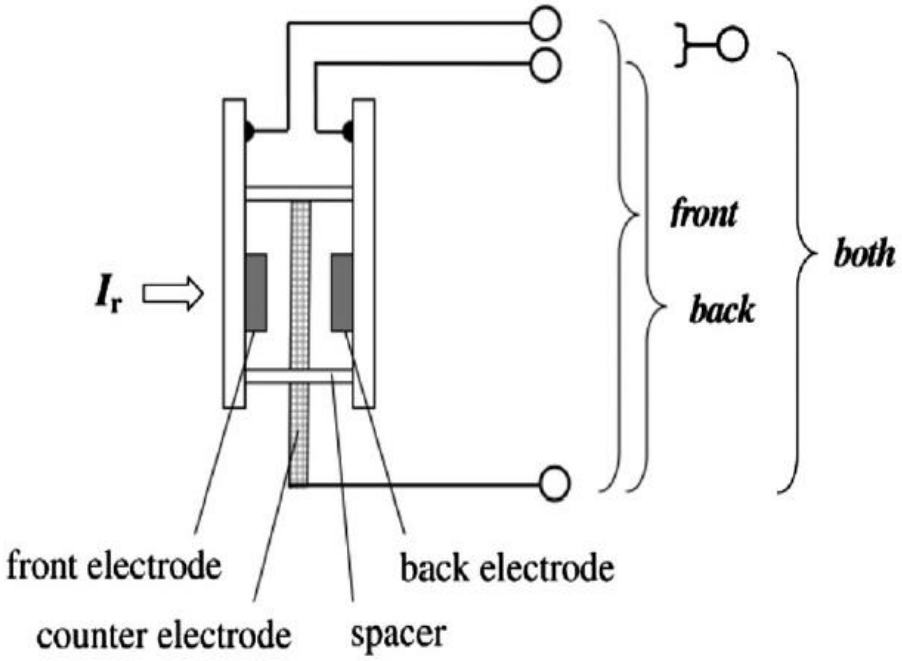

Figure 1.30 Schematic illustration of face-to-face tandem structured DSSC done by Murayama et al.[136]

In a summary, different attempts towards harvesting a broader solar spectrum have been briefly reviewed. However, each method has their pros and cons. For examples, the cocktail method will cause a negative interaction between dyes and decrease the total numbers of dye absorption in the cells. The stepwise by coating multiple layers with different dyes will be limited by the film thickness. The tandem cells

will be limited by a voltage or current density mismatch according the method of connection. Exciting improvements have been made to increase the conversion efficiency, however, optimized design and architecture are still waited to be explored and attempted.

Chapter 2

HIGHLY FLEXIBLE, TRANSPARENT PAPER-BASED IONIC DIODES FABRICATED FROM OPPOSITELY CHARGED CELLULOSE NANOFIBRILS

Abstract

Organic diodes have attracted great research interest because of their unique applications in flexible electronics. Electronic paper is one of the most attractive organic electronic devices. In this chapter, a transparent, flexible, ionic diode paper made of two oppositely charged microfibrillated cellulose (MFC) sublayers will be reported. The current rectification ratio was around 15 at ±5 V and exhibited good repeatability at room temperature. Instead of forming a depletion region to rectify current, this paper diode used asymmetric charge distribution to selectively control the ions diffusion direction. The asymmetric charge distribution inside the diode paper could selectively transport cations and anions under positive and negative bias, to allow an electric current to pass in one direction while being blocked in the opposite direction. Although the mechanism was quite different from semiconductor-based p-n junctions, the phenomenon turned out to be very similar. It was found that the moisture content, thickness of paper, scan frequency and charge density would influence the performances of the diode paper. All these factors were closely related to the ionic characteristics of the diodes.

2.1 Introduction

Junctions between p-type and n-type silicon-based semiconductors created a milestone in the development of modern electronic materials. The migration of electrons and holes across the p-n junction results in a built-in potential that only allows the current flow in a preferential direction. Such a non-linear current behavior can be utilized for signal transmission, radio demodulation, solar cells and various basic components in electronic devices. Besides the fabrication of inorganic p-n junctions, intensive researches have been focused on the fabrication of organic p-n junctions during the past two decades. Although organic electronics are not likely to surpass the silicon based micro-circuits soon in the aspect of switching speed, they have remarkable advantages of being flexible, light weight and can be environmentally friendly by using selected polymers. More importantly, some water-tolerant biocompatible organic devices can be implanted in animal or human tissues for sensing, drug release, neural-electronic integration, etc. In addition, it has been found that nonlinear current-voltage characteristics could not only happen in semiconducting material-based diodes which use electrons and holes as the charge carriers, but could also happen in polyelectrolyte which is due to asymmetric charge distribution of ions. For example, Cayre et al. reported the formation of a fixed rectifying junction by bringing together two aqueous gels containing oppositely charged polyelectrolytes. They claimed that the anisotropic distribution of positive and negative ions within the device was mainly responsible for the nonlinear current effect across the gel junction. This type of polyelectrolyte diode shed new light on exploring fabrications of diodes and made it more promising to be used in biocompatible fields.

On the other hand, contemporary society requires electronic devices to be softer and more flexible. A new focus of research is on paper and paper-like electronic devices. Cellulose, as the main component of the paper, not only is the most abundant biopolymer in the world but also has excellent mechanical properties. The diameter of MFC is usually under 100 nm and lengths can be up to several micrometers. MFC have been widely used as reinforcement nanomaterials to provide excellent load-bearing properties.

The cellulose paper can be curled and deformed fairly easily without changing much of their intrinsic properties, making them more adaptive to different shape requirements. In addition, the thin MFC paper is highly transparent, which gives it great advantages for photoelectronic applications.

In this chapter, for the first time, the wetted MFC paper with two oppositely charged sublayers which can rectify electric current is reported. The asymmetric charge distribution inside the paper will help selectively transport cations and anions under positive and negative bias, to allow the electric current to pass in one direction while being blocked in the opposite direction. Since cellulose itself is not conductive, moisture has to be in the system to help conduct current. It is found that moisture content, thickness of the paper, voltage scanning frequency and charge density play important roles in the electrical properties of this paper-based diode (PIDs). The PIDs show good long-term stability and have great potential in the fabrication of transparent, flexible, disposable, low cost switching devices and other electronic devices.

2.2 Experiments

2.2.1 Materials

Bleached kraft soft wood pulp; sodium bisulfate (Fisher Chemical); Sodium hydroxide (BDH); Urea (Alfa Aesar); 2,3-epoxypropyltrimethylammonim chloride (Aldrich); sodium periodate (Mallinckrodt Chemical Works); poly (N,N-diallyldimethylammonium chloride) (DADMAC) (Nalco company); potassium poly(vinyl sulfate) (PVSK) (Nalco company).

2.2.2 Experimental procedures

Preparation of MFC: Bleached kraft soft wood pulp was pre-soaked in deionized water and disintegrated by disintegrator. The pulp was then refined by PFI mill laboratory

beater at the resolution of 30,000. The resultant fibers were re-dispersed in water at a concentration of ca. 0.5 wt% and subjected to a high shear homogenizing process (T18 basic, Ultra Turrax, IKA Works Inc., USA) at 20,000 rpm for 30 min. The obtained fibrils suspension were diluted to ca. 0.2 wt% and further treated by Nano DeBee high pressure homogenizers for one cycle to produce the final MFC.

Synthesis of p-type MFC: The p-type MFC was prepared by a modified method reported in the literature[137]. Instead of using dissolved cellulose reported in that reference, MFC suspension was used. Because the MFC is insoluble in the reactant solution, only the surface of the MFC was modified. The morphology of the MFC was remained unchanged. First, sodium periodate was added into the MFC suspension (0.5 wt%) at a mass ratio of 50:9 at 38 ºC and pH was adjust to 4.0. The suspension was then stirred for 1h under a nitrogen atmosphere in dark. After the completion of the oxidation, the MFC was centrifuged for 4-5 times and was then dispersed in DI water. For sulfonation, the sample was treated with sodium bisulfate for 6h at 22 ºC and was centrifuged for 4-5 times for desaltation. The modification reaction can be described as

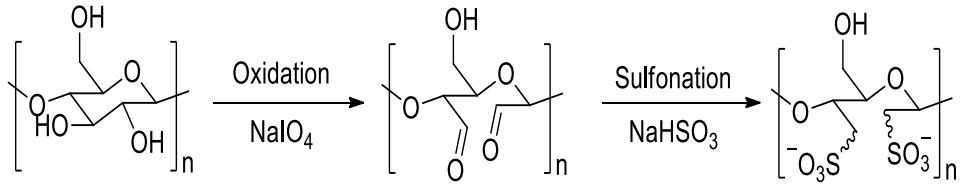

Synthesis of n-type MFC: The basic reaction mechanism is the same as reported in the literature[138]. The difference is that instead of MFC pre-treatment, MFC suspension without the NaOH/urea treatment was directly used in this study. Because MFC was insoluble in the 1% NaOH solution in this experiment, only the surface of MFC would react. The general morphology of the MFC would not be affected. The n-type MFC was prepared by a chemical reaction between MFC and 2,3-epoxypropyltrimethylammonim chloride under alkali environment. Sodium hydroxide was added to the MFC water suspension at a concentration of 1 wt%. A certain amount of 2,3-

epoxypropyltrimethylammonim chloride was then added to the system and reacted at 85 ^{o}C for 6 h. The modified MFC fibrils were centrifuged for 3 cycles to remove the sodium hydroxide, and then neutralized by hydrochloride. Finally, the modified MFC were further purified by centrifuging for at least 5 cycles.

The modification reaction can be described as

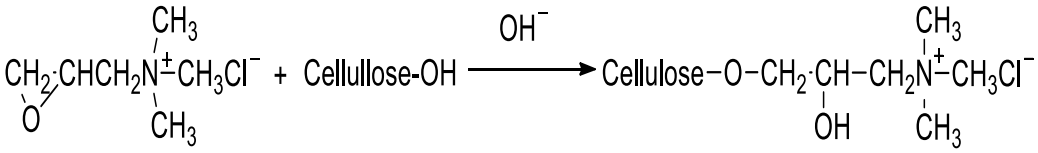

Fabrication of PIDs from p- and n- type MFC: The p-type MFC suspension was poured in a polypropylene dish and air-dried in fume hood. When the water content decreased to a certain degree, the MFC formed strong gels. Then the n-type MFC suspension was carefully poured on the top of the p-type MFC gel. A thin p-n MFC paper could be obtained after approximately 2 days air-drying. The obtained PIDs were further dried in a vacuum oven at 105 ^{o}C for 3 h.

2.2.3. Characterizations

The surface morphology of samples was examined on a LEO 1530 scanning electron microscopy (SEM) with an acceleration voltage of 8 kV. Samples were coated with Au prior to SEM observation. The surface charge density was measured by PCD-Titrator. 0.001 N poly (N,N-diallyldimethylammonium chloride) (DADMAC) and 0.001 N potassium poly(vinyl sulfate) (PVSK) from Nalco company were used as the standard solutions. Back titration method was used, i.e., polyelectrolyte (either poly DADMAC or PVSK) with opposite charge of MFC was first added into the suspension and fully stirred, and then the other polyelectrolyte was added to neutralize MFC suspension. The concentration and volume of the MFC suspension, poly DADMAC, PVSK were recorded.

An Instron 5567 universal testing machine was used to measure tensile properties of the PIDs. Samples were dried at 105 ^{o}C to constant weight and were cut into required sizes and shapes before measurement. The tests were done at ambient condition at a cross-head speed of 5 mm/min and a gauge length of 20 mm. The current versus voltage (I-V) characteristics were measured by sweeping the voltage from -5 to 5 V using a DS345 30 MHz (Stanford Research Systems) as the voltage source. The electric current signal was monitored by an SR 570 (Stanford Research Systems). The PIDs were first wetted with deionized water and then put between ITO conductive glass electrodes for the measurement.

2.3 Results and discussion

2.3.1 Morphology of the modified MFC

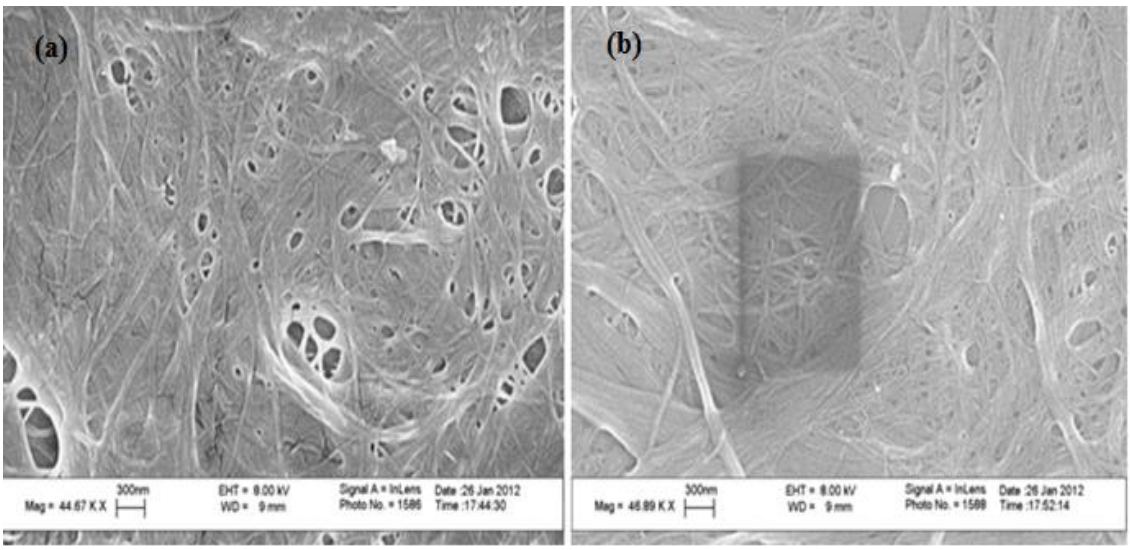

Figure 2.1 SEM images of (a) anionic (p-type) MFC; (b) cationic (n-type) MFC.

Figure 2.1a and 2.1b indicate the morphology of p-type MFC and n-type MFC. It can be seen that the fibrous structure of MFC remains after modification. The diameters of the modified MFC are in the range of 20-80 nm, which is similar to those of

unmodified MFC. Nano-sized pores are clearly shown in the photos, which are gateways for small ions to pass through.

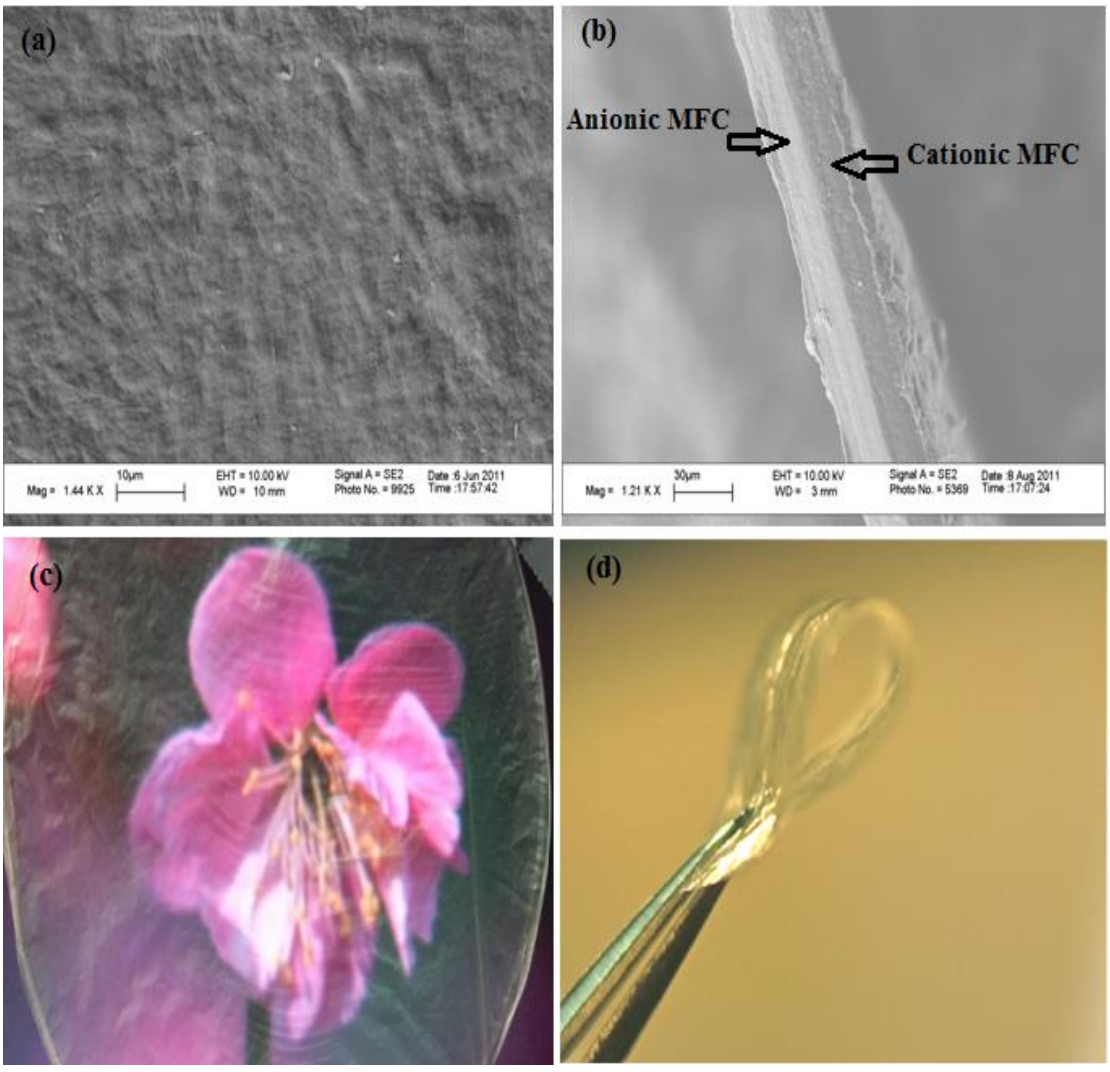

Figure 2.2 (a) Top view of low magnification of PID; (b) Cross-section of PID; (c) A 60μm thickness PID exhibits high optical transparency. (d) The PID is highly flexible under bending.

The surface morphology of PID under low magnification is shown is Figure 2.2a. The PID has relatively smooth surface. The SEM image of cross section of PID is provided in Figure 2.2b. A clear optical contrast between p-type and n-type MFC layers

can be observed. This phenomenon is possibly due to the different electric responses when electrons hit on the matters with different charges. Moreover, the positive and negative MFC layers strongly adhere to each other and no gap is observed on the border between the two sublayers. A relatively uniform and smooth texture is observed for PID.

The thin PID made in this study is transparent as demonstrated in Figure 2.2c. The colorful flower picture can be seen clearly after being covered by PID with a 60 μm thickness. Figure 2.2d indicates that the PID is quite flexible. Regular bending and folding will not cause any crack.

2.3.2 Titration results

Table 2.1 Surface charge of MFC before and after modification

Unmodified MFC	P-type MFC	N-type MFC
-40.30μeq/g	-110.7μeq/g	+80.4μeq/g

The titration results indicate that the unmodified MFC has slightly negative charge of 40.30μeq/g. This is probably because of sulfate group obtained during the process of kraft pulping. After modification, the n-type MFC shows a charge density of +80.4 μeq/g; whereas the p-type MFC shows a charge density of -110.7 μeq/g. The titration results clearly show that the positive and negative charges has successfully grafted onto the MFC surface.

2.3.3 The mechanism of the PID

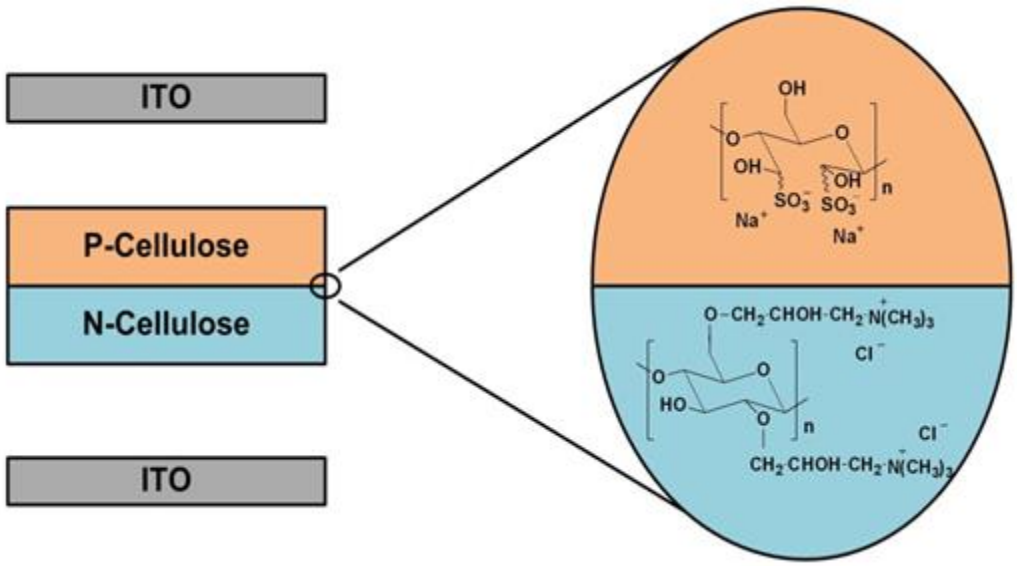

Figure 2.3 Schematic illustration of the PID setup.

Wetted PIDs were placed between two indium tin oxide (ITO) glass electrodes, and the electrical properties of the PIDs were measured. All the samples were made to have the same round-shaped area with a diameter of 0.8 cm. PIDs were soaked in deionized water for at least 2h to desalt before electrical measurements. It should be noted that the PIDs used in our measurement had been washed with deionized water, so that any impurities and ions that might come from original cellulose fibers or during the surface modification reactions were removed before the electrical measurements, except the small amount of counter ions (Na^+ and H^+ for negatively charged cellulose nanofibers and Cl^- and OH^- for positively charged cellulose nanofibrils). These counter ions form ion pairs to balance the stationary charges on the surface of MFC. Because of the attractive force between the counter ions and the oppositely charged MFC, the counter ions can only be directionally movable at relatively high electric field. Besides, the deionized water also has very low conductivity (measured as 0.3μS/cm in this experiment).

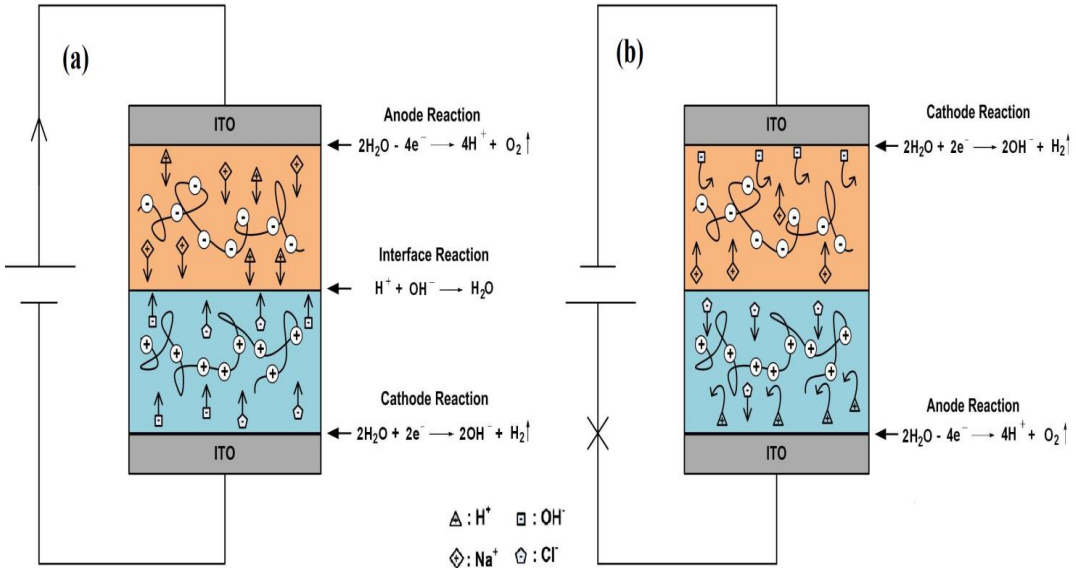

Figure 2.4 Schematic illustration of the current flow of PID under (a) forward or (b) backward bias.

The mechanism of applying positive bias (where the p-type MFC are connected to a positive electrode and the n-type MFC are connected to a negative electrode) on PID is shown in Figure 2.4a. When the energy goes high enough to overcome the barriers of electrode reactions, redox reactions of water kick off. On cathode, water molecules accept electrons from cathode to form hydrogen and hydroxide ions ($H_2O + 2e^- = 2OH^- + H_2$, $E_0 = 0$ V). The hydroxides and the possible residue counter ions (chloride) are both negatively charged, which are of opposite charge to the cationic MFC on this side. The attraction between the negatively charged movable ions and positively charged MFC makes the ions easily pass through the MFC sublayer. However, these negatively charged movable ions cannot further move to anode because of the repulsion of anionic MFC layer on the anode side. Likewise, in anode, an oxidation reaction occurs when electrons are given from water to anode to yield oxygen and positively charged protons ($H_2O - 4e^- = 4H^+ + O_2$, $E_0 = 1.229$ V). The protons and the sodium counter ions can pass through the negative MFC sublayer easily to reach the interface of two oppositely charged MFC sublayers. However, it is difficult to move further to the cathode because of the repulsion of the cationic MFC on the cathode side. At the interface of two oppositely charged MFC

layers, the protons and hydroxides will combine together to form water, which completes the circuit. On the contrast, when a backward bias (where the p-type MFC are connected to a negative electrode and the n-type MFC are connected to a positive electrode) is applied, as shown in Figure 2.4b, the protons and hydroxides generated are of the same charge of the MFC sublayers on their sides respectively, making them hard to get through. As a result, the circuit is cut off and no current flow can be measured. In this way, the current can only go in one direction while being blocked in the other direction, which gives the PIDs typical characteristics of diodes. This mechanism also explains why a single sublayer will not show diode properties.

2.3.4 Electrochemical properties characterizations

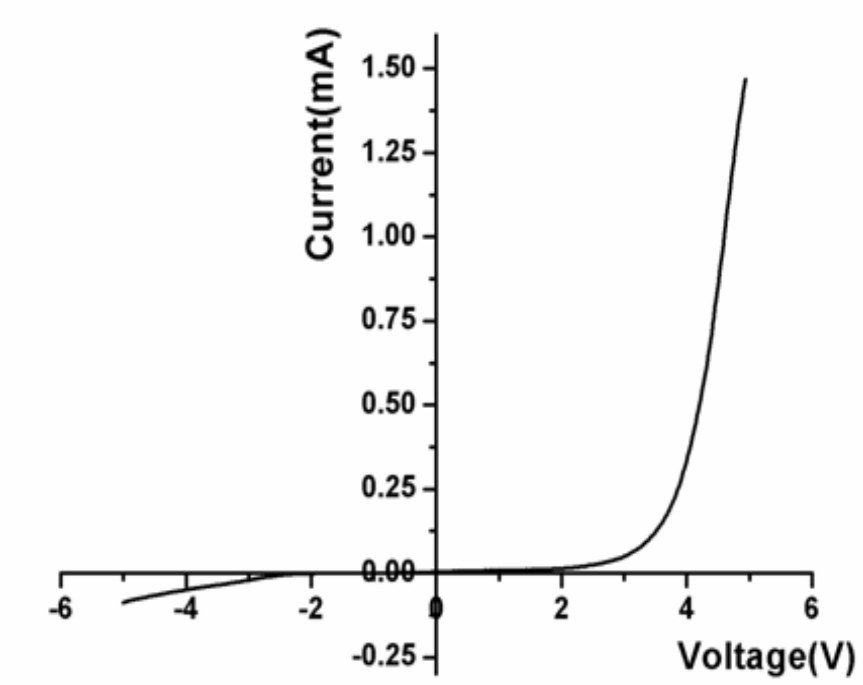

Figure 2.5 Current-voltage (I-V) plot for PID

The current-voltage curves of a typical PID are presented in Figure 2.5. Nonlinear and asymmetric current characteristics can be clearly seen with a rectification ratio of ca.

15 at ±5V. Under positive bias, the current is fairly low initially and then begins to increase significantly around 2.5 V. On the other hand, when the negative bias is applied, the current remains low (below 1.6×10^{-4} mA). The current differences between positive and negative bias endow the paper with typical characteristics of a diode.

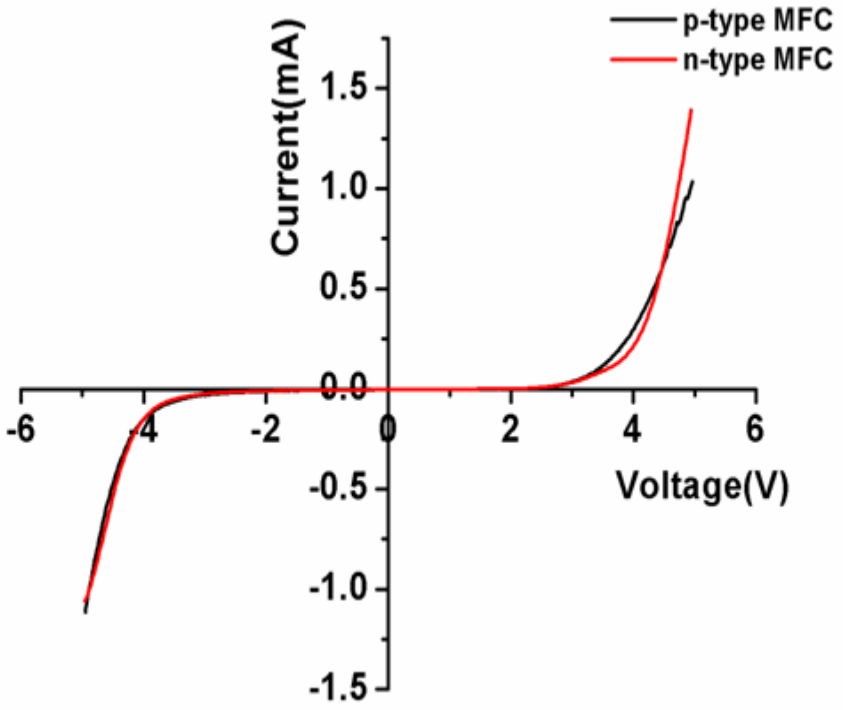

Figure 2.6 Current-voltage plots for the individual p-type and n-type MFC paper.

When the paper with only one sublayer layer (either positive or negative layer) was measured, the I-V curves appear to be symmetric about the origin and no current rectification can be observed, as shown in Figure 2.6. It can be seen that a very low current ($<3\times10^{-5}$ A/cm^2) in the wetted paper diode was observed at a bias voltage below 2.5V. However, as the bias voltage rises to pass the oxidation-reduction potential of water (1.23 V at 25 ºC at pH 7), the electrolysis of water molecules starts. At this time, as shown in Figure 2.4a and b, OH^- is produced on the cathode and H^+ is produced on anode. With the further increase of bias voltage, more OH^- and H^+ are produced which leads to an increase of current until the bias voltage is higher than 2.5 V, at which a

substantial increase of current is observed. It is noted that this substantial increase in the current occurred for both positive and negative bias if one sublayer paper is used, resulting in a symmetric I-V curve as shown in Figure 2.6. However, if the paper consists two oppositely charged sublayers, a substantial increase in the current happens only at +2.5 V, but not at -2.5 V, resulting in a typical diode I-V curve as shown in Figure 2.5. This also indicates that the asymmetric interface between the two oppositely charged MFC layers plays an important role in forming a rectifying junction.

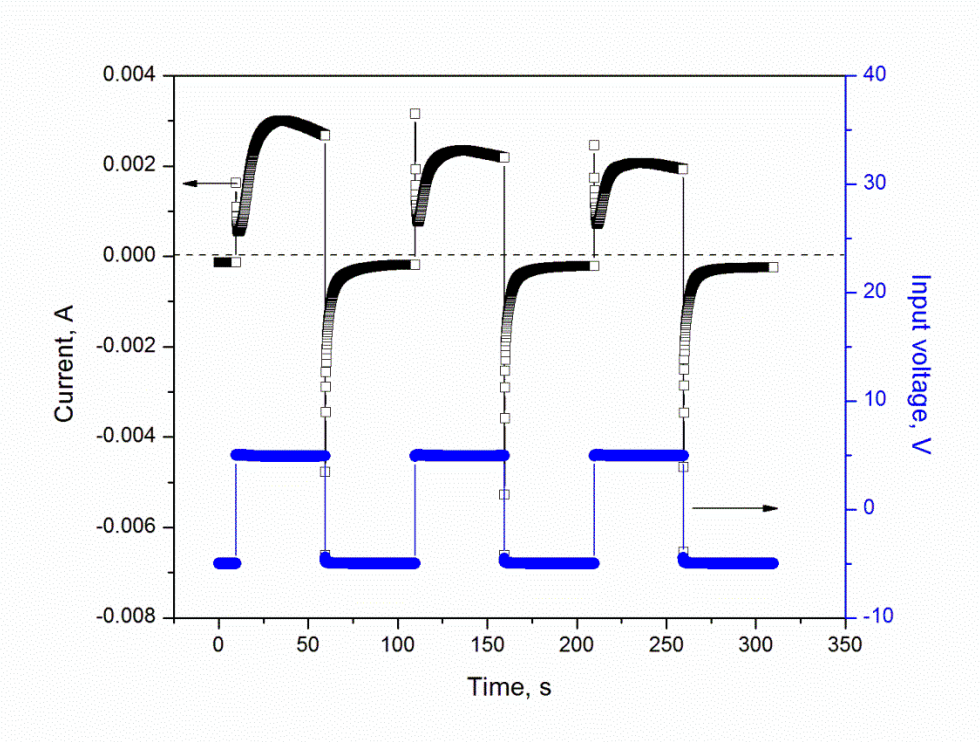

Figure 2.7 Rectifying behavior of the PID under alternative voltage at a frequency of 10 mHz, the left y axis corresponds to the upper curves, describing the measured current; while the right axis corresponds to the bottom curves, describing the applied potential.

The transient current response of PID to an alternating electric field is investigated as well. As illustrated in Figure 2.7, PID exhibits good ionic current rectification when subjected to an alternating voltage at a frequency of 10 mHz. During each voltage cycle, the current in the forward bias is significantly higher than that in the

backward bias. It is found that the current in the forward bias decades with the increase of cycles, which also leads to a decrease in rectification ratio. This is understandable because water evaporates and is also being consumed during the test. Since PID works based on the water electrolysis, the moisture content will remarkably influence the electrical behaviors of this device. However, this issue can be solved by rewetting the PID with deionized water. Testing the device in a sealed container to prevent the water evaporation will also significantly reduce the decay. In addition, it is noticed that there is a large current decay when the forward bias is switched to the backward bias (also for the voltage switching from backward to forward, though not so pronounced), which is possibly due to a transient, diffusion-controlled response to suddenly switched voltage.

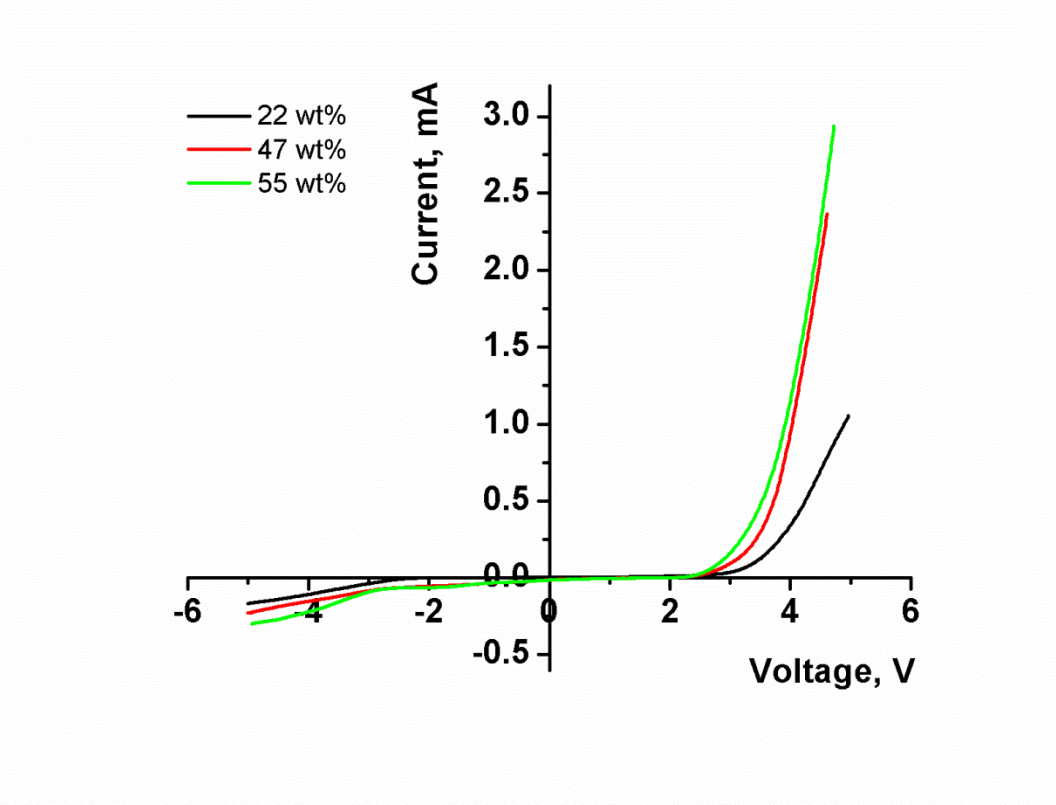

Figure 2.8 Current-voltage curves of PID under different moisture content.

The current response of PID is tested under different moisture content, which is illustrated in Figure 2.8. The samples are weighted on a high precision balance before and after they are wetted to measure the moisture content. As the moisture in the paper increases, the maximum current in both forward and backward bias increases. This is understandable because the actual conducting medium in the system is water. If the moisture content in the paper is too low, the resistance of the PID increases, resulting in low current conduction.

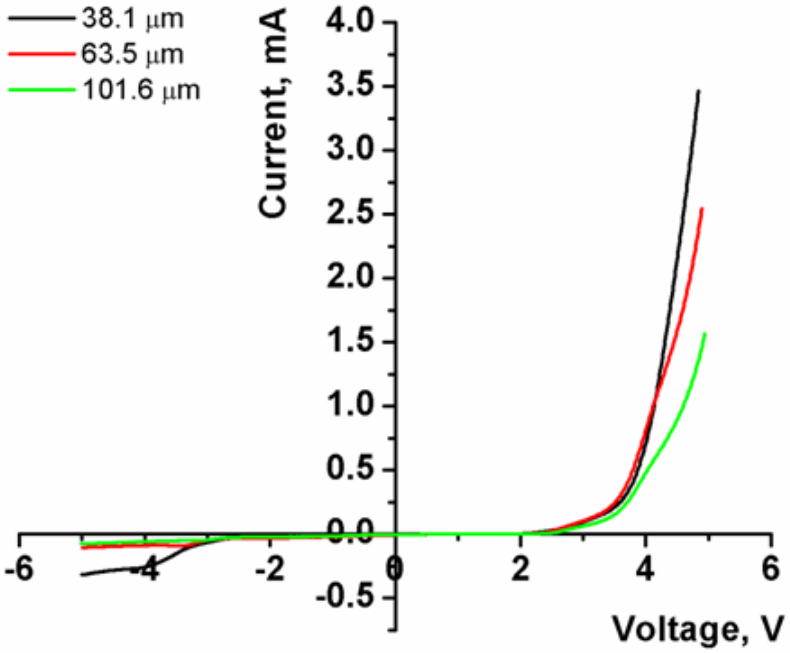

Figure 2.9 Current-voltage curves of PID at different thickness of paper

The thickness of PID can also influence their function as can be seen in Figure 2.9. With the increase of thickness, the maximum current on the forward bias decreases. This is because that the thicker the paper, the longer the distance the ions need to go through. It is also noticed that the thinner paper exhibits a lower rectification ratio. This is because a thinner layer of MFC makes it easier for some of the ions to pass through when a backward bias is applied.

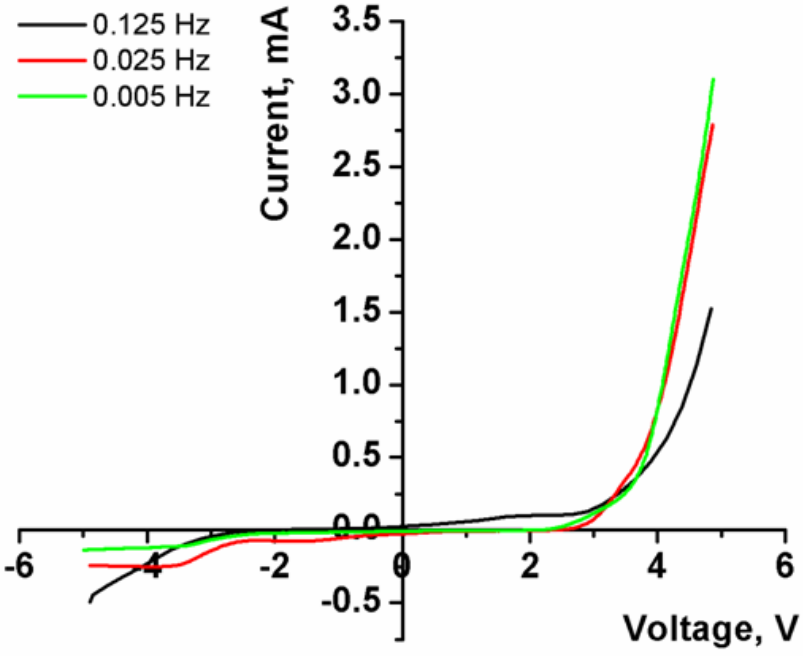

Figure 2.10 Current-voltage curves of PID at different voltage scan frequency.

The voltage scan frequency is also found to have remarkable influence on the I-V behavior of PID as illustrated in Figure 2.10. When the scan frequency increases, the maximum current becomes lower, and so does the current rectification ratio at +5 V to -5 V. The reason is that the movement of ions needs time and their motion cannot reach a steady state under a high scanning frequency. This phenomenon demonstrates the ionic characteristics of PID.

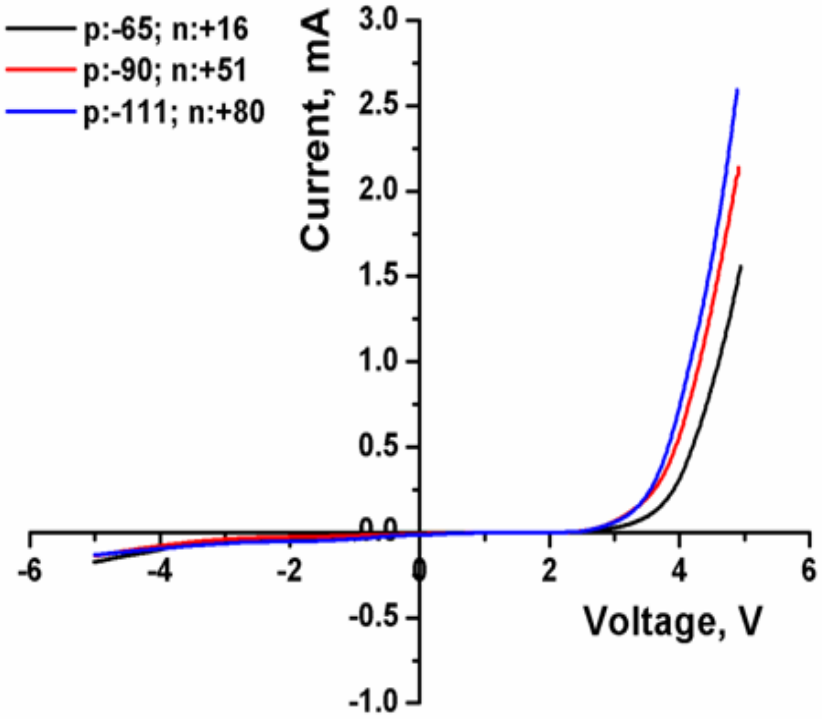

Figure 2.11 Current-voltage curves of PID at different sublayer charge density.

The charge density of MFC paper will affect the performance of PID as illustrated in Figure 2.11. The black line indicates the p-MFC and n-MFC has the charge density of -65 and +16μeq/g for the PID; the red line indicates the p-MFC and n-MFC has the charge density of -90 and +51μeq/g for the PID; the blue lack line indicates the p-MFC and n-MFC has the charge density of -111 and +80μeq/g for the PID. With the increase of the charge density, the rectification ratio will increase. That is understandable considering the mechanism of PID. As the amount of charges increase for either of p or n type of MFC, both the attractive and repellent force between the MFC backbones and charge carries(Na^+, Cl^-, H^+, OH^-) becomes more intense. That means that on the positive applied voltage, the MFC backbone will better help the ions to transport into the interfacial area; on the negative applied voltage, the MFC backbone will have a stronger force to hold back the ions trying to pass through, thus the rectification ratio is improved.

On the other hand, with the decrease of the charge density of MFC paper, the rectification ratio decrease.

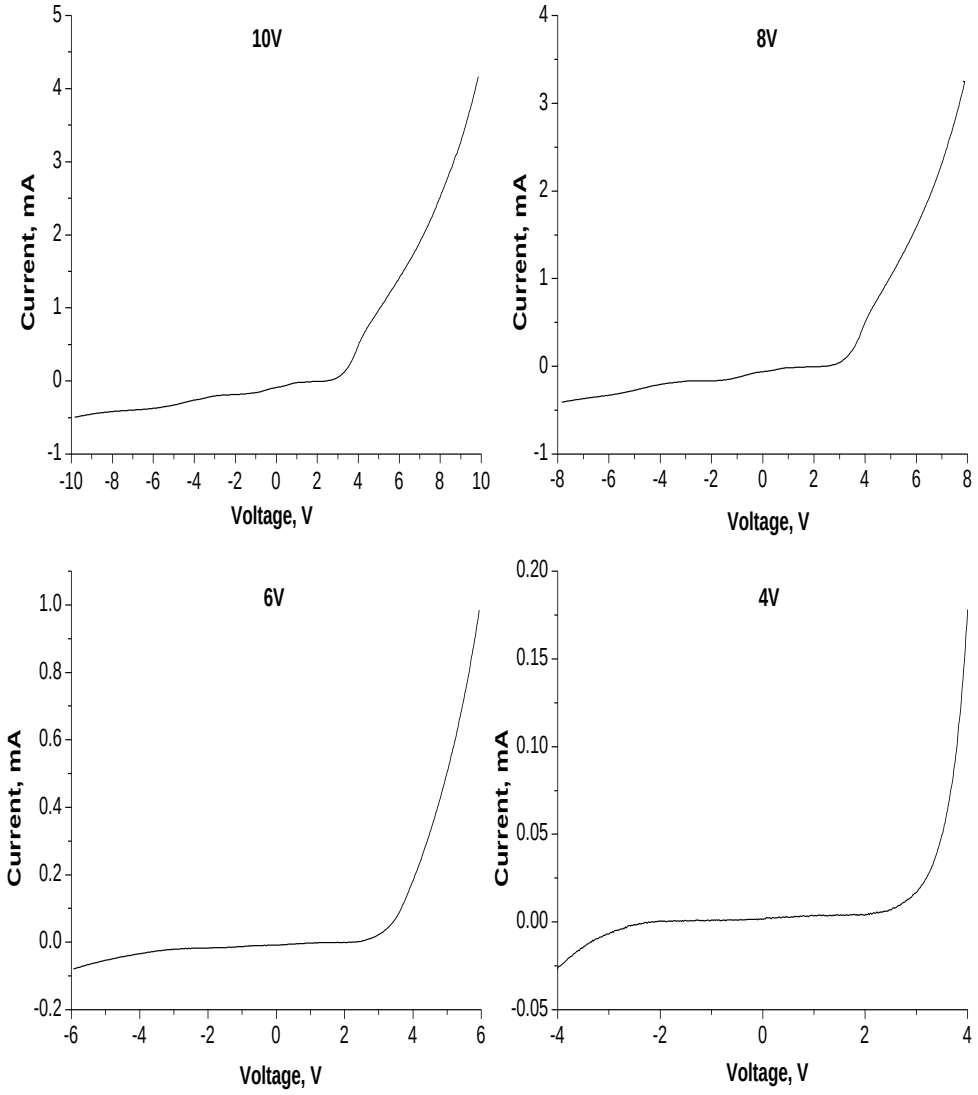

Figure 2.12 Current-voltage behavior of PID under different applied voltage. a) 10V, b) 8V, c) 6V, d) 4V.

Table 2.2 Rectification ratio, maximum current in the forward bias, maximum current in the backward bias of PID under different applied voltage

Maximum Voltage(V)	10V	8V	6V	4V
Rectification Ratio	8.3	7.9	12.4	6.6
+ Max. Current[a] (mA)	4.16	3.25	0.985	0.178
- Max. Current[b] (mA)	0.5	0.41	0.00791	0.00269

a: Maximum current in the forward bias

b: Maximum current in the backward bias

Moreover, PIDs are tested under different scanning voltages but the same moisture content (77.5 wt %), same frequency (0.01Hz), same thickness (63.5μm) and same charge density (p:-110μeq/g, n: 80μeq/g). The results are shown in Figure 2.12. The PIDs show good rectification properties, and no breakdown voltage is detected up to a scanning voltage of 10 V (the highest available scanning voltage for our equipment). The rectification ratio, maximum current in forward bias and maximum current in backward bias under different range of scanning voltages are correspondingly listed on Table 2.2. It

shows that although the rectification ratio fluctuates, the PID generally show good rectification response. With the increase of scanning voltage, both the maximum forward and backward currents increase, but the maximum current in the forward bias is always much higher than that in the back backward bias.

2.3.5 Mechanical properties characterizations

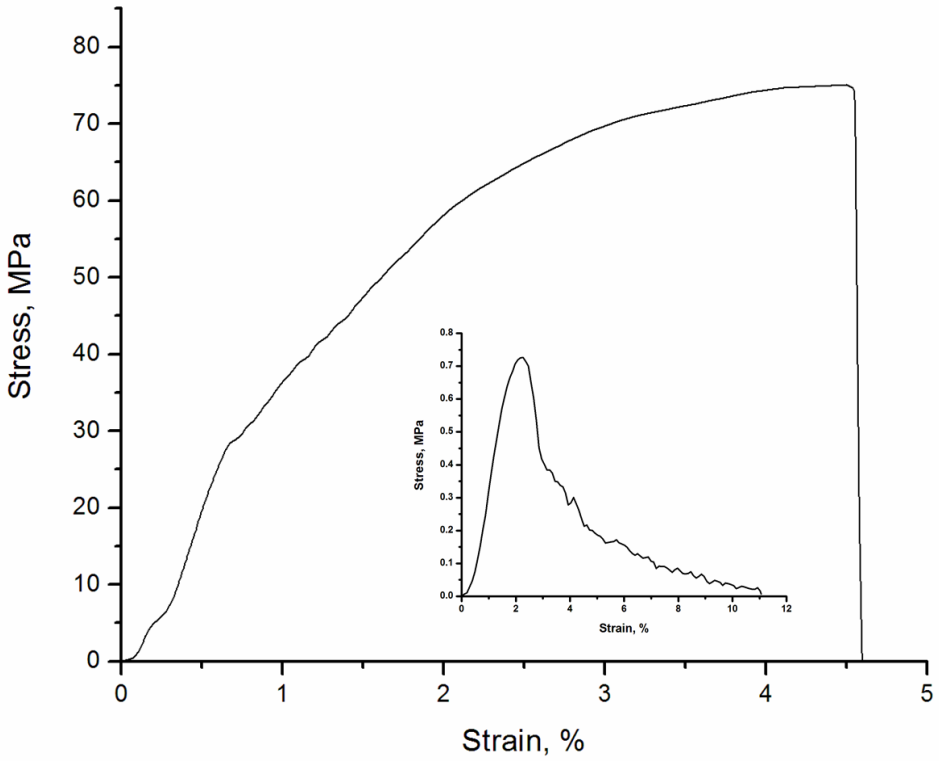

Figure 2.13 Stress-strain curve of PID. The inserted curve is for paper made from original pulp fibers through the same processing procedure.

Mechanical properties are important for the PIDs where stretch of the devices is required. A representative stress-strain curve is illustrated in Figure 2.13. For a comparison, paper made from original softwood pulp fibers is also tested as shown in the

inserted figure. The mechanical performances of PIDs are much better than the original softwood pulp fibers. The average tensile strength and modulus increase from 0.72 MPa and 0.05 GPa for original softwood fibers to 72 MPa and 4.4 GPa for PID, respectively. From the previous study, it is proved that the fiber size of PID is significantly smaller that that of original pulp. As a result, MFC in PID, due to their high specific surface area, has more contact area between adjacent MFC and is more likely to form entanglements. Morevover, more hydrogel bonding will also appear in MFC fibers than the origianl pulp. Because of the above reasons, increases in both strength and modulus for PID compared to original pulp can be observed. The prolonged strain of the original pulp fibers after yielding is due to the slippage among the long fibers inside the paper. Comparing the modules and the tensile strength of the PID (4.4 GPa and 72 MPa respectively) with other MFC reported in literatures, it is noted that the strength and modulus of the PID are lower than their counterparts (modules of 10.4-13 GPa, tensile strength of 129-214 MPa made from sulfite pulp[139, 140]). One of the possible reasons lies in the charge of PID. The charge groups on PID reduced the number of hydroxide groups and hydrogen bonding between MFC. Slightly damage of the native MFC during the chemical surface modification may be another reason for reducing the strength. In spite of this, it should be noted that the PID still show about 100 times more of tensile strength and 88 times more of modules than regular papers.

2.4 Conclusions

In summary, it is proved that PID, which is composed of two oppositely charged MFC sublayers, has good the ionic current rectification effect. The oppositely charged MFC layers play principal roles in the current rectification because they act as gateways to allow or block the ionic migration under different electric field. In addition to their unique electric properties, the PIDs are mechanically strong, low in thermal expansion, highly flexible and optically transparent, making them promising materials for future

organic electronic devices. Owing to the biocompatible and biodegradable nature, PIDs will be very promising to be used in bioelectronics.

Chapter 3

SOLID-STATE, HIGH STRENGTH PAPER-BASED SUPERCAPACITORS

Abstract

In this chapter, a novel way of fabricating solid-state, flexible, high-strength, environmental-friendly all-paper-based supercapacitors will be presented. Microfibrillated cellulose (MFC) and multi-walled carbon nanotubes (MWCNTs) were used to fabricate the electrode sheets. The solid polyelectrolyte (polyethylene oxide and lithium chloride) was doped in MFC to serve as separator layer. The specific capacitance was calculated to be 154.5 mF/cm^2 at 20mV/s from cyclic voltammetry. This value was significantly higher than most flexible supercapacitors reported in literature. The paper-based supercapacitors had excellent mechanical properties compared to the conventional liquid or gel based soft supercapacitors, with tensile strength being 1MPa and Young's modulus being 123MPa. Moreover, the specific capacitance remained the same when the supercapacitors were bent under different curvature.

3.1 Introduction

Supercapacitor is one of the main energy storage devices and is key technological enabler ranging from transportation to customer electronics. Compared to batteries, supercapacitors have advantages such as longer cycling life, higher power densities, faster charge and discharge rate and lower environmental impact[55-58, 141, 142]. Due to the space constraints and sealing problem for vehicles and portable electronics [143-

145], much effort has been devoted to develop solid-state, flexible and lightweight supercapacitors. Solid electrolyte has advantages in easy packaging and enclosure, though its conductivity is lower than its liquid counterparts[146-148]. One common category of solid electrolyte is polymeric solid electrolyte, also referred to as solid-polymer electrolytes (SPEs)[146, 148-154]. Common SPEs used in battery and supercapacitor are based on polymer-cation complex, such as polyvinyl alcohol (PVA) with inorganic acid. To fabricate solid supercapacitors, SPEs need to have a good contact with conducting electrodes. To do this, the researchers usually simply coat active electrode materials (e.g. carbon nanotubes, polyaniline, etc.) onto a SPEs layer[147, 148]. However, the active electrode materials usually have a poor bonding with SPEs, and the electrode materials will be easy to peel off, leading to the deterioration of supercapacitor properties. Furthermore, to increase the area based specific capacitance (capacitance per unit area), the coated electrode layer, such as carbon nanotubes, should be relatively thick. However, it is practically difficult to achieve a thick layer of high conductive electrode materials because the lack of bonding ability between electrode particles (such as carbon tubes or graphene). The common methods, such as coating-on, dip and dry or electrodeposition will not be able to get a rather thick electrode layer. Other category of solid electrolyte is the gel-like ionic liquid[119, 155]. The gel-like ionic liquids have high ionic conductivity, large temperature application range and high voltage stability, but their mechanical properties are less satisfactory, which will limit their use to a great extent.

Paper-based electronics have attracted much new research interest [119, 148, 156-158] because they are low-cost, flexible and mechanically-strong. Meanwhile, carbon nanotubes are calling great attention as excellent electrode materials. Multi-walled carbon nanotubes (MWCNTs) were used in our study due to their high specific surface area, high conductivity, high electrochemical stability with relatively low cost [159-161]. In this chapter, solid-state, high-strength, paper-based supercapacitors using microfibrillated

cellulose (MFC) as the skeleton materials and MWCNTs as electrodes will be investigated. The electrode sheets were made by impregnating electrode materials (modified MWCNTs) and solid electrolyte (polyethylene oxide and lithium chloride) into MFC sheets. Besides, the buried-in method can give the following advantages: (i) Effectively hold electrode materials (MWCNTs) within the electrode sheets without peeling off; (ii) Enable to make thicker sheets with more electrode materials to give higher specific areal capacitance; (iii) Provide the electrode sheets with excellent mechanical strength. The separator sheets were also made with polyethylene oxide and lithium chloride as solid electrolyte and MFC as the supporter.

3.2 Experiments

3.2.1 Materials

Bleached kraft soft wood pulp; multi-walled carbon nanotubes(mkNANO); sulfuric acid(BDH); nitric acid(BDH); polyethylene oxide (PEO, M_w=3400)(Aldrich); lithium chloride(Aldrich).

3.2.2 Experimental procedures

Oxidation of multi-walled carbon nanotubes (MWCNTs): 10g MWCNTs was stirred in a 200ml mixture of nitric acid and sulfuric acid (3:1 by volume) at 140 ^{o}C for an hour. The sample was diluted with DI water and then the oxidized CNTs were collected by centrifuge and finally dried.

Preparation of MFC/MWCNTs supercapacitor electrodes: A slurry was made with 40wt% MWCNTs, 40wt% polyethylene oxide (PEO, Mw=3400), 6.7wt% lithium chloride, 10wt% MFC in water. The slurry was stirred in room temperature for an hour and then sonicated for 10 mins. The slurry was then poured into an aluminum disk for water evaporation.

Preparation of MFC-based separator: A slurry was made with 70wt% PEO (Mw=3400), 12wt% lithium chloride and 18wt% MFC. The slurry was stirred in room temperature for an hour and poured into an aluminum disk to form sheets.

Sample Characterizations: The surface morphology of samples was examined on a LEO 1530 scanning electron microscopy with an acceleration voltage of 3kV. For the electrochemical measurement, the cyclic voltammetry curve was obtained by a two-electrode system using a DS345 30 MHz (Stanford Research Systems) as the voltage source and a SR 570 (Stanford Research Systems) as the current recorder. The galvanostat charge-discharge curve and nyquist plot was obtained by Princeton potential stat. The conductivity of the electrode and separator sheets was measured by a method of Volt-Ampere. The I-V curves were obtained by the Standford Research System. The length and width of the sheets were measured by vernier caliper and thickness was measured by Mitutoyo Caliper. The specific area and pore volume distribution of the electrode sheets were measured by BET (Quantachrome Quadrasorb SI). The samples were first degassed using Flovac Degasser for 24 hours at 50°C under vacuum and then measured by BET under high purity N_2 at 77k maintained by liquid nitrogen. The surface area and pore size distribution were determined using the Multi point BET model and DFT model respectively. The mechanical properties were measured by Instron 5567 universal testing. Samples were dried at 105 ^{o}C to a constant weight and were cut into required sizes and shapes before measurement. The tests were done at ambient condition at a cross-head speed of 5 mm/min and a gauge length of 20 mm.

3.3 Results and discussion

3.3.1 Structure of the MWCNTs/MFC supercapacitors

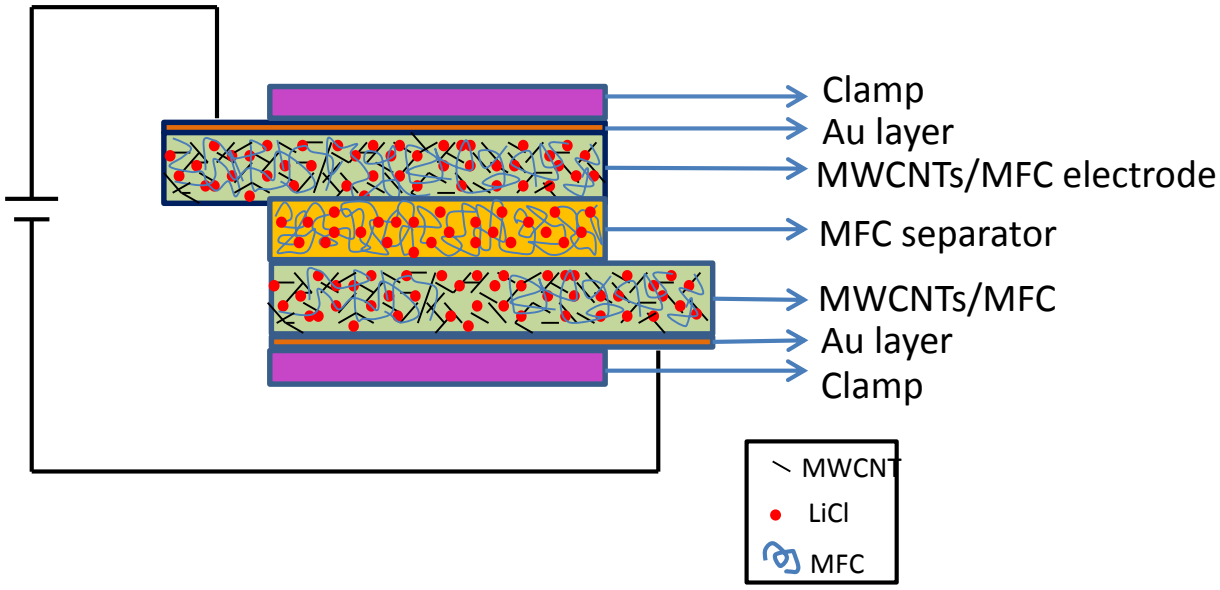

Figure 3.1 Illustration of the fabrication of MWCNTs/MFC supercapacitors

The detailed design of all paper-based MWCNTs/MFC supercapacitors is shown in Figure 3.1. The electrode paper sheets were made of modified MWCNTs as active electrode materials, polyethylene oxide (PEO) and lithium chloride as electrolyte and MFC as a supporter. The modified MWCNTs with carboxyl groups have a better compatibility with the MFC matrix. PEO with molecular weight of 3400 was chosen because of its relatively low M_w (good mobility) but solid-state characteristics. The conductivity of MFC electrode sheet was measured to be 5.2×10^{-4}S/cm. Symmetric electrode sheets were used at both sides of supercapacitors. The separator sheet was made of PEO and LiCl as electrolyte, MFC as electric isolator and supporter. The conductivity of PEO/LiCl/MFC separator sheet was 6.8×10^{-6} S/cm. A thin layer of Au was deposited onto electrode sheets to serve as current collector. Symmetric electrode sheets were used to sandwich the MFC separator. For the purpose of get stable reading, flexible plastic clamps (made of 15 layers of plastic tapes) have been used on both sides of supercapacitors to hold these layers tight and guarantee the flexibility of the whole devices.

3.3.2 Morphology of the electrode sheets and separator sheets

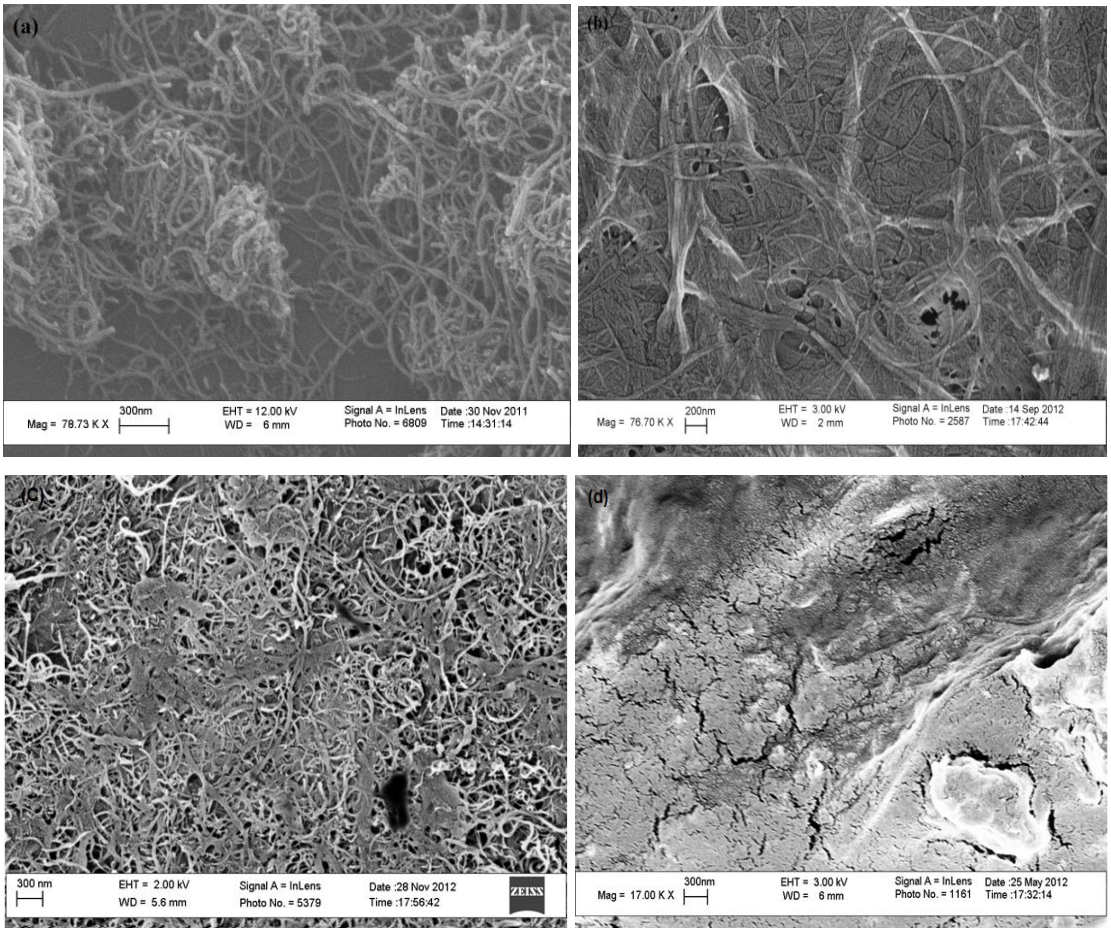

Figure 3.2 SEM image of a) Multi-walled carbon nanotubes (MWCNTs) network; b) Microfibrillated cellulose (MFC).c) MWCNTs/MFC(80:20 wt%) sheets. d) Complexion of PEO and LiCl.

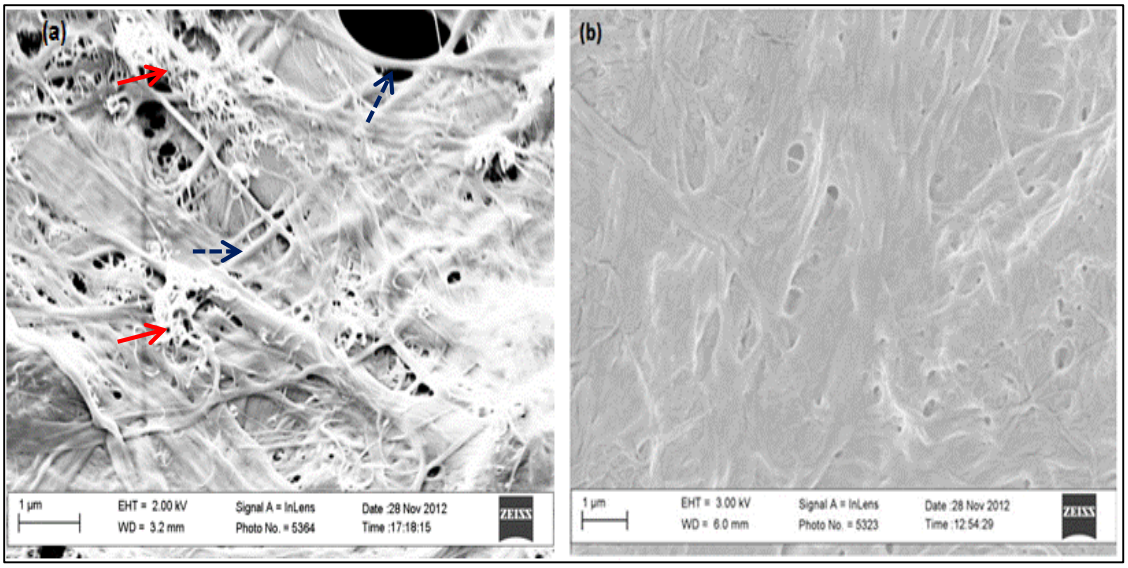

Figure 3.3 SEM images of a) electrode sheets of MWCNTs as active electrode materials, PEO and LiCl as electrolyte, MFC as sheet supporter. Solid arrows point to the representative entangled MWCNTs, dashed arrows point to the representative MFC fibers. b) separator sheets with PEO and LiCl as electrolyte, MFC as film supporter.

The scanning electron microscopy (SEM) images of individually MWCNTs, MFC, MWCNTs/MFC composites and PEO/LiCl are shown in Figure 3.2. MWCNTs are seen to tightly entangle together to form a porous network. The specific area and total pore volume of MWCNTs is 270.82m^2/g and 2.224cc/g from the BET results. MFC are observed to form a three-dimensional porous web with their diameters in nano-scale. The images of the electrode sheets made by MWCNTs/PEO/LiCl/MFC are shown in Figure 3.3a. It can be seen that under the support of MFC skeleton, the MWCNTs construct 3-D conducting nanoporous networks, meanwhile the PEO/LiCl electrolyte penetrate through the whole sheet. The specific surface area and total pore volume of the electrode sheets is 116.21m^2/g and 6.017cc/g as shown in Figure 3.4. It is important to note that the MFC is necessary because they can form a strong porous sheet to hold the MWCNTs and electrolyte but still allow the ions to diffuse in the electrode sheets. The porous and insulating nature of MFC also makes them a good candidate for separators. Figure 3.3b

shows that the PEO/LiCl electrolyte is uniformly distributed among MFC networks. MFC can prevent the electric contact between electrode sheets meanwhile leaving enough space for the ion movement.

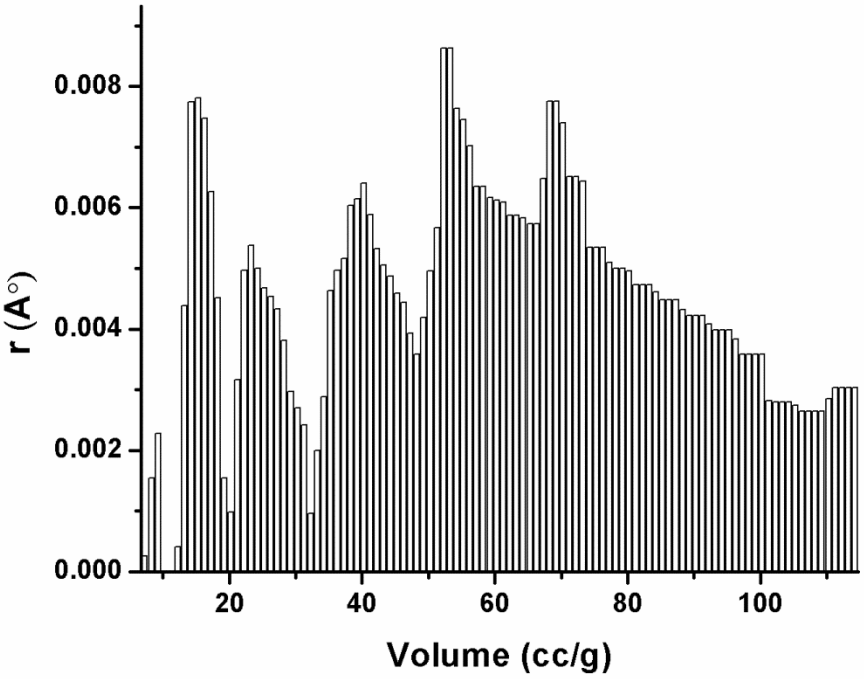

Figure 3.4 The pore volume distribution in term of pore volume (cc/g) v.s. half pore width r(Å) of electrode sheet(80wt% MWCNTs and 20% MFC).

3.3.3 Electrochemical properties of the MWCNTs/MFC supercapacitors

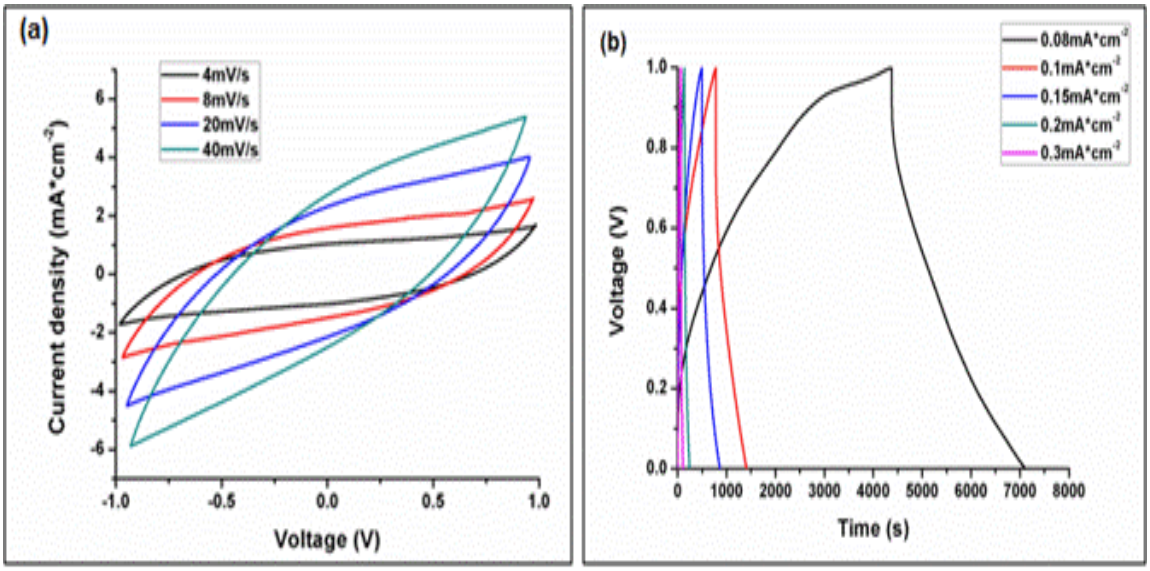

Figure 3.5 a) Cyclic voltammetry(CV) of MWCNTs/MFC supercapacitors at different scanning rates of 4mV/s, 8mV/s, 20mV/s, 40mV/s. b) Galvanostate charge-discharge curve at different current densities of 0.08mA/cm2, 0.1mA/cm^2, 0.15 mA/cm^2,0.2 mA/cm^2, 0.3 mA/cm^2.

The electrical performances of as-fabricated supercapacitors were tested using cyclic voltammetry (CV), galvanostate charge and discharge curve. Figure 3.5a shows the cyclic voltammetry of the as-fabricated supercapacitors at a different scanning rate of 4mV/s, 8mV/s, 20 mV/s, 40 mV/s. The estimated specific areal capacitance (C_s) is 154.5mF/cm2 at 20m V/s from CV plot using the following equation:

$$C_S = \frac{\int IdV}{s \times \Delta V \times r},$$

Where I is the measured current, V is the applied potential, s is the area of one electrode sheet, ΔV is the range of voltage scan, and r is the scanning rate. Our reported value of 154.5 mF/cm^2 is significant higher than other reported flexible supercpacitors (0.4 mF/cm^2-109 mF/cm^2)[118, 119, 121, 162-164] except Yuan's most recently published work of 800mF/cm-2.[148] The reason for the high Cs in our work lies on the

total amount of MWCNTs loaded in the electrode sheets. Different from other methods, the method of impregnating MWCNTs into MFC sheets adopted in this study can easily adjust the amount of MWCNTs in the electrodes. It should be noted that one of the great advantages of using MWCNTs-MFC composite electrode sheets is that the amount of MWCNTs per unit area can be easily tuned. In other word, much higher amount of MWCNTs can be loaded to electrode sheets compared to other methods (coating-on, electrodeposition, dip and dry, etc.). For example, by a simple coating method, the MWCNTs particles are not impregnated in the sheet but are simply deposited on the surface of electrode sheets. When the layer of MWCNTs is too thick, the loose MWCNTs particles will fall off from the electrode sheet. However, in our approach, MWCNTs particles are impregnated in the MFC sheet, so the fall-off of MWCNTs is no longer a problem. As a result, we can increase the amount of MWCNTs on the electrodes so a higher specific areal surface capacitance can be achieved. Galvanostat charge-discharge curves at different current densities are shown in Figure 3.5b. The specific areal capacitance calculated from the charge-discharge curve is 40.76 mF/cm^2 at the current density of 0.03mA/cm^2 with the electrode thickness of 0.19 mm. This value agrees with the C_s obtained in the CV plot.

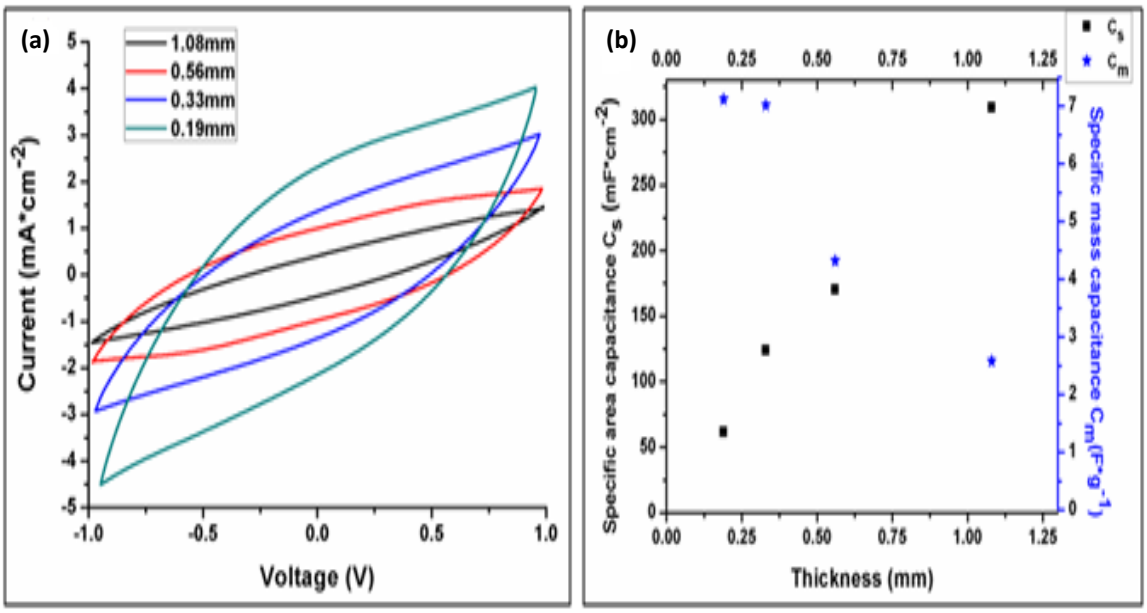

Figure 3.6 Cyclic voltammetry of MWCNTs/MFC supercapacitors at different thickness at a scanning rate of 20mV/s. b) Specific areal capacitance and specific mass capacitance with different thickness of electrode sheets.

The CV plots of supercapacitors at different electrode thickness are illustrated in Figure 3.6a. It can be observed that Cs increases with the electrode thickness. The calculated specific areal capacitance with different thickness is plotted as in Figure 3.6b. The specific areal capacitance increases from 60.1 mF/cm^2 to 304.4 mF/cm^2 as the thickness increase from 0.19 mm to 1.08 mm. But it can also be noted that the specific mass capacitance Cm decreases with the increase of thickness, which suggests that even though the total amount of MWCNTs increases with the increase of the thickness, the efficiency of MWCNTs per gram decreases. The reason is that the thicker sheets also lead to an increase of resistance, considering 15wt% of the sheets is made of the non-conductive cellulose. The increase of the resistance causes decrease of capacitance in terms of gram. Although the MFC/MWCNTs has a higher resistance than pure MWCNTs, the pure MWCNTs cannot form soft electrodes.

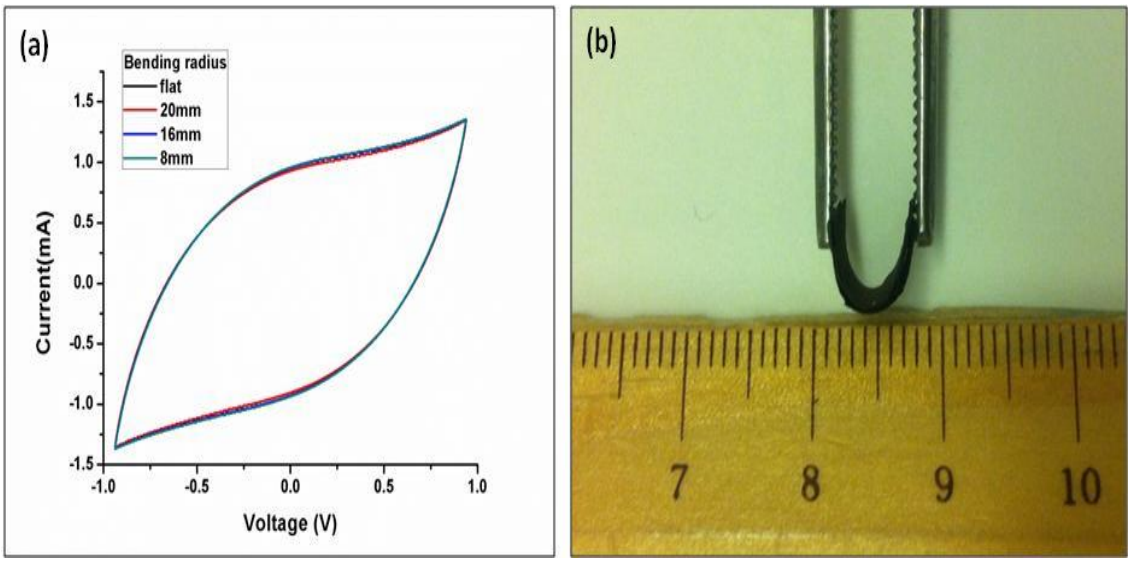

Figure 3.7 CV plots of supercapacitors at different bending radius (area of supercapacitance being 6mm*8mm). b) Photo of flexibility of the supercapacitors.

The supercapacitors are tested under different bending radius with a sheet area of 6mm × 8mm as in Figure 3.7a. It can be seen that there is almost no change in capacitance when the supercapacitors are bent from flat to a radius of 8mm. The high flexibility of the supercapacitors can also be seen in Figure 3.7b.

3.3.4. Mechanical properties of the electrode sheets of MWCNTs/ MFC supercapacitors

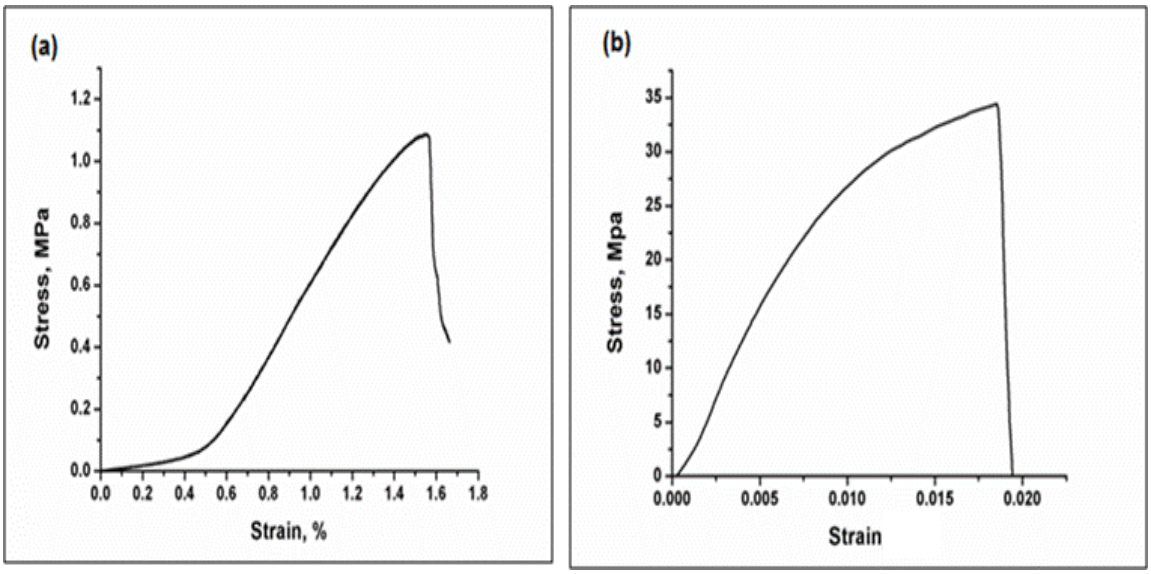

Figure 3.8 Stress-strain curve of a) MWCNTs/MFC electrode sheet; b) pure MFC sheet.

The MWCNTs/MFC supercapacitors have great advantages where mechanical strength is required. A representative stress-strain curve of the pure MFC sheet and the MFC/MWCNTs electrode sheet is illustrated in Figure 3.8. The tensile stress and modulus of the electrode are measured to be 1 MPa and 123 MPa (from the longest straight line), respectively. It is not surprising that the tensile strength and modulus of the MFC/MWCNTs electrode are much lower than that of pure MFC sheet, considering a large portion (48wt%) of the electrode sheets is made of MWCNTs and electrolyte, because MWCNTs have poor inter-particle bonding and electrolyte has very poor strength. However, the MFC/MWCNTs electrode sheet is still considered a strong paper comparable to normal papers whose tensile strength normally ranges in a few MPa[156, 165, 166]. Moreover, the mechanical properties of the MWCNTs/MFC supercapcitors are much better than the conventional liquid-based or gel-based supercapacitors.

3.4 Conclusions

In summary, solid-state, high strength paper-based supercapacitors are fabricated using multi-walled carbon nanotubes as active electrode materials, PEO and LiCl as solid electrolyte and MFC as a skeleton material. The specific capacitance of the paper-based supercapacitors can reach up to 154.5mF/cm^2 at 20mV/s from cyclic voltammetry. The capacitance remains almost the same when the supercapacitors are bent under different curvature. The mechanical properties of the supercapacitors are also satisfactory. The as-made supercapacitors can be potentially used in various areas where solidity, flexibility and high mechanical strength is required.

Chapter 4

SOLID-STATE FLEXIBLE POLYANILINE/SILVER MICROFIBRILLATED CELLULOSE AEROGEL SUPERCAPACITORS

Abstract

In this chapter, solid-state flexible aerogel supercapacitors fabricated from microfibrillated cellulose (MFC), Ag and polyaniline (PANI) nanoparticles will be reported. The electrochemical performances of PANI/Ag/MFC aerogel supercapacitors are characterized by cyclic voltammetry, galvanostatic charge-discharge curves and electric impedance spectroscopy. The specific capacitance is calculated to be 176mF/cm^2 at 10mV/s from cyclic voltammetry. This value is significantly higher than most flexible supercapacitors reported in literature. The electrochemical properties of the as-fabricated supercapacitors also remain the same when they are bent with different bending radius.

4.1 Introduction

Flexible and renewable energy storage devices are highly desired for the present society, motivated by the growing mobile market[143, 158, 167, 168]. Supercapacitors and batteries are the state-of-the-art electrical energy storage devices. Supercapacitors are preferable to batteries when high power density, fast charge and discharge rate and long

life cycles are required[55-58]. Based on the energy storage mechanism, supercapacitors can be classified into two groups, electrochemical double layer capacitors (EDLCs) and pseudocapacitors. EDLC store charges by electric double layers, for which no chemical reactions will happen[59]. In contrast, pseudocapacitors store charges by fast and reversible redox reactions. Pseudocapacitors are becoming attracting research areas because they have higher power density and can provide higher capacitance per gram than EDLCs, although their energy density and cycle life are generally slightly inferior[96, 169]. Conducting polymers, such as polyaniline (PANI), polypyrrole (PPY) are some of the common used pseudo-capacitive electrode materials. PANI is one of the most extensively studied conducting polymers because of its excellent properties, such as ease of synthesis, high electroactivity, good chemical stability, simplicity in doping and dedoping and high mechanical flexibility[147, 148, 169, 170]. In addition, when PANI is used as electrode material, its capacitance can be tuned by different factors, such as synthetic routes, morphology, amount of additives and binders used, etc. For examples, it was reported that the PANI prepared by electrodepositon generally had higher specific capacitance than the ones synthesized by chemical oxidation[96].

In the meanwhile, increasing attention on environment has driven researchers to develop more renewable, biodegradable and environmental friendly electronic devices. Cellulose, as the main component in paper, is one of the emerging renewable materials which can be used for electronic devices[119, 146, 156, 158, 171, 172]. Cellulose has the advantages of wide-spread availability, low cost, renewable, biodegradable, biocompatible, and highly flexible [11, 12, 173, 174]. Some explorations of using cellulose paper on supercapacitors have been reported in literatures. For example, Razaq et al. in-situ chemically synthesized polypyrrole on to Cladophora nanocellulose to make composite electrodes for supercapacitors, with a specific capacitance of 60-70F/g[175]. Zheng et al. designed paper-based electrodes for supercapacitors in a way of drawing graphite onto cellulose paper, showing an areal capacitance of 2.3mF cm^{-2}.[164] These

researches provided inspiring work for cellulose-based supercapacitors, but the capacitance of cellulose paper-based supercapacitors is low. Porous materials have been used to improve the performances of the supercapacitors. Chen et al. reported sponge supercapacitors with MnO2 and carbon nanotubes as electrode materials and the specific capacitance was very competitive[176]. Their work demonstrated that aerogel could serve as an excellent candidate for supercapacitor substrates. MFC based aerogel has the advantages of high porosity, biodegradable, large specific surface area, low density and better impact buffer[177, 178]. Theoretically, MFC based electronics can be disposable because of their biodegradability. With these advantages, it is very promising that MFC aerogel will have extraordinary performances as electrode substrates for supercapacitors. However, cellulose itself is insolating, so the MFC aerogel must be modified to be conductive. A simple and effective way to solve this problem is to coat conductive materials onto the surface of cellulose. Silver particles are highly conductive materials and have various applications in conductive wires, conductive adhesives and various electronic components[179-181]. It has also been reported that silver nanoparticles can be stabilized by cellulose[182-185]. Silver particles have been used in supercapacitors serving as conductors to form electron transfer-channels between the electrolyte and electrode materials. For example, Zhang et al. reported that an increase of about 300% was achieved by incorporating of Ag particles onto MnO_2 nanosheets[186]. Huang et al. claimed that by incorporation of Ag particles into CuO sheets, the capacitance nearly doubled than those of pure CuO sheets[187].

In this study, Ag particles were in situ deposited on MFC aerogel, which created conducting channels in the aerogel. To achieve high capacitive performances, PANI nanoparticles, as the electrode materials for charge collection, were further deposited on the surface of Ag particles. The PANI/Ag/MFC aerogel was then assembled by solid-state PVA/H_3PO_4 solid electrolyte to fabricate flexible supercapacitors. The specific capacitance was calculated to be 176mF/cm^2 at 10mV/s from cyclic voltammetry. The

electrochemical properties of the as-fabricated supercapacitors also remained the same when they were bent with different bending radius.

4.2 Experiments

4.2.1 Materials

Bleached kraft soft wood pulp; silver nitrate(Alfa Aesar); sodium borohydride(J.T. Baker); aniline(Alfa Aesar); sulfuric acid(BDH), polyvinyl alcohol(Aldrich), phosphoric acid(J.T. Baker).

4.2.2 Experimental procedures

Preparation of MFC aerogel: Bleached kraft softwood pulp was pre-soaked in deionized water and disintegrated by disintegrator. The pulp was then refined by PFI mill laboratory beater at the resolution of 30,000. The resultant fibers were redispersed in water at a concentration of ca. 0.5 wt% and treated by Nano DeBee high pressure homogenizers for three cycles. Then the fibers were subjected to a high shear homogenizing process (T18 basic, Ultra Turrax, IKA Works Inc., USA) for 30 min to get the final MFC suspension. The MFC suspension was then concentrated to 1.5wt% and suddenly quenched by liquid nitrogen. The frozen MFC samples were put into a freeze dryer until all the water was sublimed.

Coating Ag on to MFC areogel: The above prepared MFC aerogel was cut into small ribbons with the thickness of 1mm. 0.05g MFC aerogel ribbons and 1.86g silver nitrate was added into 10ml deionized water. The above MFC/silver nitrate mixture was magnetically stirred in an ice bath. 2.07g sodium borohydride was added into 10 ml deionized water in another beaker and was added into the MFC/silver nitrate suspension drop by drop. The reaction was stopped 10 min after all the sodium borohydride was added into MFC/silver nitrate mixture. The Ag/MFC aerogel was taken out and washed

with deionized water for three times. These procedures were repeated for five times to get the final Ag/MFC aerogel.

Electrodeposition of PANI onto Ag/MFC aerogel: The electrodeposition of PANI on Ag/MFC was performed in a solution of 1M aniline and 1M H_2SO_4. Two-electrode system (Stanford research systems DS345 and SR570) was employed. A deposition current density of 5mA/cm^2 was used. Different amount of PANI was controlled by deposition time at 5min, 10min, 15 min and 20min. The mass of PANI was calculated from the total Faradic charge consumed by assuming an average of 2.5 electrons per aniline monomer in the electropolymerization.

Sample Characterizations: The surface morphology of samples was examined on a LEO 1530 scanning electron microscopy with an acceleration voltage of 3kV. For the electrochemical measurement, the cyclic voltammetry curves were obtained by a two-electrode system using a DS345 30 MHz (Stanford Research Systems) as the voltage source and a SR 570 (Stanford Research Systems) as the current recorder. The galvanostatic charge-discharge curves and Nyquist plot were obtained by Princeton potential stat. All the electrochemical tests were performed with Pt foil as current collector at both sides of supercapacitors. The conductivity of the electrode and separator sheets was measured by a four-point probe system. The specific area of MFC aerogel was measured by BET (Quantachrome Quadrasorb SI). The samples were first degassed using Flovac Degasser for 24 hours at 90°C under vacuum and then measured by BET under high purity N_2 at 77k maintained by liquid nitrogen. X-ray diffraction (XRD) analysis was performed on X'Pert PRO diffractometer(PANanalytical BV) with Cu Ka radiation.

4.3 Results and discussion

4.3.1 Structure of the PANI/Ag/MFC supercapacitors

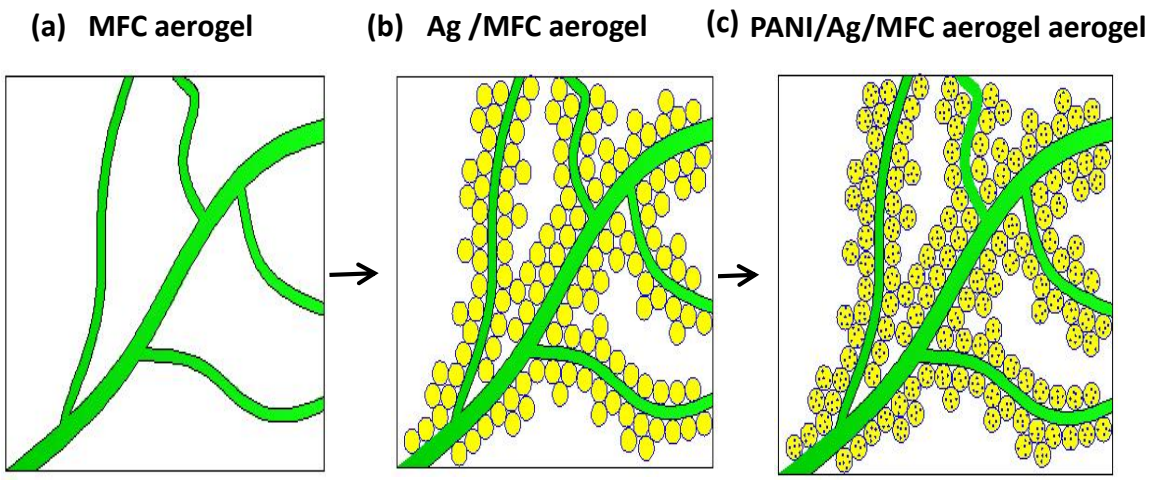

Figure 4.1 Fabrication process of PANI/Ag/MFC aerogel electrodes. (a) MFC aerogel; (b) Ag particles were in-situ synthesized onto MFC aerogel; (c) PANI was electrodeposited on to Ag/MFC aerogel.

The fabrication process of PANI/Ag/MFC aerogel electrodes consists of three steps as demonstrated in Figure 4.1. First, MFC aerogel was prepared by freeze drying of 1.5wt% MFC aqueous suspension. The density and specific surface area of as-made MFC aerogel were measured to be 1.2g/cm^3 and 30m^2/g respectively. The specific surface area of the aerogel used in this study was lower than 70-110m^2/g that was reported previously[178]. The main reason was that an aerogel with relatively high strength was needed in this study. Therefore, a higher concentration of MFC in the solution was used in aerogel preparation, which resulting in higher density and lower specific surface area compared to these reports in our previous work. The MFC aerogel was then cut into small ribbons with thickness of 1mm. The photo of as-made MFC aerogel and its small ribbons are shown in Figure 4.2.

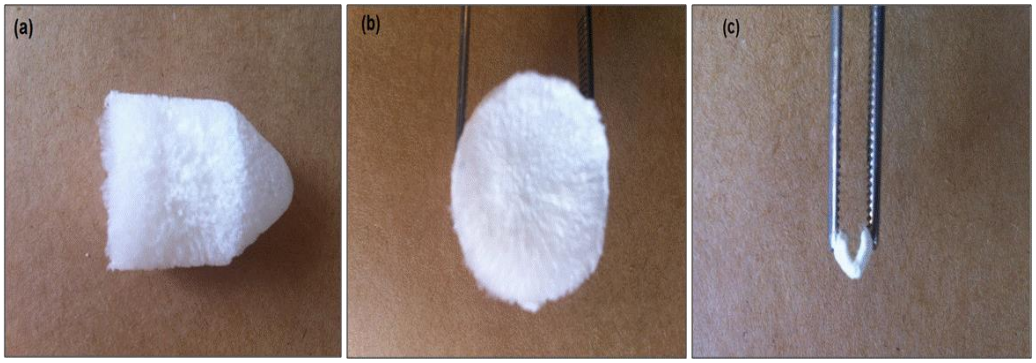

Figure 4.2 Photo of (a) side view of MFC aerogel; (b) cross section of MFC aerogel; (c) flexibility of MFC aerogel ribbon.

Next, Ag particles were in situ-synthesized on to the MFC to make conductive MFC aerogel. The sheet resistance of Ag/MFC aerogel was measured to be 1Ω/square using a four-point method. PANI was subsequently electrodeposited onto the Ag/MFC aerogel as the electrode material to make PANI/Ag/MFC aerogel electrodes. In order to study the effect of the amounts of PANI on the performances of supercapacitors, different electrodeposition time (5, 10, 15 and 20 min) of PANI on Ag/MFC aerogel was adopted. After preparing PANI/Ag/MFC aerogel electrodes, the solid state and flexible PANI/Ag/MFC aerogel supercapacitors were assembled, as illustrated by Figure 4.3. The PANI/Ag/MFC aerogel electrodes and separator sheet were immersed into the polyvinyl alcohol (PVA)/phosphoric acid (H_3PO_4) solution to fully absorb the electrolyte. The supercapacitors were then assembled by sandwiching the separator sheet between two identical PANI/Ag/MFC aerogel electrodes and then fully dried in room temperature to make integrate devices.

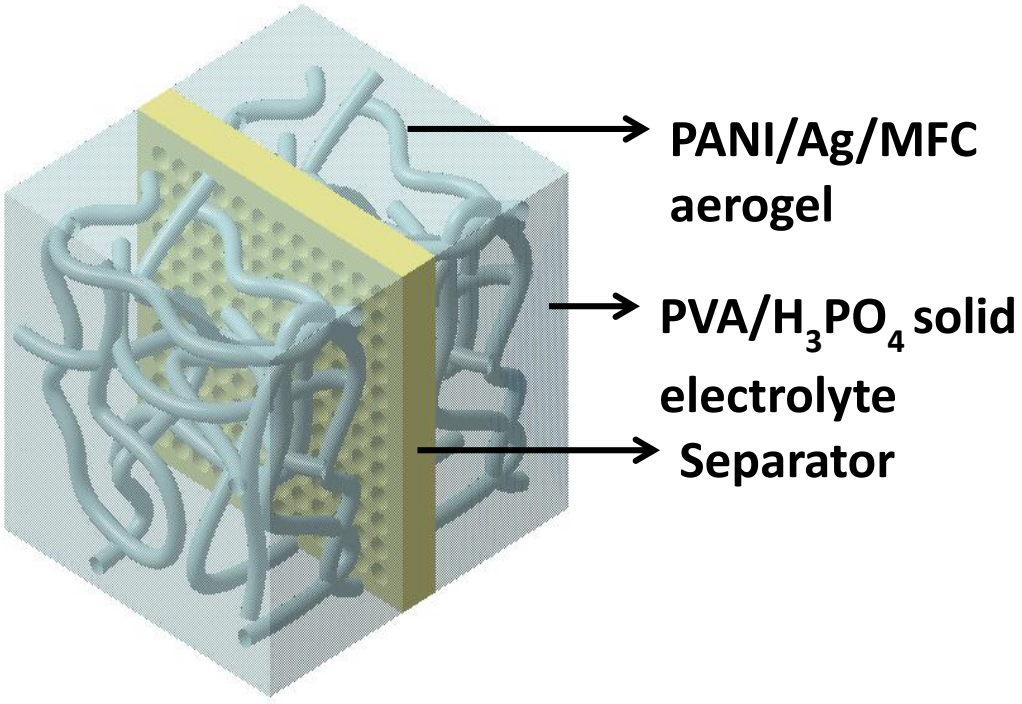

Figure 4.3 Fabrication of PANI/Ag/MFC supercapacitors.

4.3.2 Morphology and characterizations of the electrode sheets

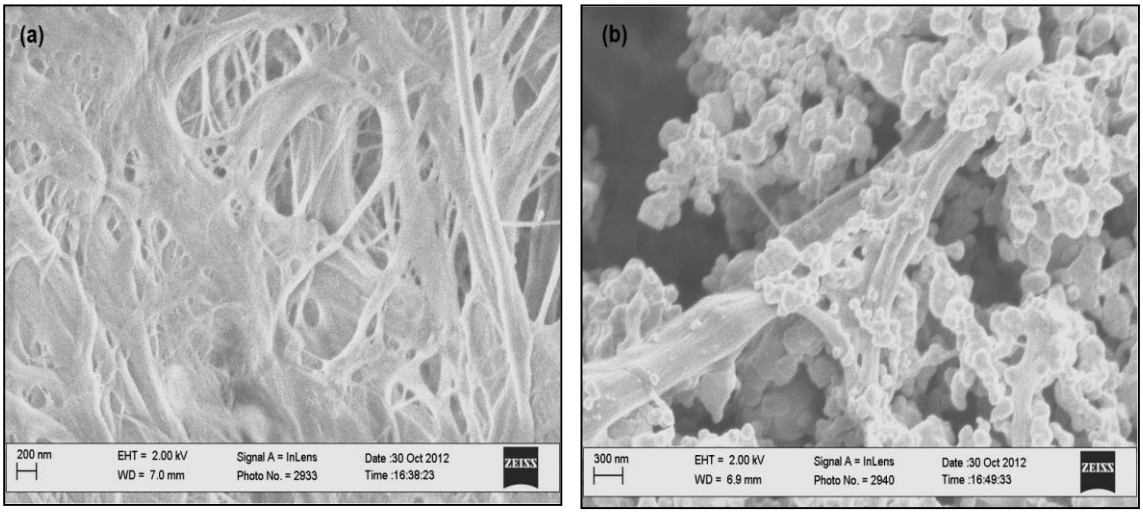

Figure 4.4 Scanning electron microscopy of (a) MFC aerogel; (b) Ag/MFC aerogel

Scanning electron microscopy of MFC aerogel and Ag/MFC areogel are shown in Figure 4.4a and 4.4b. It can be observed from Figure 4.4a that the MFC constructs a highly porous network. The diameters of the fibers are in mirco/nano-scale, which

provide high specific surface area for the skeleton of the supercapacitors. Figure 4.4b shows Ag particles are successfully coated on MFC aerogels for Ag/MFC aerogel. The sizes of Ag particles range from tens to hundreds of nanometers, and are randomly distributed in the aerogel with a branch-grape structure.

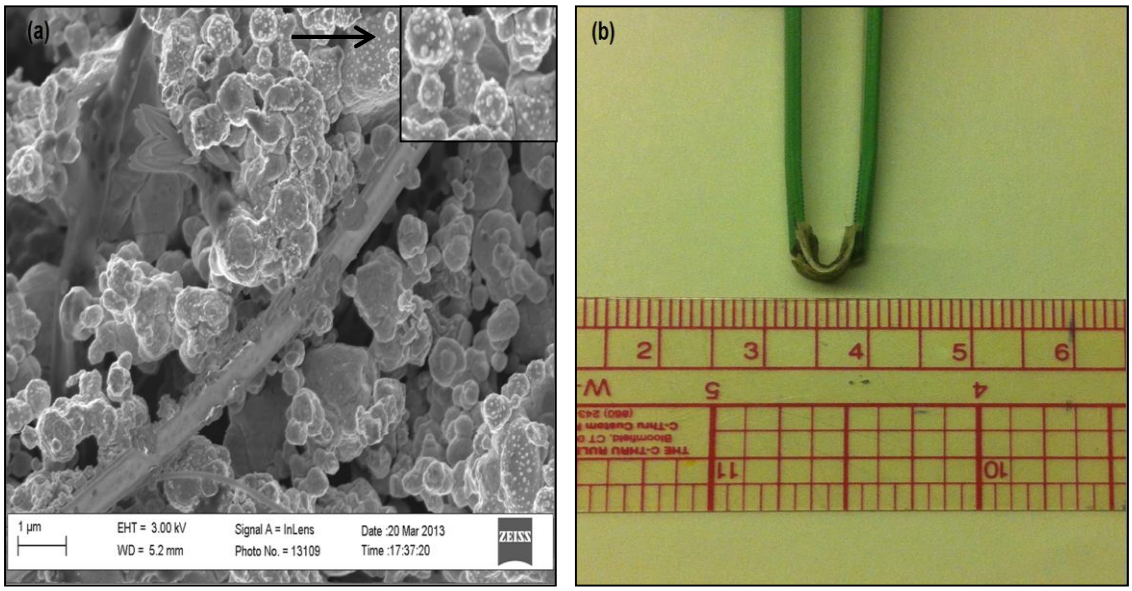

Figure 4.5 Scanning electron microscopy of PANI/Ag/MFC aerogel. (b) Photo of PANI/Ag/MFC aerogel.

Electrodeposition of PANI on to Ag/MFC aerogel was subsequently performed. SEM image of PANI/Ag/MFC aerogel is shown in Figure 4.5a. PANI in shape of nano-dots is deposited on Ag particles (see the inserted enlarged photo), while no deposition of PANI can been seen on MFC. This is reasonable because Ag particles are conductive but MFC is insulating. As a result, the electrodeposition of PANI can only happen on conductive Ag particle surface. The PANI is the actual electrochemically reactive material for the supercapacitors for charge storage while the Ag particles provide high electrically conductive channel for fast charge transportation. The photo of as fabricated PANI/Ag/MFC aerogel is shown in Figure 4.5b. The two electrode sheets and the

separator sheets are adhesive to each other by the solid electrolyte to form an integrated device. The supercapacitors are solid-sate and quite flexible under bending.

4.3.3 Characterizations of Ag contents on the electrode sheets

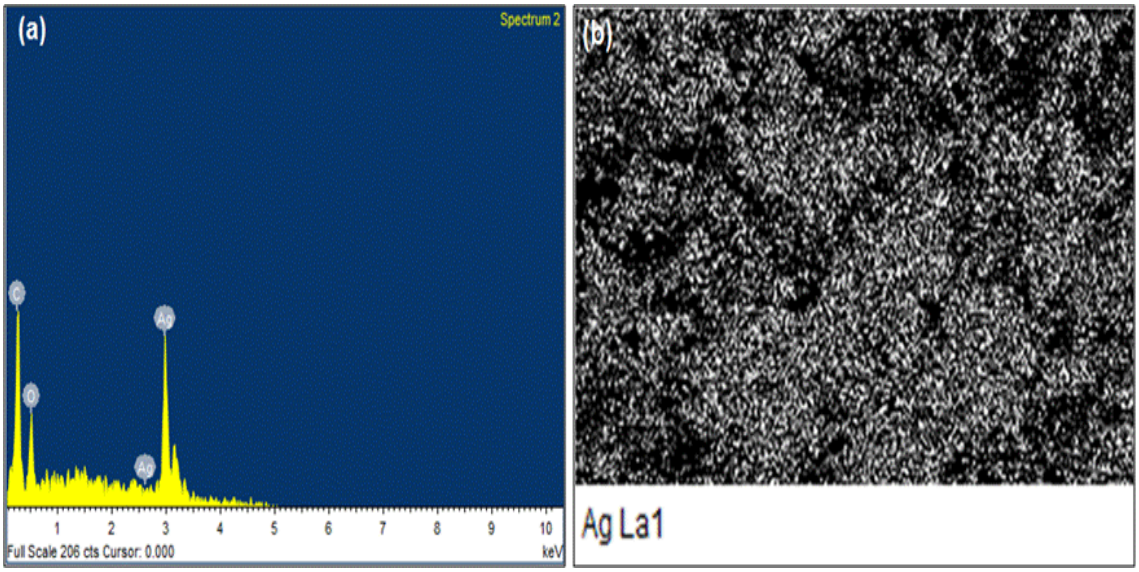

Figure 4.6 EDS analysis of Ag/MFC aerogel. (b) EDS mapping of Ag dispersion in Ag/MFC aerogel.

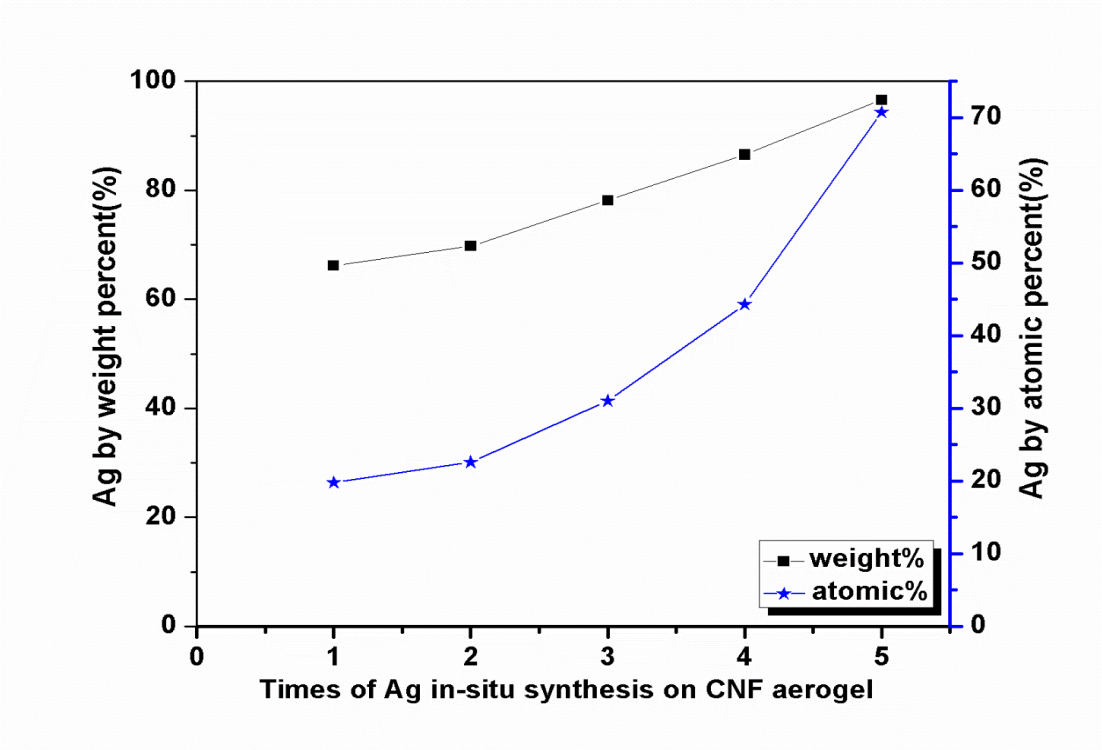

Figure 4.7 Change of Ag contents with synthesis times in term of weight percent and atomic percent measured by the EDS analysis.

The amount and distribution of Ag on MFC aerogel surface are further studied by EDS analysis in Figure 4.6 and Figure 4.7. In Figure 4.6a, strong Ag characteristic peaks are found in as-made Ag/MFC aerogel. The dispersion of Ag particles in MFC aerogel can be observed from the EDS mapping shown in Figure 4.6b. The Ag particles are well distributed in the whole MFC aerogel. In Figure 4.7, we can see how the contents of Ag change with the increase of Ag synthesis times. The in-situ reaction of Ag on aerogel was repeated for five times to achieve high conductance. The results indicate that Ag contents increase with the increase of Ag in-situ synthesis times in term of both weight percent and atomic percent. After five times reactions, the weight percent and atomic percent of Ag can achieve 96.6% and 70.7% respectively.

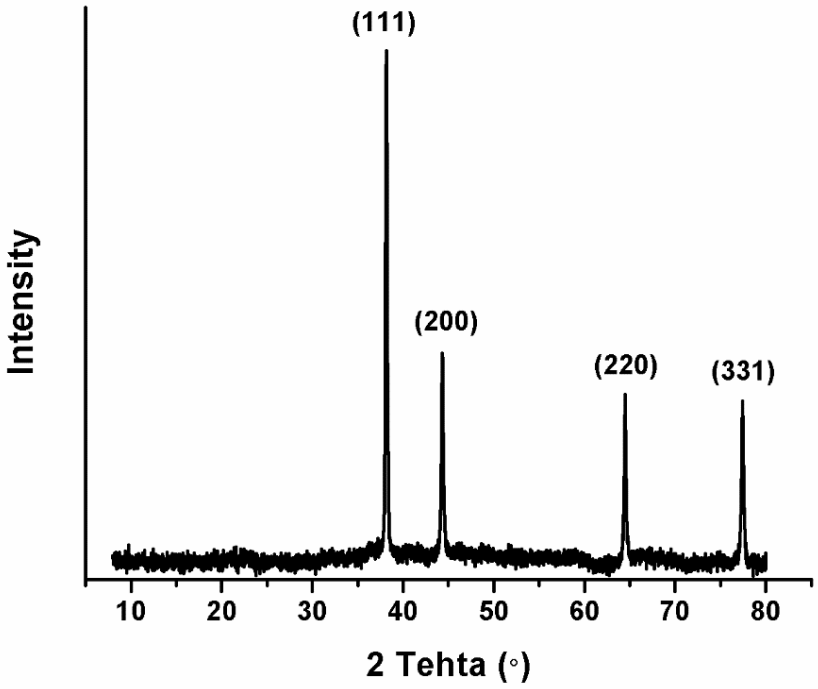

Figure 4.8 X-ray diffraction patterns of PANI/Ag/MFC aerogel

The XRD pattern of Ag/MFC aerogel is shown in Figure 4.8. The sharp peaks center at 2θ of 38º, 44º, 64 º, and 77° correspond to (111), (200), (220), and (311) silver planes, respectively, which coincides well with the literature values (JCPDS No. 04-0783)[188]. The XRD is also a proof of success of synthesis of Ag particles on the MFC skeleton.

4.3.4 Electrochemical properties of the PANI/Ag/MFC aerogel supercapacitors

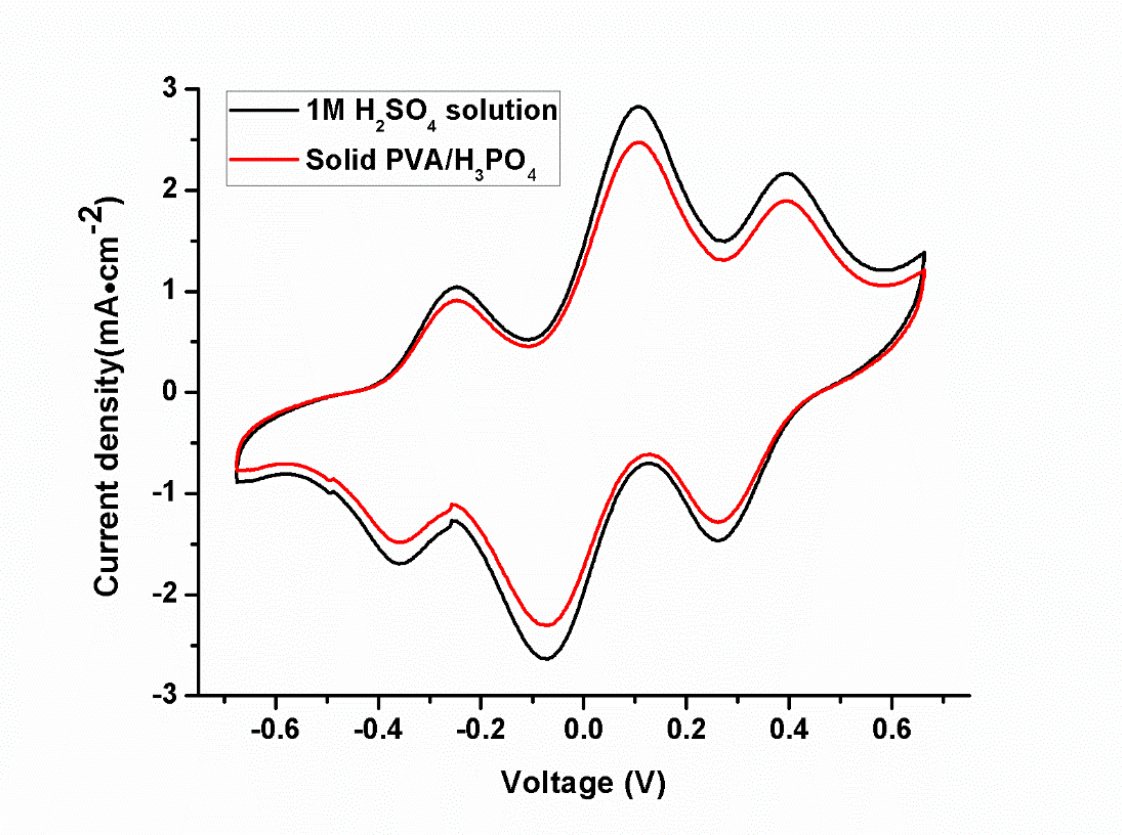

Figure 4.9 Cyclic voltammetry (CV) of PANI/Ag/MFC aerogel with 5 min PANI electrodeposition in 1M H_2SO_4 solution and PVA/H_3PO_4 solid electrolyte at a scan rate of 20mV/s

The electrical performances of PANI/Ag/MFC supercapacitors were measured using cyclic voltammetry (CV), galvanostatic charge and discharge curve and electric impedance spectroscopy (EIS). The comparisons of the as fabricated PANI/Ag/MFC supercapacitors in 1M H_2SO_4 solution and in PVA/H3PO4 solid electrolyte are shown in CV plots at a scan rate of 20mV/s in Figure 4.9. The two curves show the same patterns with slightly different peak heights. The nearly overlapped curves indicate the electrochemical properties of PANI/Ag/MFC supercapacitors in PVA/H_3PO_4 solid electrolyte are almost as good as they are in H_2SO_4 aqueous solution, which suggests the

fast ion transportation of PVA/H_3PO_4 solid electrolyte. PANI is responsible for the three reversible peaks in these curves, reflecting the conversion of PANI in different oxidation states, which are leucoemeraldine, emeraldine, nigraniline and pernigraniline. Ag particles help to enlarge the area of the curves enclosed in CV curves because it is reported that Ag particles could greatly increase the capacitance of PANI by improving the electrodes conductivity [186, 189, 190]. However, for the device contains only Ag/MFC aerogel (without PANI), the CV curve indicated that almost no measurable capacitance could be observed.

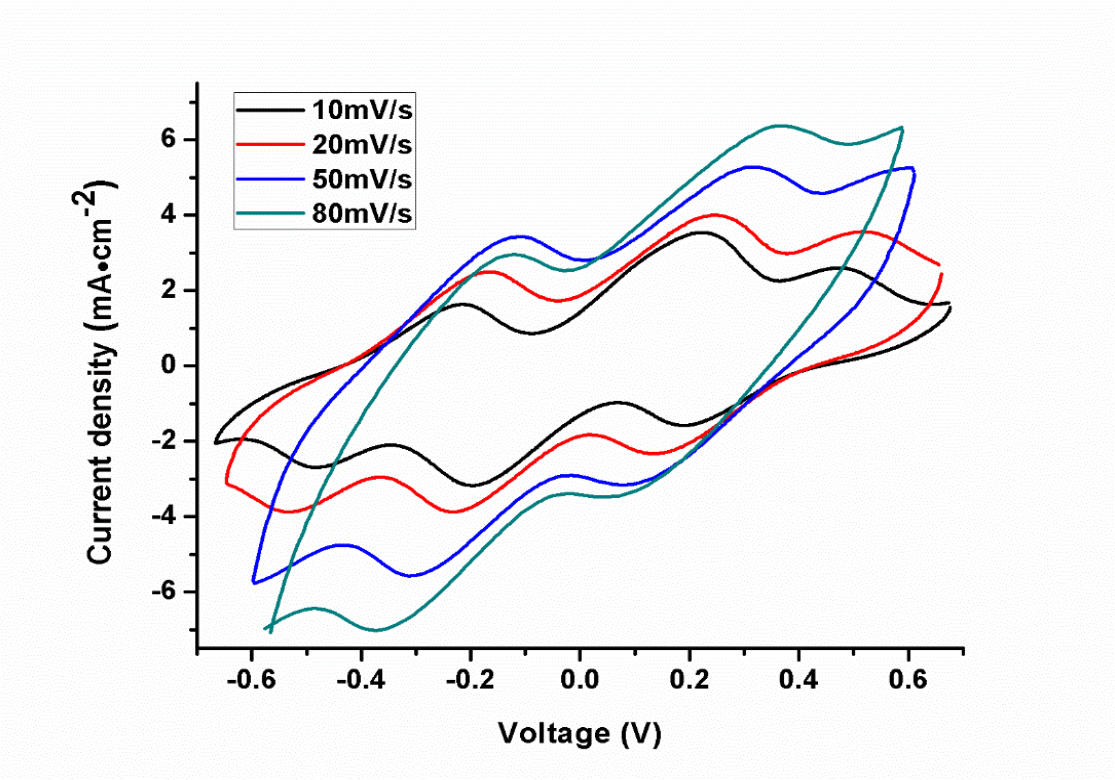

Figure 4.10 CV of PANI/Ag/MFC aerogel with 15 min PANI electrodeposition under different scan rates of 10mV/s, 20mV/s, 50mV/s and 80mV/s

PANI/Ag/MFC aerogel supercapacitor with 15 min PANI electrodeposition was tested under different scan rates of 10, 20, 50, 80 mV/s, as shown in Figure 4.10. It can be seen that the cathodic peak potentials shift to the positive direction and the anodic

peak potentials shift to the negative directions as the scan rates increase. All the peak currents increase with the increase of scan rate. The specific areal specific and mass capacitances of the PANI/Ag/MFC aerogel supercapacitors were calculated according to the equation $C_S = \frac{\int IdV}{s \times \Delta V \times r}$ and $C_m = \frac{\int IdV}{m \times \Delta V \times r}$ respectively, where I is the measured current, V is the applied potential, s is the area of one electrode sheet, m is the mass of electrode PANI on one electrode, ΔV is the range of voltage scan, and r is the scan rate.

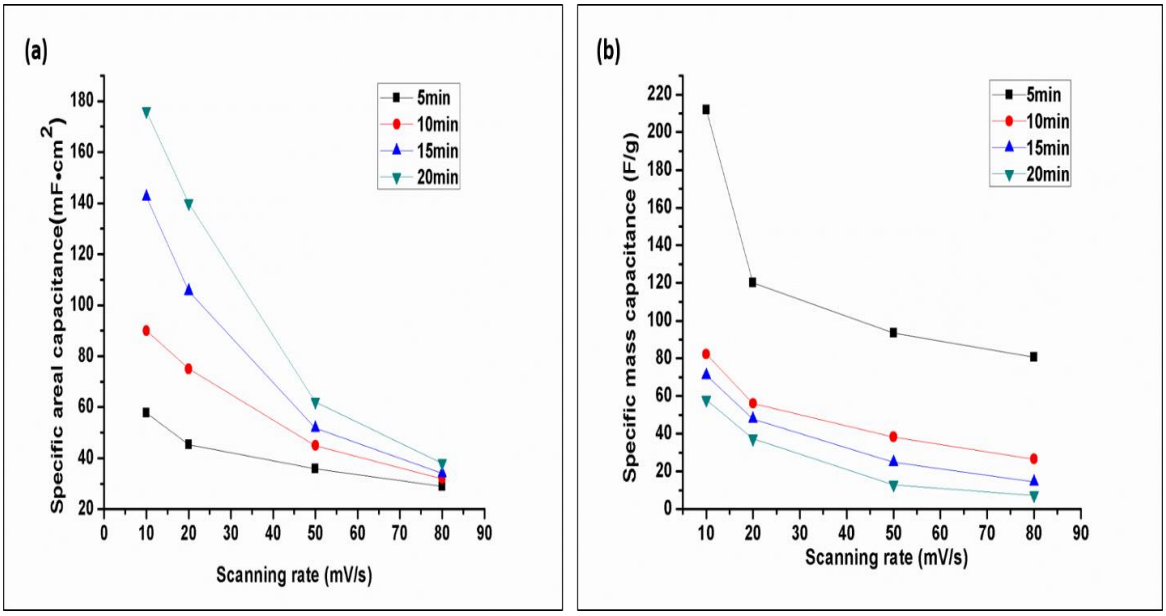

Figure 4.11 (a) Specific areal capacitance C_s vs scan rates for different PANI deposition time, ranging from 5 to 20 min. (b) Specific mass capacitance C_m vs scan rates for different PANI deposition time, ranging from 5 to 20 min

The specific areal capacitance of PANI/Ag/MFC aerogel supercapacitors with different PANI deposition time and different scan rates are given in Figure 4.11a. The C_s increases with the increase of electrodeposition time considering the increasing amounts of PANI for longer deposition time. Meanwhile the C_s also increases with the decrease of

scan rates due to more adequate Faradaic reactions at lower scan rates. The C_s for PANI/Ag/MFC aerogel supercapacitors with 20 min PANI electrodeposition is calculated to be 176 $mF \cdot cm^{-2}$ at the scan rate of 10mV/s, which is significant higher than most previously reported flexible supercapacitors (0.4 mF/cm^2-109 mF/cm^2)[118, 119, 121, 162-164] The C_m of PANI/Ag/MFC aerogel supercapacitors with different PANI deposition time and different scan rates is given in Figure 4.11b. The results in Figure 5.11b agree with the work reported by Chen et al. on carbon nanotubes/MnO_2 sponge supercapacitors.[176] The Cm depends strongly on the scan rate for low mass loading supercapaictors but depends weakly on scan rate for high mass loading supercapacitors. That is to say, for higher mass loading supercapacitors, such as 10, 15, 20 min PANI depositions, the Cm change with scan rates is small. However, for low mass loading supercapacitors, such as 5 min PANI depositions, relatively large changes in C_m with scan rate can be achieved. This is mainly due to the limited conductivity of high mass loading samples and the limited utilization of PANI at high scan rates.[176] The specific mass capacitance for 5 min electrodeposited PANI on Ag/MFC aerogel can reach be 212F/g at the scan rate of 10mV/s.

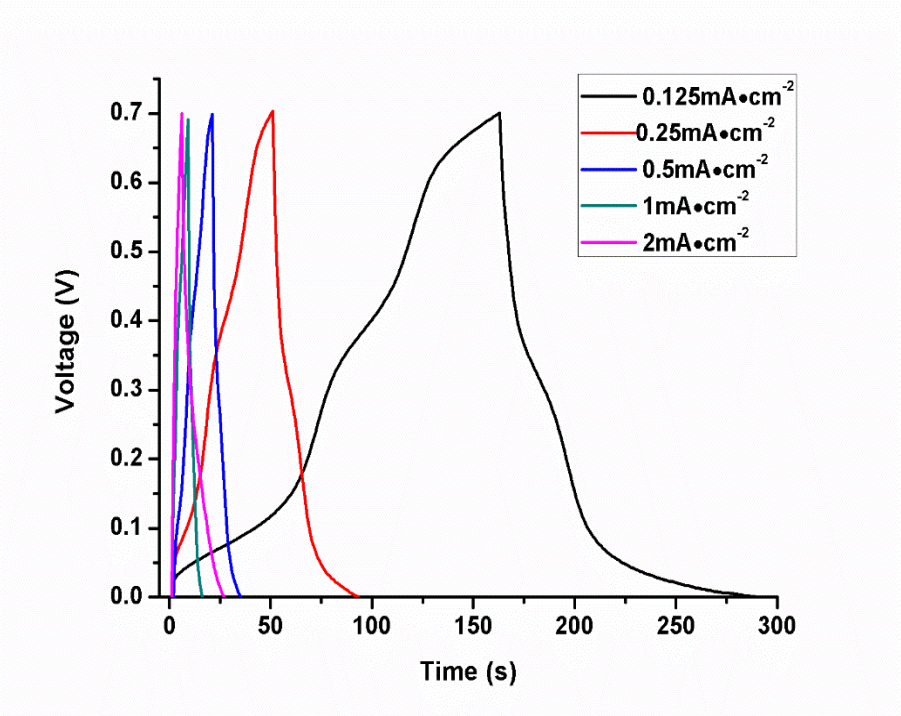

Figure 4.12 Galvanostatic charge-discharge curves at different current densities for PANI/Ag/MFC aerogel with 10 min PANI electrodeposition

The galvanostatic charge-discharge curves for PANI/Ag/MFC aerogel supercapacitors with 10min PANI electrodepostion at different current densities are illustrated in Figure 4.12. The specific capacitance can be calculated from the charge-discharge curves following the equation $C=\frac{2I}{S\times\left(\frac{dv}{dt}\right)}$, where I is the applied current, s is the area of one electrode, dV/dt is calculated from the slope obtained by fitting a straight line to the discharge curve over the range of Vmax to 1/5 V_{max}. The specific capacitance is calculated to be 42 $mF\cdot cm^{-2}$ for PANI/Ag/MFC aerogel with 10 min PANI deposition at 0.125 mA·cm-2, which is in good agreement with the value obtained from CV curve of 45 mF·cm-2 at scan rate of 20 mV/s. From the charge discharge curve, it can also be seen that the specific capacitance increases with decrease of the discharge current density. That reflects the ionic nature of the supercapacitors. With the lower charge-discharge

density of the supercapacitor, the ions have more time to get into position to react of PANI, which gives higher capacitance.

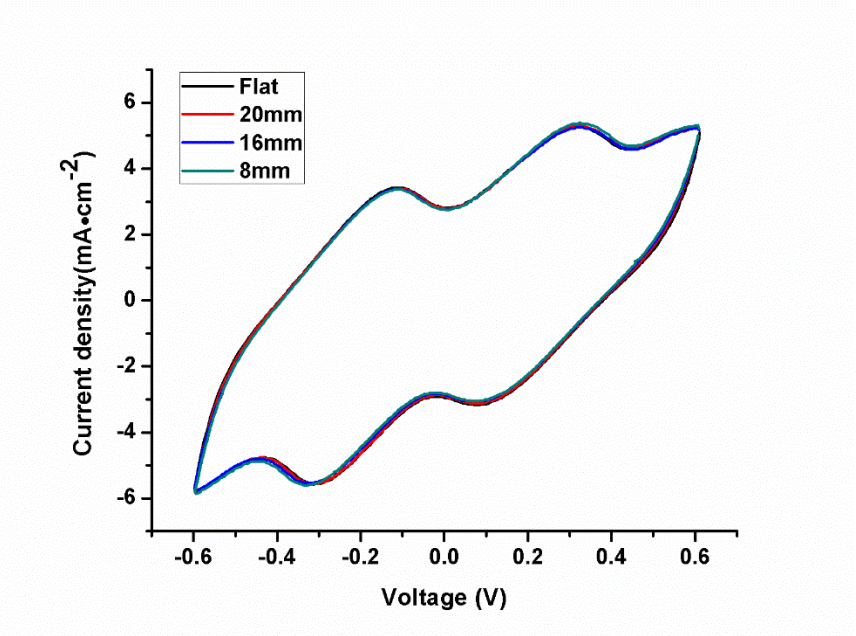

Figure 4.13 CV of PANI/Ag/MFC aerogel with 15 min PANI electrodeposition under different bending radius (the area of supercapacitors are 7mm*7mm)

In order to test the flexibility of the as fabricated supercapacitors, CV plots of PANI/Ag/MFC aerogel with 15 min PANI deposition under different bending radius are tested in Figure 4.13. The overlapped curves indicate the bending of the samples will not change their electrochemical behavior. The supercapacitors are quite flexible and can be readily bent without damage of the electrochemical properties.

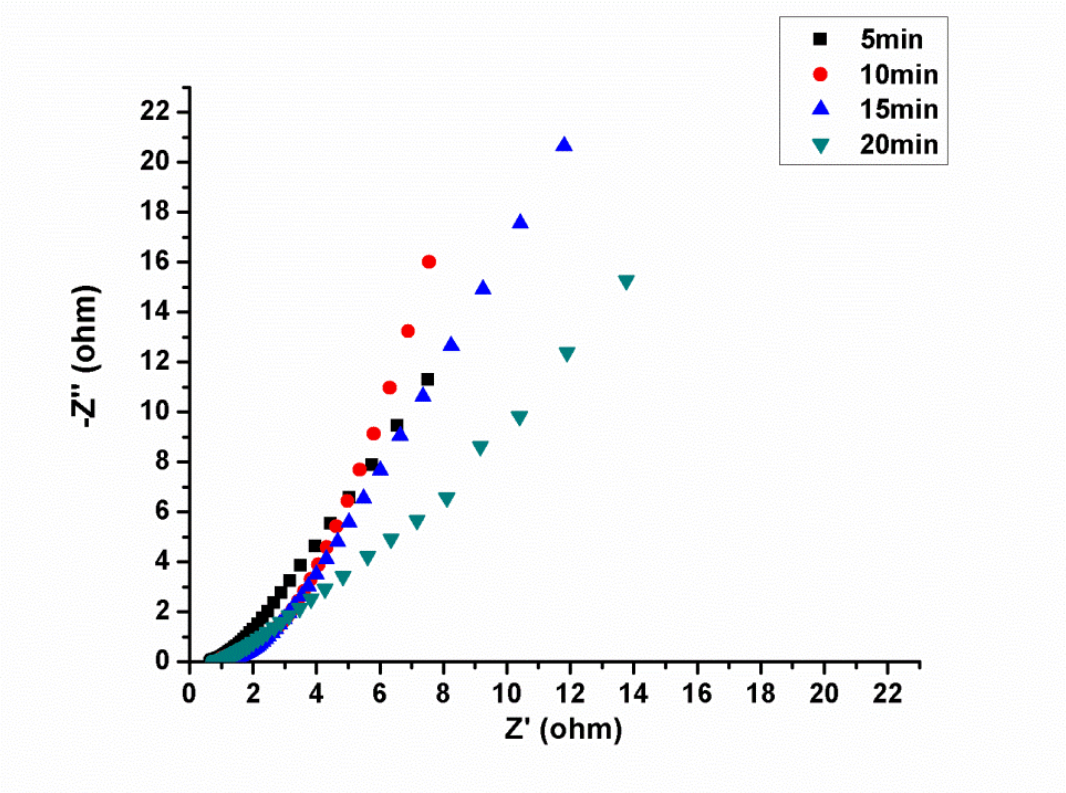

Figure 4.14 Nyquist plots of PANI/Ag/MFC aerogel supercapacitors with 5min, 10min, 15min, 20min PANI electrodeposition

The electrochemical impedance spectroscopy (EIS) was used to characterize PANI/Ag/MFC aerogel supercapacitors with different PANI deposition. The results are shown in Figure 4.14. EIS is a technique to provide more information on the electrochemical frequency behavior of the supercapacitors. It can be seen that the lower left portion of the curves refers to the high frequency region while the higher portion refers to the low frequency region. No distinct semi-circle in the curves indicates a very small charge transfer resistance at the PANI/Ag electrode/electrolyte interface. In addition, the linear portion in the low-frequency range is attributable to Warburg impedance, resulting from the frequency dependence of ion diffusion and transport in the electrolyte. There is an angle between the linear region of the plots and the real axis. The angles in Figure 4.14 generally follow the trend that with larger loading of PANI, the

angle will go smaller. The smaller angle indicates a greater variation in the ion diffusion path length and an increase of ion movement obstruction for ion diffusion into the electrode. Meanwhile, the value of the intercept at the real axis in the high frequency range is used to estimate the equivalent series resistance (ERS). All the samples show low ERS, which is around 1Ω. ERS includes electrode resistance, electrolyte resistance and contact resistance between the electrode and electrolyte. The low ERS of the samples help to guarantee the high value of power density.

4.4 Conclusions

In summary, in this chapter, PANI/Ag/MFC aerogel supercapacitors were successfully fabricated with high flexibility and excellent performances. The highly porous structure of aerogel and the high pseudocapacitive of polyaniline provide an excellent structure for supercapacitor electrodes, while the Ag particles provide fast electron transportion channels to achieve high capacitance. The specific capacitance of the as made supercapacitors can reach 176 $mF \cdot cm^{-2}$ at the scan rate of 10mV/s. Moreover, the capacitance of the supercapacitors shows almost no change after severe bending. The PANI/Ag/MFC aerogel supercapacitors are very promising for future development of energy storage devices.

Chapter 5

RATIONAL DESIGN OF HYBRID DYE-SENSITIZED SOLAR CELLS COMPOSED OF DOUBLE-LAYERED PHOTOANODES WITH ENHANCED POWER CONVERSION EFFICIENCY

Abstract

In this chapter, a uniquely-structured dye-sensitized solar cell was fabricated by assembling two photoanodes and one counter electrode in a single compartment. The two photoanodes have complementary roles in absorbing solar light at different wavelengths. The power conversion efficiency of the hybrid cell can reach to 6.6%, which is significantly higher than that of the single cell. The rational design of the hybrid cell does not need interconnecting layer as that is used in conventional tandem solar cells, leading to higher power conversion efficiency.

5.1 Introduction

Dye-sensitized solar cells (DSSCs) have been studied extensively because of their low cost compared to Si based solar cells[128]. Great effort has been made to improve their power conversion efficiency to sharpen their competitive edge over Si based solar cells [191-201]. Different methods have been adopted to realize better power conversion efficiency. One attempt is to develop a high-efficiency dye which can absorb as much light as possible in intensity and over a broader solar spectrum [202, 203]. However, it is difficult to achieve high photoelectric conversion and low charge recombination at the same time for high-efficiency dye design. Another method is to use simultaneous or

stepwise co-sensitization of multiple dyes for cell fabrication [204-207]. Co-sensitization compensates the disadvantages of absorption limitation of a single dye and broadens solar wavelength absorption range. However, in the simultaneously co-sensitized DSSCs[208, 209], there is an absorption competition between different dyes, and possible negative interaction between these dyes also occurs. As a result, the total light conversion is only slightly improved or even lowered than a single dye-sensitized DSSC. While in the case of stepwise co-sensitization on DSSCs[210-214], two or more different dye-sensitized semiconductor layers (usually TiO_2 or ZnO) will be coated stepwise on a conductive substrate. Clearly, with the increase of the semiconductor thickness, difficulties will be encountered for successful injection of electrons to the conductive substrate.

Tandem or hybrid solar cells are also used to harvest more solar energy [215, 216]. Generally, these cells were fabricated by vertically stacking two or more subcells connected by an interconnecting layer. Tandem/hybrid cells have the advantages of broadening the absorption spectrum and avoiding negative interaction among dyes. Nelles et al. designed tandem DSSCs with red dye and black dye in the upper and lower compartments, respectively[135]. However, in their design, the incident light needs to pass through multiple electrodes, including two working electrodes and one semitransparent counter electrode, to reach the lower dye. This would reduce the light absorption of the bottom cell. Murayama and Mori designed a face to face tandem cell structure with two dye-sensitized TiO_2 at each side as working electrodes and a platinum mesh in the middle as the counter electrodes [136]. Homogeneous DSSCs (N3 dye-sensitized TiO_2) and heterogeneous DSSCs (N3 dye and black dye-sensitized TiO_2) were tested in this design, with power conversion efficiency being 1.8% and 3.9%, respectively. Likewise, the middle counter electrode, or called interconnecting layer, would block the part of solar energy, leading to the low efficiency. Yamaguchi et al. fabricated tandem dye-sensitized solar cells on a glass rod, in which two different dye-sensitized TiO_2 layers were assembled along the glass rod[217]. These tandem cells

showed a low power conversion of 1.33%. The reason for the low efficiency was because that almost of the light passed through the glass rods directly without being absorbed. Only a small portion of the light contacting the interface between the glass rod and the TiO_2/dye layer was used for photoconversion.

Although tandem solar cells commonly have higher efficiency than a single solar cell, there are many challenges in order to further improve their performance. For example, to connect two or more subcells in a series, interconnecting layers have to be used. Ideally, the interconnecting layers should have sufficient conductivity, high transparency, good uniformity and high chemical stability. Their energy levels should also match with those of donor/acceptor molecules in the active layer. Unfortunately, such ideal interconnecting layers have not been reported. Besides, compared to solid polymer tandem solar cells, the liquid electrolyte based dye sensitized tandem solar cells are more difficult to be fabricated due to the leakage of the electrolyte.

Herein, uniquely-structured dye-sensitized solar cells that have double-layered photoanodes with two different dyes, but only one counter cathode, are fabricated. Different from traditional DSSCs, a second photoanode layer is inserted between traditional anode (with N719 sensitized TiO_2 nanoparticles) and platinum cathode in our novel design. This second photoanode layer is made by a porous and electrical conducting Ti/Ni mesh with a thin layer of dye-sensitized TiO_2 nanoparticles coated on it. The two photoanodes containing different dyes are assembled face-to-face and connected in a parallel mode as co-anodes. Since the second layer is supported by a porous Ti/Ni mesh, the electrolyte can easily diffuse through this layer to reach the cathode. Because of the two different dye-sensitized TiO_2 layers, such rationally designed hybrid solar cells can absorb more light over a broader wavelength.

5.2 Experiments

5.2.1 Materials

P-25 powders (Degussa); polyvinylpyrrolidone(Alfa Aesar); ITO glass(Hudson Surface Technology); nitric acid (BDH); ethanol(BDH); Ni mesh (MTI corporation); titanium tetrachloride(Pfaltz And Bauer Inc); deoxycholaic acid(Acros Organics); chloroplatinic acid(J.T. Baker); PTFE separator films(Y-carbon); Di-tetrabutylammonium cis-bis(isothiocyanato)bis(2,2'-bipyridyl-4,4'-dicarboxylato)ruthenium(II) (N719)(Solaronix); triisothiocyanato-(2,2':6',6"-terpyridyl-4,4',4"-tricarboxylato) ruthenium(II) tris(tetra-butylammonium)(N749).

5.2.2 Experimental procedures

Preparation of TiO_2 photoelectrodes: A suspension of 3g P-25 powders, 60ml ethanol, 0.1ml HNO_3(65%) was put into a rotary evaporator at 80 ˚C for 6h until the suspension becomes powdery (TiO_2/NO_3^-). A coating paste was prepared by mixing 0.3g TiO_2/NO_3^-, 0.12g polyvinylpyrrolidone in 1.5ml ethanol. ITO conductive glass and Ni mesh were served as the substrates for the photoanodes. Before use, Ti was coated onto both sides of Ni mesh with a deposition thickness of 500nm by DC Sputter (UniFilm Technology) at a rate of 50 nm/min. The ITO glass and Ti/Ni mesh were pretreated in 50mM $TiCl_4$ solution at 70 ˚C for half an hour. The as prepared TiO_2/NO_3^- paste was then cast onto ITO glasses (14μm) and Ti/Ni mesh (18μm, both sides), followed by calcination at 500 ˚C for 2h. The photoanodes were treated again in 50mM $TiCl_4$ solution at 70 ˚C for half an hour, followed by calcination at 500 ˚C for 30min. After cooling down, TiO_2 on ITO conductive glass was immersed into 0.5mM N719/ethanol solution at room temperature for 24h. TiO_2 on Ti/Ni mesh was immersed into 0.2mM N749 with 20mM deoxycholic acid (DCA) in ethanol at room temperature for 24h. The counter electrodes were prepared by spreading a 0.5mM H_2PtCl_6 ethanol solution to ITO conductive glass,

followed by calcination at 400 ˚C for 20min. The PTFE separator films were kindly provided by Y-Carbon Inc.

Fabrication of dye-sensitized solar cells: The single N719 cells were prepared by placing a Pt counter electrode against a TiO_2/ITO photoanode by using Kapton tapes as spacers. The single N749 cells were prepared by sequentially assembling ITO conductive glasses, N749 sensitized TiO_2 on Ti/Ni mesh, a PTFE separator and a Pt counter electrode, and sealed with Kapton tapes. Notably, the Ti/Ni mesh was only partially coated with N749 sensitized TiO_2, so that the uncoated part was connected to ITO glasses by indium metal. The hybrid cells were fabricated by sequentially assembling a N719-sensitized TiO_2 on ITO glasses, N749-sensitized TiO_2 on Ti/Ni mesh, a PTFE separator and a Pt counter electrode together, and sealed with Kapton tapes. The redox electrolyte used was an ionic liquid containing 0.60MBMIM-I, 0.03 M I_2, 0.50 M TBP, and 0.10 M GTC in a mixture of acetonitrile and valeronitrile (v/v = 85/15) (No. ES-0004, io.li.tec, Germany). The electrolyte was injected into the cell by a narrow passage left by the Kapton tapes.

Sample Characterizations: The photocurrent density-voltage (J-V) characteristics were measured using a Keithley model 2400 multisource meter. A solar simulator (SoLux Solar Simulator) was used to simulate sunlight for an illumination intensity of 100 mW/cm^2, calibrated with a Daystar Meter. The surface morphology of samples was examined on a LEO 1530 scanning electron microscopy with an acceleration voltage of 3kV. X-ray diffraction (XRD) analysis was performed on X'Pert PRO diffractometer (PANanalytical BV) with Cu K*a* radiation. Electrochemical impedance spectroscopy was scanned under open voltage by electrochemical workstation (Zahner, Zennium). UV-Vis absorption spectra were measured by a UV-Vis spectrophotometer (SHIMADZU, UV-2600). The IPCE spectra were measured by QE/IPCE measurement kit from Newport Company.

5.3 Results and discussion

5.3.1 Structure of the hybrid dye-sensitized solar cells with double-layered photoanodes

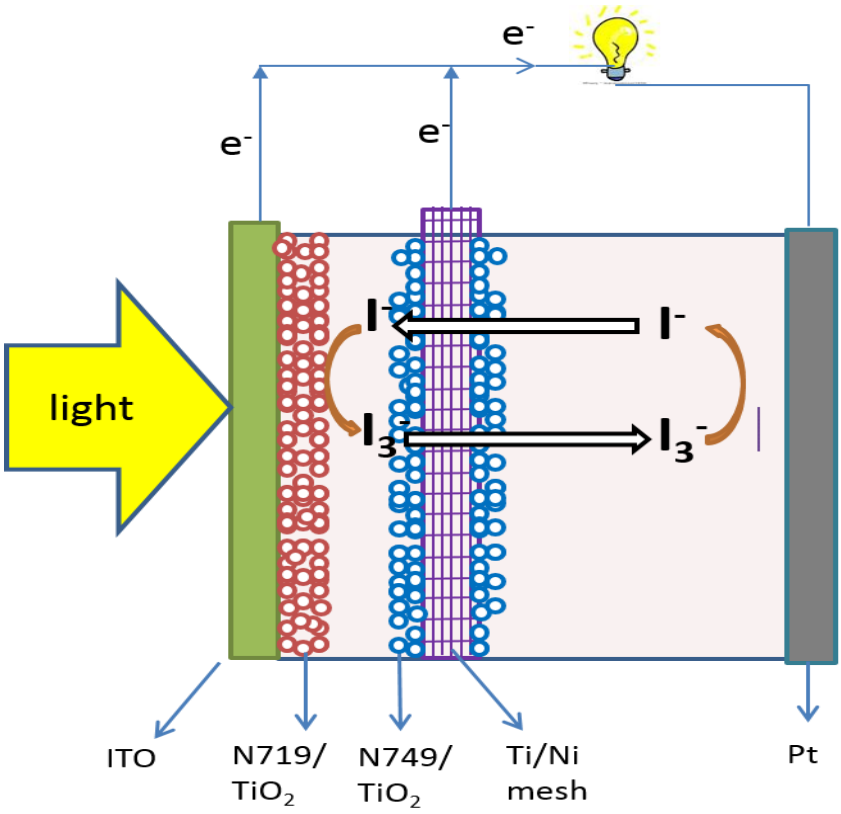

Figure 5.1 Schematic illustration of dye-sensitized solar cells with double-layered photoanodes

Figure 5.1 illustrates a schematic diagram of the structure of hybrid solar cells. The top photoanode is made of N719-sensitized TiO_2 on ITO glass. The second photoanode is composed of N749-sensitized TiO_2 on the substrate of porous Ti/Ni mesh (i.e., 500nm Ti was sputtered on Ni mesh). The whole cell compartment is filled with electrolyte solution. The two dyes, N719 and N749, compensate the light absorption range so the solar cell efficiency can be substantially improved. Upon incident light, the

electrons in the highest occupied molecular orbital (HOMO) of N719 and N749 are excited and injected to TiO_2 nanoparticles and then transport to the ITO and Ti/Ni mesh, respectively. The redox couple in the electrolyte will receive the electrons at the counter electrode and reduce the dye molecules back to their original states. The photo of the hybrid cell is shown in Figure 5.2.

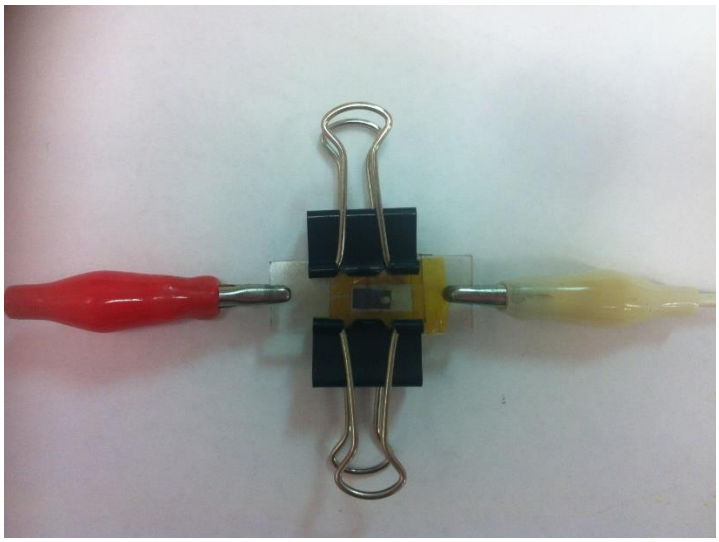

Figure 5.2 Photo of the hybrid cell device

Our double-layered DSSCs are different from conventional tandem solar cells. In our design, there is only one cathode but two parallel connected photoanodes coated with different dyes. The hybrid cells designed in this study allows the incident light to directly reach the second photoanode after passing through the first one, which can reduce the loss of solar energy and internal resistance. More importantly, no interconnecting electrode is needed, which overcomes the bottleneck in fabricating tandem cells. Furthermore, the single-compartment design renders the cells to be more compact and of lower internal resistant. For our hybrid DSSCs, two photoanodes can be separately prepared, thereby eliminating the issues encountered by co-sensitized solar cells.

5.3.2 Morphology of the photoanodes

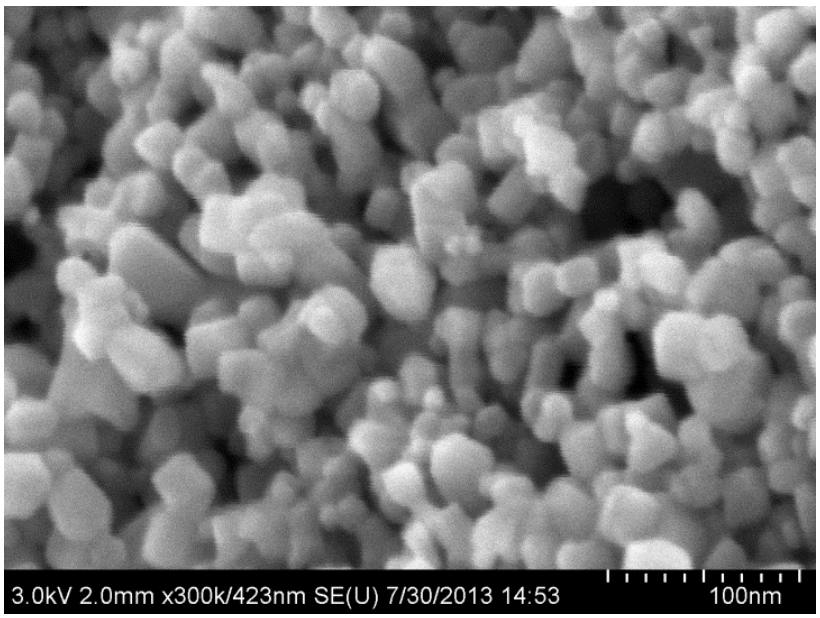

Figure 5.3 TiO_2/NO_3^- nanoparticles

Figure 5.3 shows the SEM image of the TiO_2 nanoparticles(NP). It can be seen that the diameters of TiO_2 NP are ranged from 20 to 40nm. Nano-sized pores can be seen among TiO_2 nanoparticles. These nano-sized pores can provide passways for the diffusion of electrolyte and the adsorption of dye molecules.

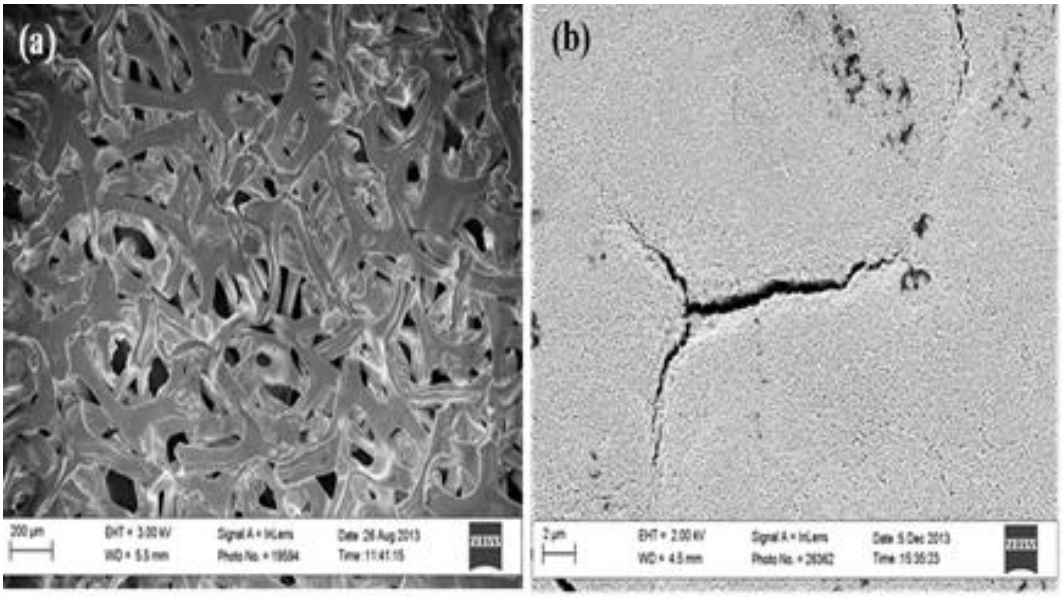

Figure 5.4 SEM images of (a) Ti/Ni mesh; (b) TiO_2 nanoparticles on Ti/Ni mesh

The SEM image of Ti/Ni mesh is shown in Figure 5.4a. Clearly, the Ti/Ni mesh is made up of interconnected holes with diameters in the range of 100-250µm. The porous nature of Ti/Ni mesh is an essential prerequisite for the electrolyte to penetrate through the whole space in the solar cell compartment. Figure 5.4b displays the morphology of TiO_2 nanoparticles thin film coated on Ti/Ni mesh. The TiO_2 NP thin film appears to have some cracks, which is beneficial for electrolyte to flow through.

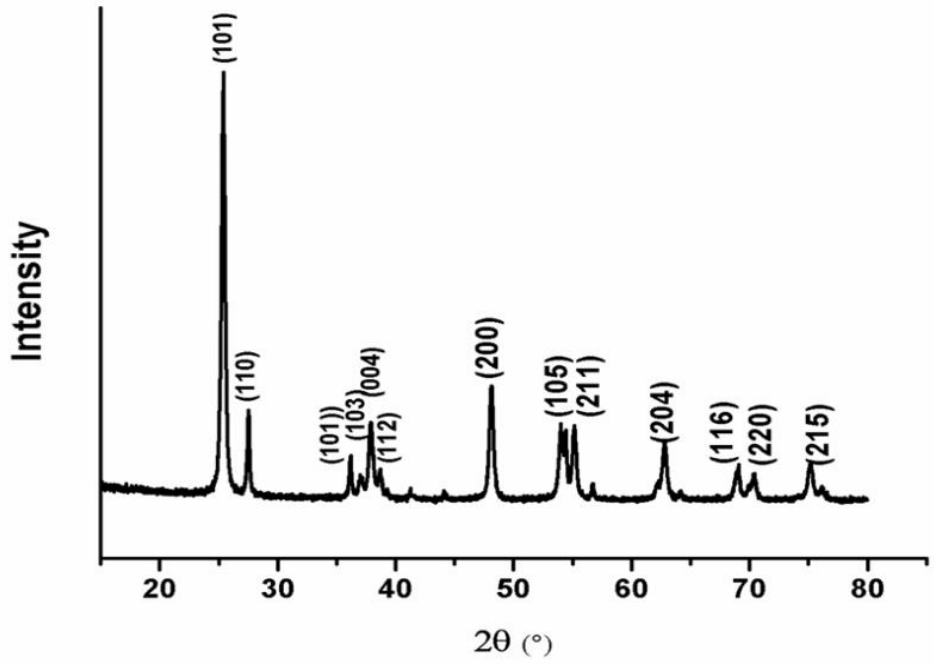

Figure 5.5 X-ray diffraction patterns of TiO_2 nanoparticles

Figure 5.5 shows the X-ray diffraction profile of the TiO_2 nanoparticles. Both anatase and rutile phase exist in the as-prepared TiO_2 nanoparticles. The strong diffraction peaks at 25˚ and 48˚, corresponding to face (101) and (200), respectively, are solid evidence of TiO_2 NP in its anatase phase. The strong peaks at 27˚, 36˚, 55˚, corresponding to face (110), (101), (211), respectively, indicate the existence of rutile phase of TiO_2 NP. All peaks are in good agreements with the standard spectrum of anatase and rutile TiO_2. (JCPDS no. 84-1286 and 88-1175).

5.3.3 Complementary absorption of solar energy for the two photoanodes

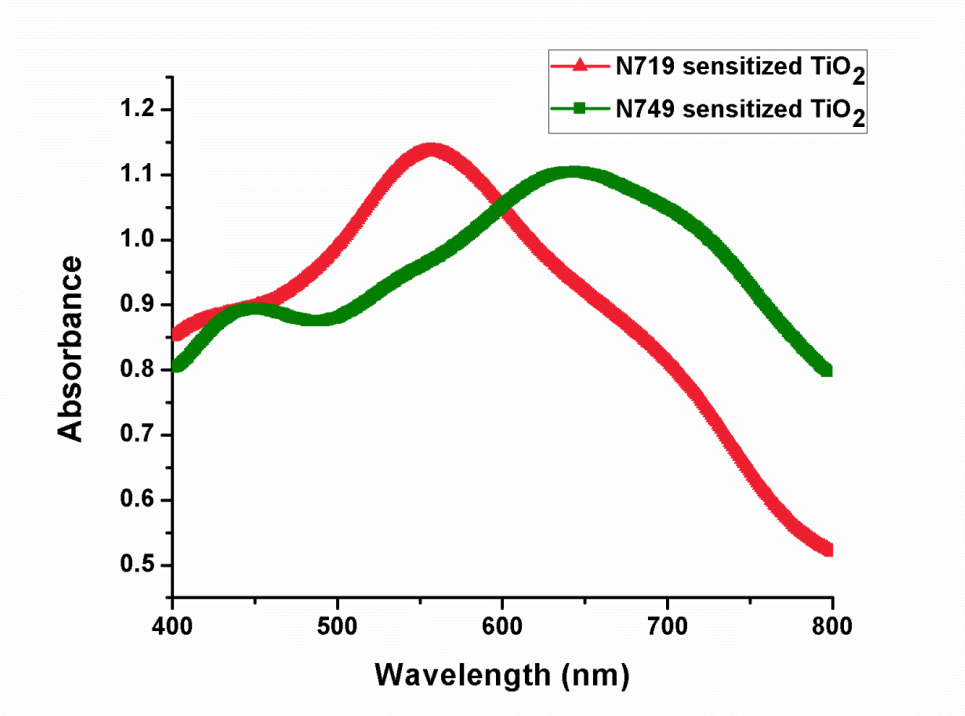

Figure 5.6 UV-Vis spectrum of N719/TiO_2 film and N749/TiO_2 film

To impart the hybrid cell with higher power conversion efficiency than an individual cell, the sensitizers on the two photoanodes should have complementary absorption spectrum for solar energy. Thus, the UV-Vis absorption spectra and IPCE spectra of N719 and N749 sensitized solar cells are measured, as shown in Figure 5.6 and 5.7. UV-Vis spectra in Figure 5.6 shows that N719 sensitized solar cells have a strong absorption band in the range of 500-800nm with maximum peak λ=556nm; N749 sensitized solar cells have two peaks in the range of 400-500nm and 600-800nm, with maximum peaks at λ=450nm and λ=647nm.

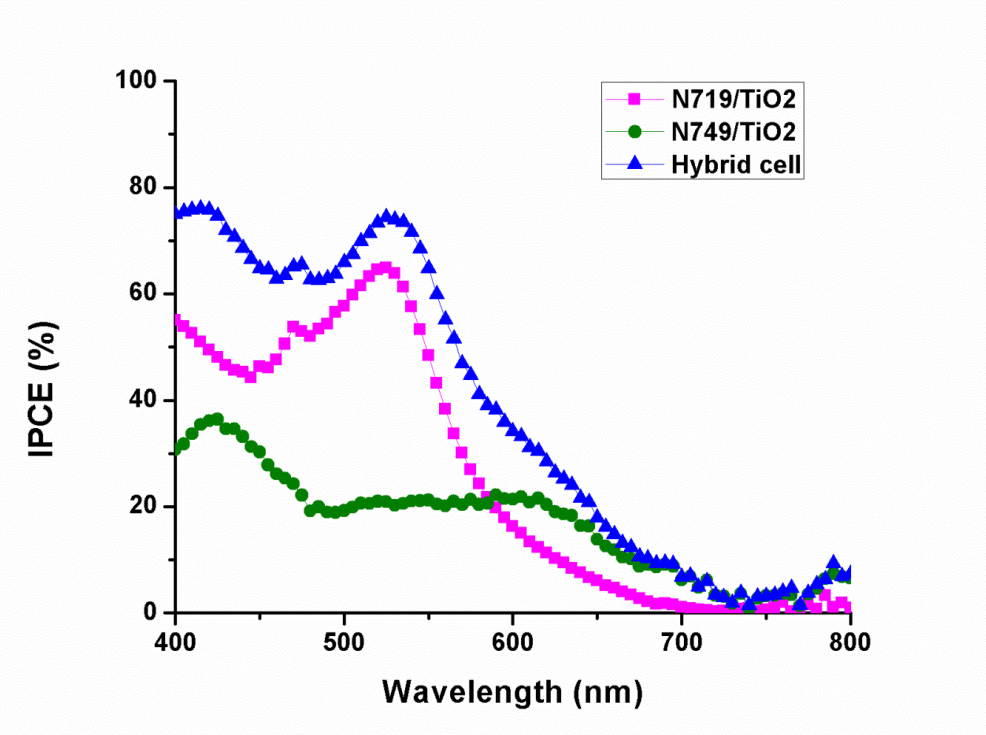

Figure 5.7 IPCE spectra of N719-sensitized TiO_2 cell, N749-sensitized TiO_2 cell and the hybrid cell

In Figure 5.7, the IPCE spectra of individual N719 and N749 show peaks in the similar positions as compared to UV-Vis spectra. Compared with the N749 IPCE spectra with N719 spectra, a stronger absorption was observed in the range of 600-800nm. The IPCE of the hybrid cell indicates better absorption across the broad spectral range. These results suggest that the N719 sensitized TiO_2 absorbs solar energy in the shorter wavelength region firstly, and then the longer wavelength light is further captured by the N749 sensitized TiO_2 in the second photoanode. The two dyes used in this study nearly cover the whole panchromatic spectrum in the range of visible light.

5.3.4 Photocurrent density-voltage (J-V) curves of the solar cells

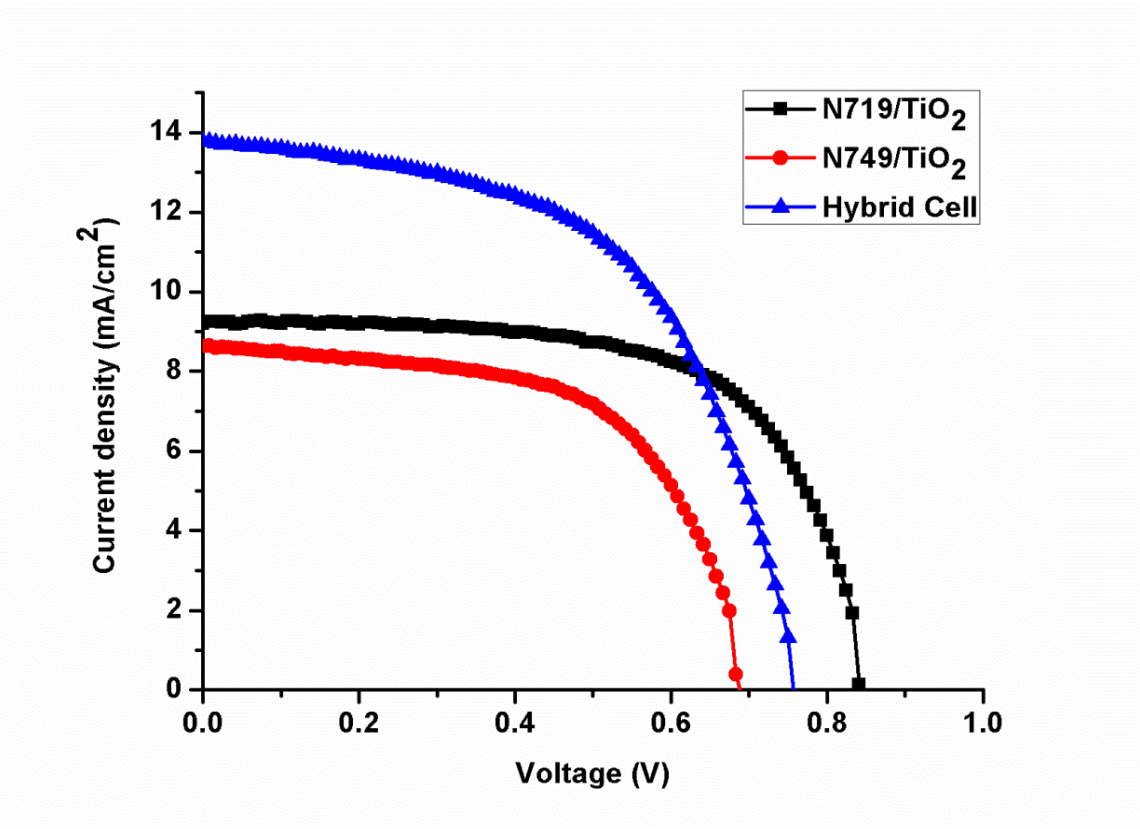

Figure 5.8 Photocurrent density-voltage (J-V) curves of individual N719-sensitized TiO_2 cell (black line), individual N749-sensitized TiO_2 cell (red line), and the hybrid cell (blue line)

The photocurrent density–voltage (J–V) characteristics of the individual N719 sensitized solar cell on ITO glass (N719 cell), individual N749 sensitized solar cell on Ti/Ni mesh (N749 cell) and the hybrid cell are compared in Figure 5.8. The important parameters, including open-circuit voltage V_{oc}, short-circuit current density J_{sc}, fill factor FF, and power conversion efficiency η are summarized in Table 5.1. The short-circuit current density (J_{sc}) at one sun illumination (standard illumination at AM1.5, or 1 kW/m^2) for the hybrid cell is 13.8 mA·cm^{-2}, which is much higher than either of the single cell, i.e. 9.2 mA·cm^{-2} for N719 cells and 8.84 mA·cm^{-2} for N749 cells. The significant increase

in J_{sc} reflects the parallel-connected nature of the hybrid cell and also substantiates the results of UV-VIS spectrum, suggesting that the hybrid cell can capture a nearly panchromatic spectrum of the sun light. It is interesting to see that the V_{oc} of the hybrid cell is close to the average of single cells V_{oc}. (i.e. $V_{oc\text{-}hydrid} \approx 1/2(V_{oc\text{-}cell1}+V_{oc\text{-}cell2})$). Lee et al.[133], Miao et al.[218] and Nelles et al.[135] carried out similar experiments on multi-layered TiO_2 with different dyes but by other methods. The relationship between V_{oc} of the whole cell and that of each single in their research agrees with the results in our experiments. The V_{oc} of a DSSC can be calculated by the following equation,

$$V_{oc} = \frac{RT}{\beta F}\ln\left(\frac{AI}{n_0 k_b [I_3^-] + n_0 k_r [D^+]}\right),$$

where R is the molar gas constant, T is the temperature, F is the Faraday constant, β is the reaction order for I_3^- and electrons, A is the electrode area, I is the incident photon flux, n_0 is the concentration of accessible electronic states in the conduction band, and k_b, k_r are the kinetic constants of the backreaction of the injected electrons with triiodide and the recombination of these electrons with oxidized dyes (D^+), respectively. Since the loss term as $n_0 k_r [D^+]$ can be neglected and $[I_3^-]$ can be considered as constant, V_{oc} depends logarithmically on $1/k_b$, ($k_b=\omega_{max}$[219], where ω_{max} refers to the peak frequency of the second arc). From the results of electrochemical impedance spectroscopy (EIS) shown in Figure 5.9, the peak frequency of for the hybrid cell (ω_{max}) is 7.15Hz, which is in the middle of those of single cells(i.e., ω_{max}=18.62Hz for N719 cell and ω_{max}= 4.98Hz for N749 cell). This explains why the V_{oc} for hybrid cells is in between of those of N719 cells and N749 cells. Besides using Ti/Ni mesh as the substrate for the second photoanode, stainless steel mesh (SSM) was also tested. However, the V_{oc} of SSM cell can only reach a value of 4.9V, with power conversion efficiency of 0.96%. The possible reason for the unsatisfactory performance of SSM cell is that the SSM can be oxidized into Fe oxides at high temperature (around 500˚C) during sintering [220-222], which greatly accelerates the back recombination of electrons at the TiO_2/dye/electrolyte

interface. Thus, we adopted Ti/Ni mesh as the substrate for the bottom cell in our hybrid cell.

Notably a fill factor of 0.56 is measured for the hybrid cell, which is lower than that of N719 cell and N749 cell. The lower FF of hybrid cell is probably due to the higher internal resistance compared to the single cell. The overall energy conversion efficiency for hybrid cell is 6.6%, which is 21% (compared to N719 cell) and 47% (compared to N749 cell) higher than that of the single cell. The significant improvement in the efficiency of hybrid cell proves that within the same dye-sensitized TiO_2 areas, the performance of the hybrid cell is much better than a single cell.

Table 5.1 . Photovoltaic parameters of the hybrid cell and the individual N719 and N749 cells.

	V_{oc} (V)	J_{sc} (mA·cm^{-2})	FF	η (%)
N719 cell	0.84	9.2	0.66	5.2
N749 cell	0.69	8.64	0.61	3.5
Hybrid cell	0.76	13.8	0.56	6.6

5.3.5 Electron kinetics of the solar cells

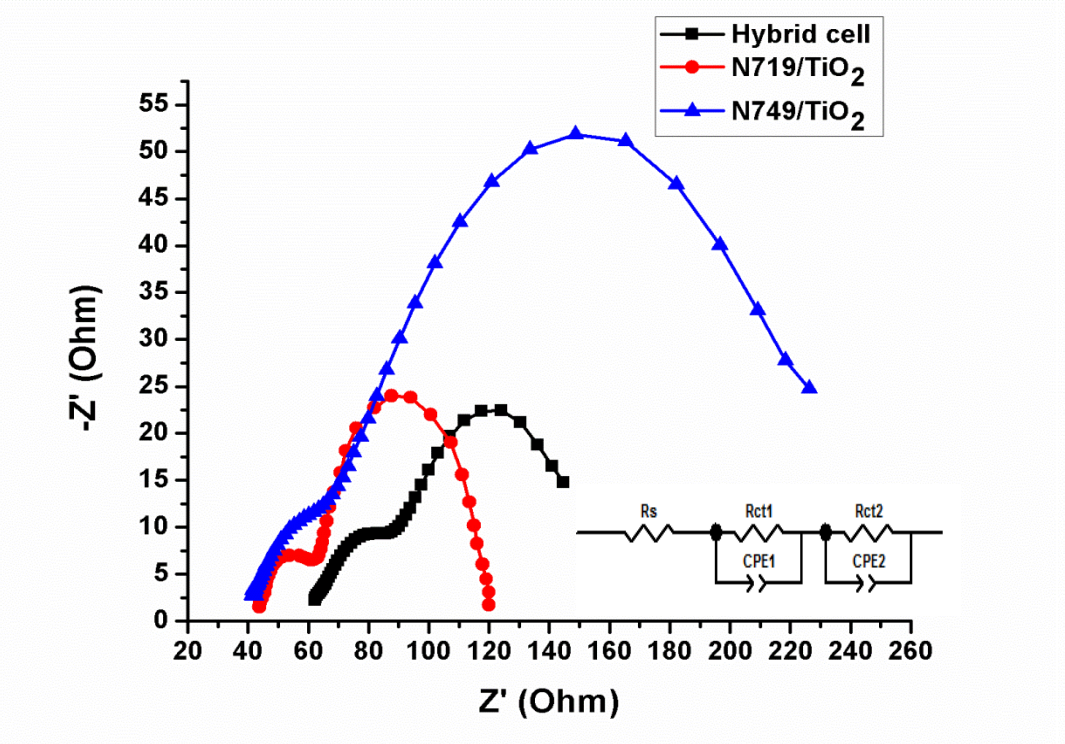

Figure 5.9 Electrochemical impedance spectroscopy of individual N719-sensitized TiO_2 cell (red line), individual N749-sensitized TiO_2 cell (blue line), and the hybrid cell (black line). The equivalent circuit is inserted in the bottom right of the figure.

To study the kinetics of electron transport and recombination, electrochemical impedance spectroscopy (EIS) and an equivalent circuit are studied in Figure 5.9. The key parameters obtained from EIS measurements are listed in Table 5.2. Each EIS curve consists of two arcs. The first arc assigned at high frequency scan region is related to the kinetics at the interface of Pt counter electrode/electrolyte. The diameter of the first arc is regarded as the resistance at the Pt surface (R_{ct1}), which is 20Ω (N719 cell), 22 Ω (N749 cell), and 24 Ω (hybrid cell), respectively in our experiments. The similar R_{ct1} for the three cells agrees with the fact that the Pt counter electrodes are prepared under the same condition. The second arc in the curve is assigned at low frequency region, indicating the kinetics at the interface of TiO_2/dye/electrolyte. The diameter of the second arc is related to charge-transfer resistance for electron recombination (R_{ct2}), which is 56 Ω (N719 cell),

120 Ω (N749 cell), and 62 Ω (hybrid cell), respectively. Obviously, the charge combination resistance of the hybrid cell is in between the two individual cells. This is not surprising as the hybrid cells combine the characteristics of individual N719 cell and N749 cells. Consequently the properties will be compromised. For the same principle, the effective recombination rate constant (k_b) and effective electron lifetime (τ_b) of the hybrid cells also locate in between of the single cells. R_s represent the serious resistance of the circuit. It is reasonable to see that the series resistance of the hybrid cell is higher than either of the single cell.

Table 5.2 Parameters determined by the electrochemical impedance spectroscopy measurement.

	k_b (s^{-1})	τ_b (s)	$R_{s(\Omega)}$	$R_{ct1\ (\Omega)}$	$R_{ct2\ (\Omega)}$
N719 cell	18.62	0.054	41	20	56
N749 cell	4.98	0.200	52	24	120
Hybrid cell	7.15	0.140	62	22	62

k_b : effective rate constant for recombination reaction.

τ_b: effective electron lifetime for recombination.

R_s: series resistance

R_{ct1}: resistance at the Pt surface

R_{ct2}: charge transfer resistance related to the recombination of electrons

5.4 Conclusions

In conclusion, uniquely-structured dye-sensitized solar cells have been rationally designed and implemented by assembling two photoanodes (i.e., ITO/TiO_2 and Ti/Ni mesh/TiO_2) and one Pt/ITO counter electrode in a single compartment. The power

conversion efficiency of the hybrid cell (6.6%) is significantly higher than that of single cell. The higher J_{sc} of the hybrid cell substantiates the signature of the parallel cell connection. The porous structure of the second photoanode enables the crafting of hybrid cell in a single compartment, by allowing the electrolyte to diffuse through the whole cell space. In sharp contrast to other hybrid/tandem cells which need the interconnecting layers, the two photoanodes were designed to be right next to each other, thereby eliminating the unnecessary loss of solar energy. As such, our study demonstrates an easy and scalable method to fabricate hybrid dye-sensitized solar cells with improved power conversion efficiency.

Chapter 6

CONCLUSIONS AND RECOMMENATIONS

6.1 Overall Conclusions

In this thesis, the utilization and potential utilization of MFC in electronic devices by chemical modification and physical blending was explored. With people's attention on building a more sustainable and environmental-friendly world, bio-renewable materials, such as cellulose, found their roles in much broader applications than decades before. The extraordinary physical properties of cellulose, such as flexibility, high mechanical strength, and adjustable pore size rendered it great advantages compared to other metallic, ceramic and plastic materials. In this thesis, several types of paper-based electronics were successfully fabricated, including ionic diodes, electrical double layer supercapacitors, pseudocapacitors. In addition, hybrid two-photoanode dye-sensitized solar cells were studied in order to pave the way to fabricate novel paper-based dye-sensitized solar cells.

Transparent and flexible paper-based ionic diodes, which allowed unidirectional transportation of ions, were successfully fabricated by combing two layers of oppositely charged MFC. It was proved that the structure of two oppositely charged MFC was crucial for the rectification of the diodes, because the combination of them allowed electrostatic force to control the ions to flow selectively. The rectification ratio could reach to ca. 15 under ±5V. The ionic diodes were also examined under different

conditions. It was found that moisture content, scanning frequency, thickness and charge density were important factors to influence the performances of ionic diodes. All of these factors were closely related to the ionic nature of the diodes. It was also indicated that the diodes were quite flexible and transparent. The devices could be bent freely to form different curvature without breaking and people could easily see through the devices to detect patterns underneath. The ionic diodes also had excellent mechanical properties with tensile strength around 1Mpa, which was much better than other liquid-based ionic diodes.

Functional papers by doping carbon nanotubes and solid electrolyte (LiCl and PEO) in to MFC fibers for the applications of supercapacitors were made. The properties of the supercapacitors, especially with the focus on the electrochemical properties, were investigated. The areal capacitance of the supercapacitors was found to be closely related to the thickness of the electrode sheets. By increasing of thickness of the electrode sheets, more MWCNTs could be employed in per unit area, which led to more energy storage efficiency in terms of per unit area. However, this would come with a price of reducing the specific mass capacitance, since the resistance of the devices would increase with the increase of thickness. The results indicated that the areal specific capacitance of the paper-based supercapacitors could reach up to 154.5mF/cm^2 at 20mV/s from cyclic voltammetry. Meanwhile, due to the use of MFC as supporting substrates, the devices were quite flexible. Moreover, the capacitance remained almost the same when the supercapacitors were bent under different curvature.

PANI/Ag/MFC aerogel supercapacitors were also made with high flexibility and excellent performances. Compared to regular cellulose paper, the MFC aerogel appeared to have more specific surface area, which was beneficial to enlarge the contacting area between electrode materials and the electrolyte for more charge storage. It was shown that the CV plots of the solid-state PANI/Ag/MFC aerogel supercapacitors almost overlapped with those tested in liquid electrolyte system, indicating the good ionic

transportation for solid electrolyte. The specific capacitance of PANI/Ag/MFC supercapacitors could reach 176 $mF \cdot cm^{-2}$ at the scan rate of 10mV/s. In addition, the devices showed good flexibility with almost no change of capacitance under severe bending.

As pioneering work of exploring the potential of the porous MFC to be used in the dye-sensitized solar cells, doube-photoanode dye-sensitized solar cells were studied, with the key structure of porous Ni/Ti mesh as the supporting substrate for the second photoanode. The Ni/Ti mesh was playing a significant role, since it allowed the hybrid cell to be made in a single compartment by letting the electrolyte to penetrate through, and it also helped to reduce the loss of solar energy by avoiding the use of the interconnecting layers. The results showed that the power conversion efficiency of the hybrid cell (6.6%) was significantly higher than that of single cell. Since MFC can be rationally treated to resemble of the structure of Ni/Ti mesh, the work of the hybrid solar cells based on Ni/Ti mesh paved the way to the MFC-based dye-sensitized solar cells.

Overall, MFC was proved to be a good substrate/functional material to fabricate electronic devices. Its excellent physical properties and adjustable chemical properties rendered it broad applications for different electronics. Although some challenges are still need to overcome, such as the improvement of the conductivity for paper-based electronics, the work done in this thesis shed light on great potential for cellulose to be used in the next generation of green and flexible electronic devices.

6.2 Recommendations for future work

6.2.1 Control the moisture content in the paper-based ionic diodes

In this thesis, ionic diodes were successfully made by using small ions to conduct the current in a preferential direction. The performance of the ionic diodes was greatly influenced by the moisture content, scanning frequency, device thickness and charge

density. The moisture content directly determined how much hydrogens and hydroxides can be yielded to carry the charges and the resistance of the device. However, as the diodes underwent the voltage scan, electrode reactions would happen at both electrodes to consume the moisture of the device. Therefore, in order to achieve a stable performance of the device, moisture level needs to be controlled in a more accurate way. Instead of running the diodes in an open environment, a sealing device should be explored with the function of adding moisture into the device periodically.

6.2.2 Increase of conductivity of MWCNTs/MFC based supercapacitors

Paper-based supercapacitors were fabricated by physically doping modified MWCNTs and solid electrolyte into MFC. Due to the insulating nature of MFC, conducting materials such as MWCNTs were served both as conducting agents and electrode materials. Currently, the conductivity of the electrode sheets still need to be improved. The electrical resistance of the supercapacitors would greatly affect the electrochemical performances of the device and were important parameters to determine the power density of the devices. Another high conductive material should be designed to be either doped or synthesized in the electrode sheets, aiming to increase the electron transportation of the electrode sheets.

6.2.3 Balance the specific surface area and the pore size in the PANI/Ag/MFC aerogel supercapacitors

Compared to the MWCNTs/MFC based supercapacitors, the PANI/Ag/MFC aerogel supercapcaitors were made upon MFC aerogels, which had larger specific surface area than normal papers. The specific surface area is a very important parameter for supercapacitors, since it determines the contacting area between electrodes and electrolyte and thus affects the capacitance. In a certain range, the larger the specific surface area, the higher the capacitance would be. However, when the specific surface area increases to reach to a certain level, the pore size of the electrodes will be too small

for the ions to pass through. Thus, further study is needed to determine what will be the optimized value for the specific surface area, in order to achieve a balance of large contact area and the appropriate pore size.

6.2.4 Develop MFC-based dye-sensitized solar cells

Hybrid double-photoanode dye-sensitized solar cells were achieved with a higher power conversion efficiency than any of the single cell, with the critical structure being the porous Ni/Ti mesh as the second photoanode. The next step will be to modify MFC in order to get the similar porous network as the Ni/Ti mesh. There would be two ways to do that. One way is to coat conducting materials onto MFC surface; the other way is to use MFC as precursor, and then obtain carbon aerogels by high temperature calcination. It has been reported that high conductive carbon aerogel can be made by calcination of MFC aerogel at around 1000°C under nitrogen flow. The thus-made carbon aerogel would be further used in the dye-sensitized solar cells.

REFERENCES

[1] R. Agarwal, M.S. Alam, B. Gupta, Journal of Applied Polymer Science, 129 (2013) 3728-3736.

[2] R.M. Narbaitz, D. Rana, H.T. Dang, J. Morrissette, T. Matsuura, S.Y. Jasim, S. Tabe, P. Yang, Chemical Engineering Journal, 225 (2013) 848-856.

[3] J.M. Guo, X.Y. Li, C.D. Mu, H.G. Zhang, P. Qin, D.F. Li, Food Hydrocolloids, 33 (2013) 273-279.

[4] C.G. Hoyos, E. Cristia, A. Vazquez, Materials & Design, 51 (2013) 810-818.

[5] J.H. Wu, M.C. Kuo, C.W. Chen, C.W. Chen, P.H. Kuan, Y.J. Wang, S.Y. Jhang, Journal of Applied Polymer Science, 129 (2013) 3007-3018.

[6] D. Klemm, B. Heublein, H.P. Fink, A. Bohn, Angewandte Chemie-International Edition, 44 (2005) 3358-3393.

[7] D.L. Vanderhart, R.H. Atalla, Macromolecules, 17 (1984) 1465-1472.

[8] I. Sakurada, Y. Nukushina, T. Ito, Journal of Polymer Science, 57 (1962) 651-&.

[9] S. Iwamoto, W.H. Kai, A. Isogai, T. Iwata, Biomacromolecules, 10 (2009) 2571-2576.

[10] I. Siro, D. Plackett, Cellulose, 17 (2010) 459-494.

[11] Y. Habibi, L.A. Lucia, O.J. Rojas, Chemical Reviews, 110 (2010) 3479-3500.

[12] D. Roy, M. Semsarilar, J.T. Guthrie, S. Perrier, Chemical Society Reviews, 38 (2009) 2046-2064.

[13] R.H. Atalla, D.L. Vanderhart, Science, 223 (1984) 283-285.

[14] O. Nechyporchuk, M.N. Belgacem, F. Pignon, Carbohydrate Polymers, 112 (2014) 432-439.

[15] C.X. Huang, M.M. Yan, J. Wang, X.Y. Shen, L. Wang, Y. Chen, Asian Journal of Chemistry, 24 (2012) 5613-5618.

[16] K.L. Spence, R.A. Venditti, O.J. Rojas, Y. Habibi, J.J. Pawlak, Cellulose, 18 (2011) 1097-1111.

[17] J. Lu, P. Askeland, L.T. Drzal, Polymer, 49 (2008) 1285-1296.

[18] A.N. Nakagaito, H. Yano, Applied Physics a-Materials Science & Processing, 80 (2005) 155-159.

[19] T. Saito, S. Kimura, Y. Nishiyama, A. Isogai, Biomacromolecules, 8 (2007) 2485-2491.

[20] K.L. Spence, R.A. Venditti, Y. Habibi, O.J. Rojas, J.J. Pawlak, Bioresource Technology, 101 (2010) 5961-5968.

[21] T. Taipale, M. Osterberg, A. Nykanen, J. Ruokolainen, J. Laine, Cellulose, 17 (2010) 1005-1020.

[22] S. Ahola, M. Osterberg, J. Laine, Abstracts of Papers of the American Chemical Society, 233 (2007) 729-729.

[23] M. Andresen, P. Stenstad, T. Moretro, S. Langsrud, K. Syverud, L.S. Johansson, P. Stenius, Biomacromolecules, 8 (2007) 2149-2155.

[24] H. Lonnberg, L. Fogelstrom, M. Berglund, E. Malmstrom, A. Hult, European Polymer Journal, 44 (2008) 2991-2997.

[25] M. Henriksson, L.A. Berglund, P. Isaksson, T. Lindstrom, T. Nishino, Biomacromolecules, 9 (2008) 1579-1585.

[26] P. Stenstad, M. Andresen, B.S. Tanem, P. Stenius, Cellulose, 15 (2008) 35-45.

[27] O. Eriksen, K. Syverud, O. Gregersen, Nordic Pulp & Paper Research Journal, 23 (2008) 299-304.

[28] N. Lavoine, I. Desloges, A. Dufresne, J. Bras, Carbohydrate Polymers, 90 (2012) 735-764.

[29] N.C.T. Martins, C.S.R. Freire, R.J.B. Pinto, S.C.M. Fernandes, C.P. Neto, A.J.D. Silvestre, J. Causio, G. Baldi, P. Sadocco, T. Trindade, Cellulose, 19 (2012) 1425-1436.

[30] A. Wang, J. Zhao, M.A. Green, Applied Physics Letters, 57 (1990) 602-604.

[31] J.H. Zhao, A.H. Wang, M.A. Green, Progress in Photovoltaics, 7 (1999) 471-474.

[32] R. Labes, H. Zain, Naunyn-Schmiedebergs Archiv Fur Experimentelle Pathologie Und Pharmakologie, 126 (1927) 284-306.

[33] H. Reiss, Journal of Chemical Physics, 21 (1953) 1209-1217.

[34] B. Lovrecek, A. Despic, J.O.M. Bockris, Journal of Physical Chemistry, 63 (1959) 750-751.

[35] M. Seno, T. Yamabe, Bulletin of the Chemical Society of Japan, 37 (1964) 668-671.

[36] P. Lauger, Berichte Der Bunsen-Gesellschaft Fur Physikalische Chemie, 68 (1964) 534-541.

[37] O.J. Cayre, S.T. Chang, O.D. Velev, Journal of the American Chemical Society, 129 (2007) 10801-10806.

[38] H. Daiguji, Y. Oka, K. Shirono, Nano Letters, 5 (2005) 2274-2280.

[39] R. Karnik, C. Duan, K. Castelino, R. Fan, P.D. Yang, A. Majumdar, Asme, TRANSPORT OF IONS AND MOLECULES IN NANOFLUIDIC DEVICES, 2008.

[40] M.E. Gracheva, J. Vidal, J.P. Leburton, Nano Letters, 7 (2007) 1717-1722.

[41] I. Vlassiouk, Z.S. Siwy, Nano Letters, 7 (2007) 552-556.

[42] I. Vlassiouk, S. Smirnov, Z. Siwy, Nano Letters, 8 (2008) 1978-1985.

[43] Z. Siwy, E. Heins, C.C. Harrell, P. Kohli, C.R. Martin, Journal of the American Chemical Society, 126 (2004) 10850-10851.

[44] Y. Yan, L. Wang, J.M. Xue, H.C. Chang, Journal of Chemical Physics, 138 (2013).

[45] M. Ali, P. Ramirez, S. Mafe, R. Neumann, W. Ensinger, Acs Nano, 3 (2009) 603-608.

[46] C. Wei, A.J. Bard, S.W. Feldberg, Analytical Chemistry, 69 (1997) 4627-4633.

[47] S. Umehara, N. Pourmand, C.D. Webb, R.W. Davis, K. Yasuda, M. Karhanek, Nano Letters, 6 (2006) 2486-2492.

[48] E.C. Yusko, R. An, M. Mayer, Acs Nano, 4 (2010) 477-487.

[49] I.C. Bassignana, H. Reiss, Journal of Membrane Science, 15 (1983) 27-41.

[50] P. Ramirez, H.J. Rapp, S. Reichle, H. Strathmann, S. Mafe, Journal of Applied Physics, 72 (1992) 259-264.

[51] K. Nagasubramanian, F.P. Chlanda, K.J. Liu, Journal of Membrane Science, 2 (1977) 109-124.

[52] D.T. Conroy, R.V. Craster, O.K. Matar, L.J. Cheng, H.C. Chang, Physical Review E, 86 (2012).

[53] J.H. Han, K.B. Kim, H.C. Kim, T.D. Chung, Angewandte Chemie-International Edition, 48 (2009) 3830-3833.

[54] X. Li, B.Q. Wei, Nano Energy, 2 (2013) 159-173.

[55] J.R. Miller, P. Simon, Science, 321 (2008) 651-652.

[56] E. Frackowiak, F. Beguin, Carbon, 39 (2001) 937-950.

[57] R. Kotz, M. Carlen, Electrochimica Acta, 45 (2000) 2483-2498.

[58] Z.Y. Lin, Y. Liu, Y.G. Yao, O.J. Hildreth, Z. Li, K. Moon, C.P. Wong, Journal of Physical Chemistry C, 115 (2011) 7120-7125.

[59] A. Ghosh, Y.H. Lee, Chemsuschem, 5 (2012) 480-499.

[60] V.V.N. Obreja, Physica E-Low-Dimensional Systems & Nanostructures, 40 (2008) 2596-2605.

[61] Y.P. Zhai, Y.Q. Dou, D.Y. Zhao, P.F. Fulvio, R.T. Mayes, S. Dai, Advanced Materials, 23 (2011) 4828-4850.

[62] J. Gorka, A. Zawislak, J. Choma, M. Jaroniec, Applied Surface Science, 256 (2010) 5187-5190.

[63] X.Q. Wang, J.S. Lee, C. Tsouris, D.W. DePaoli, S. Dai, Journal of Materials Chemistry, 20 (2010) 4602-4608.

[64] W.M. Qiao, S.H. Yoon, I. Mochida, Energy & Fuels, 20 (2006) 1680-1684.

[65] P. Simon, Y. Gogotsi, Nature Materials, 7 (2008) 845-854.

[66] H. Nakamura, H. Komatsu, M. Yoshio, Journal of Power Sources, 62 (1996) 219-222.

[67] H. Yang, M. Yoshio, K. Isono, R. Kuramoto, Electrochemical and Solid State Letters, 5 (2002) A141-A144.

[68] P.W. Zhou, B.H. Li, F.Y. Kang, Y.Q. Zeng, New Carbon Materials, 21 (2006) 125-131.

[69] Y.T. Yu, C.J. Cui, W.Z. Qian, Q. Xie, C. Zheng, C.Y. Kong, F. Wei, Asia-Pacific Journal of Chemical Engineering, 8 (2013) 234-245.

[70] Q.F. Zhang, E. Uchaker, S.L. Candelaria, G.Z. Cao, Chemical Society Reviews, 42 (2013) 3127-3171.

[71] M.F.L. De Volder, S.H. Tawfick, R.H. Baughman, A.J. Hart, Science, 339 (2013) 535-539.

[72] S. Park, M. Vosguerichian, Z.A. Bao, Nanoscale, 5 (2013) 1727-1752.

[73] E. Frackowiak, K. Metenier, V. Bertagna, F. Beguin, Applied Physics Letters, 77 (2000) 2421-2423.

[74] E. Frackowiak, K. Jurewicz, S. Delpeux, F. Beguin, Journal of Power Sources, 97-8 (2001) 822-825.

[75] K.H. An, K.K. Jeon, W.S. Kim, Y.S. Park, S.C. Lim, D.J. Bae, Y.H. Lee, Journal of the Korean Physical Society, 39 (2001) S511-S517.

[76] S.W. Lee, D.K. Park, J.K. Lee, J.B. Ju, T.W. Sohn, Korean Journal of Chemical Engineering, 18 (2001) 371-375.

[77] B.J. Yoon, S.H. Jeong, K.H. Lee, H.S. Kim, C.G. Park, J.H. Han, Chemical Physics Letters, 388 (2004) 170-174.

[78] H.S. Ye, X. Liu, H.F. Cui, W.D. Zhang, F.S. Sheu, T.M. Lim, Electrochemistry Communications, 7 (2005) 249-255.

[79] C.G. Liu, H.T. Fang, F. Li, M. Liu, H.M. Cheng, Journal of Power Sources, 160 (2006) 758-761.

[80] R.R. Nair, P. Blake, A.N. Grigorenko, K.S. Novoselov, T.J. Booth, T. Stauber, N.M.R. Peres, A.K. Geim, Science, 320 (2008) 1308-1308.

[81] Y. Lee, J.H. Ahn, Nano, 8 (2013).

[82] A.K. Geim, K.S. Novoselov, Nature Materials, 6 (2007) 183-191.

[83] J.C. Meyer, A.K. Geim, M.I. Katsnelson, K.S. Novoselov, T.J. Booth, S. Roth, Nature, 446 (2007) 60-63.

[84] S. Stankovich, D.A. Dikin, G.H.B. Dommett, K.M. Kohlhaas, E.J. Zimney, E.A. Stach, R.D. Piner, S.T. Nguyen, R.S. Ruoff, Nature, 442 (2006) 282-286.

[85] H.A. Becerril, J. Mao, Z. Liu, R.M. Stoltenberg, Z. Bao, Y. Chen, Acs Nano, 2 (2008) 463-470.

[86] M. Hirata, T. Gotou, S. Horiuchi, M. Fujiwara, M. Ohba, Carbon, 42 (2004) 2929-2937.

[87] Y. Wang, Z.Q. Shi, Y. Huang, Y.F. Ma, C.Y. Wang, M.M. Chen, Y.S. Chen, Journal of Physical Chemistry C, 113 (2009) 13103-13107.

[88] Y. Chen, X.O. Zhang, D.C. Zhang, P. Yu, Y.W. Ma, Carbon, 49 (2011) 573-580.

[89] W. Lv, D.M. Tang, Y.B. He, C.H. You, Z.Q. Shi, X.C. Chen, C.M. Chen, P.X. Hou, C. Liu, Q.H. Yang, Acs Nano, 3 (2009) 3730-3736.

[90] L.W. Ji, Z. Lin, M. Alcoutlabi, X.W. Zhang, Energy & Environmental Science, 4 (2011) 2682-2699.

[91] F.Y. Cheng, J. Liang, Z.L. Tao, J. Chen, Advanced Materials, 23 (2011) 1695-1715.

[92] J. Jiang, Y.Y. Li, J.P. Liu, X.T. Huang, C.Z. Yuan, X.W. Lou, Advanced Materials, 24 (2012) 5166-5180.

[93] Y.G. Li, B. Tan, Y.Y. Wu, Nano Letters, 8 (2008) 265-270.

[94] L.J. Fu, H. Liu, C. Li, Y.P. Wu, E. Rahm, R. Holze, H.Q. Wu, Solid State Sciences, 8 (2006) 113-128.

[95] T. Fang, J.G. Duh, S.R. Sheen, Journal of the Electrochemical Society, 152 (2005) A1701-A1706.

[96] C.D. Lokhande, D.P. Dubal, O.S. Joo, Current Applied Physics, 11 (2011) 255-270.

[97] B.D. Desai, J.B. Fernandes, V.N.K. Dalal, Journal of Power Sources, 16 (1985) 1-43.

[98] N.L. Wu, S.L. Kuo, M.H. Lee, Journal of Power Sources, 104 (2002) 62-65.

[99] T.P. Gujar, V.R. Shinde, C.D. Lokhande, W.Y. Kim, K.D. Jung, O.S. Joo, Electrochemistry Communications, 9 (2007) 504-510.

[100] J.P. Zheng, P.J. Cygan, T.R. Jow, Journal of the Electrochemical Society, 142 (1995) 2699-2703.

[101] K. Lota, V. Khomenko, E. Frackowiak, Journal of Physics and Chemistry of Solids, 65 (2004) 295-301.

[102] M. Mastragostino, C. Arbizzani, F. Soavi, Journal of Power Sources, 97-8 (2001) 812-815.

[103] S.R. Sivakkumar, D.W. Kim, Journal of the Electrochemical Society, 154 (2007) A134-A139.

[104] S.R. Sivakkumar, D.R. MacFarlane, M. Forsyth, D.W. Kim, Journal of the Electrochemical Society, 154 (2007) A834-A838.

[105] S.R. Sivakkumar, R. Saraswathi, Journal of Power Sources, 137 (2004) 322-328.

[106] H. Talbi, P.E. Just, L.H. Dao, Journal of Applied Electrochemistry, 33 (2003) 465-473.

[107] K.S. Ryu, K.M. Kim, N.G. Park, Y.J. Park, S.H. Chang, Journal of Power Sources, 103 (2002) 305-309.

[108] T.C. Girija, M.V. Sangaranarayanan, Journal of Power Sources, 156 (2006) 705-711.

[109] S. Chaudhari, Y. Sharma, P.S. Archana, R. Jose, S. Ramakrishna, S. Mhaisalkar, M. Srinivasan, Journal of Applied Polymer Science, 129 (2013) 1660-1668.

[110] S.F. Shaikh, J.Y. Lim, R.S. Mane, M.K. Zate, S.H. Han, O.S. Joo, Journal of Applied Polymer Science, 128 (2013) 3660-3664.

[111] S. Suematsu, Y. Oura, H. Tsujimoto, H. Kanno, K. Naoi, Electrochimica Acta, 45 (2000) 3813-3821.

[112] W. Sun, X.Y. Chen, Journal of Power Sources, 193 (2009) 924-929.

[113] S. Lee, M.S. Cho, J.D. Nam, Y. Lee, Journal of Nanoscience and Nanotechnology, 8 (2008) 5036-5041.

[114] H.P. de Oliveira, S.A. Sydlik, T.M. Swager, Journal of Physical Chemistry C, 117 (2013) 10270-10276.

[115] A.L.M. Reddy, F.E. Amitha, I. Jafri, S. Ramaprabhu, Nanoscale Research Letters, 3 (2008) 145-151.

[116] C.J. Yu, C. Masarapu, J.P. Rong, B.Q. Wei, H.Q. Jiang, Advanced Materials, 21 (2009) 4793-+.

[117] L.B. Hu, J.W. Choi, Y. Yang, S. Jeong, F. La Mantia, L.F. Cui, Y. Cui, Proceedings of the National Academy of Sciences of the United States of America, 106 (2009) 21490-21494.

[118] M. Kaempgen, C.K. Chan, J. Ma, Y. Cui, G. Gruner, Nano Letters, 9 (2009) 1872-1876.

[119] Y.J. Kang, H. Chung, C.H. Han, W. Kim, Nanotechnology, 23 (2012).

[120] A. Izadi-Najafabadi, T. Yamada, D.N. Futaba, M. Yudasaka, H. Takagi, H. Hatori, S. Iijima, K. Hata, Acs Nano, 5 (2011) 811-819.

[121] M. Pasta, F. La Mantia, L.B. Hu, H.D. Deshazer, Y. Cui, Nano Research, 3 (2010) 452-458.

[122] Q. Wu, Y.X. Xu, Z.Y. Yao, A.R. Liu, G.Q. Shi, Acs Nano, 4 (2010) 1963-1970.

[123] S. Shi, C.J. Xu, C. Yang, J. Li, H.D. Du, B.H. Li, F.Y. Kang, Particuology, 11 (2013) 371-377.

[124] X.M. Feng, R.M. Li, Z.Z. Yan, X.F. Liu, R.F. Chen, Y.W. Ma, X.A. Li, Q.L. Fan, W. Huang, Ieee Transactions on Nanotechnology, 11 (2012) 1080-1086.

[125] L.Y. Yuan, X.H. Lu, X. Xiao, T. Zhai, J.J. Dai, F.C. Zhang, B. Hu, X. Wang, L. Gong, J. Chen, C.G. Hu, Y.X. Tong, J. Zhou, Z.L. Wang, Acs Nano, 6 (2012) 656-661.

[126] S. Giri, D. Ghosh, A. Malas, C.K. Das, Journal of Electronic Materials, 42 (2013) 2595-2605.

[127] A. Hagfeldt, G. Boschloo, L.C. Sun, L. Kloo, H. Pettersson, Chemical Reviews, 110 (2010) 6595-6663.

[128] B. Oregan, M. Gratzel, Nature, 353 (1991) 737-740.

[129] M. Gratzel, Nature, 414 (2001) 338-344.

[130] R. Jose, V. Thavasi, S. Ramakrishna, Journal of the American Ceramic Society, 92 (2009) 289-301.

[131] S.K. Balasingam, M. Lee, M.G. Kang, Y. Jun, Chemical Communications, 49 (2013) 1471-1487.

[132] H.H. Deng, Z.H. Lu, H.F. Mao, H.J. Xu, Chemical Physics, 221 (1997) 323-331.

[133] K. Lee, S.W. Park, M.J. Ko, K. Kim, N.G. Park, Nature Materials, 8 (2009) 665-671.

[134] F.Z. Huang, D.H. Chen, L. Cao, R.A. Caruso, Y.B. Cheng, Energy & Environmental Science, 4 (2011) 2803-2806.

[135] M. Durr, A. Bamedi, A. Yasuda, G. Nelles, Applied Physics Letters, 84 (2004) 3397-3399.

[136] M. Murayama, T. Mori, Journal of Physics D-Applied Physics, 40 (2007) 1664-1668.

[137] J. Zhang, N. Jiang, Z. Dang, T.J. Elder, A.J. Ragauskas, Cellulose, 15 (2008) 489-496.

[138] L. Yan, H. Tao, P.R. Bangal, Clean-Soil Air Water, 37 (2009) 39-44.

[139] M. Henriksson, G. Henriksson, L.A. Berglund, T. Lindstrom, European Polymer Journal, 43 (2007) 3434-3441.

[140] K. Syverud, P. Stenius, Cellulose, 16 (2009) 75-85.

[141] H.D. Abruna, Y. Kiya, J.C. Henderson, Physics Today, 61 (2008) 43-47.

[142] J.M. Miller, B. Dunn, T.D. Tran, R.W. Pekala, Journal of the Electrochemical Society, 144 (1997) L309-L311.

[143] H. Nishide, K. Oyaizu, Science, 319 (2008) 737-738.

[144] J.Q. Geng, J.P. Bonnet, S. Renault, F. Dolhem, P. Poizot, Energy & Environmental Science, 3 (2010) 1929-1933.

[145] J.M. Tarascon, M. Armand, Nature, 414 (2001) 359-367.

[146] S. Hu, R. Rajamani, X. Yu, Applied Physics Letters, 100 (2012).

[147] Q.A. Liu, M.H. Nayfeh, S.T. Yau, Journal of Power Sources, 195 (2010) 7480-7483.

[148] L.Y. Yuan, X. Xiao, T.P. Ding, J.W. Zhong, X.H. Zhang, Y. Shen, B. Hu, Y.H. Huang, J. Zhou, Z.L. Wang, Angewandte Chemie-International Edition, 51 (2012) 4934-4938.

[149] T.I. Lee, J.P. Jeagal, J.H. Choi, W.J. Choi, M.J. Lee, J.Y. Oh, K.B. Kim, H.K. Baik, Y.N. Xia, J.M. Myoung, Advanced Materials, 23 (2011) 4711-+.

[150] V. Di Noto, M. Vittadello, S. Lavina, M. Fauri, S. Biscazzo, Journal of Physical Chemistry B, 105 (2001) 4584-4595.

[151] A. Liivat, D. Brandell, J.O. Thomas, Journal of Materials Chemistry, 17 (2007) 3938-3946.

[152] A. Maitra, A. Heuer, Physical Review Letters, 98 (2007).

[153] Y. Aihara, G.B. Appetecchi, B. Scrosati, Journal of the Electrochemical Society, 149 (2002) A849-A854.

[154] D. Diddens, A. Heuer, O. Borodin, Macromolecules, 43 (2010) 2028-2036.

[155] V.L. Pushparaj, M.M. Shaijumon, A. Kumar, S. Murugesan, L. Ci, R. Vajtai, R.J. Linhardt, O. Nalamasu, P.M. Ajayan, Proceedings of the National Academy of Sciences of the United States of America, 104 (2007) 13574-13577.

[156] W. Zhang, X.D. Zhang, C.H. Lu, Y.J. Wang, Y.L. Deng, Journal of Physical Chemistry C, 116 (2012) 9227-9234.

[157] R. Martins, I. Ferreira, E. Fortunato, Physica Status Solidi-Rapid Research Letters, 5 (2011) 332-335.

[158] D. Tobjork, R. Osterbacka, Advanced Materials, 23 (2011) 1935-1961.

[159] G. Lota, K. Fic, E. Frackowiak, Energy & Environmental Science, 4 (2011) 1592-1605.

[160] R.H. Baughman, A.A. Zakhidov, W.A. de Heer, Science, 297 (2002) 787-792.

[161] B. Kim, H. Chung, W. Kim, Journal of Physical Chemistry C, 114 (2010) 15223-15227.

[162] J. Bae, M.K. Song, Y.J. Park, J.M. Kim, M.L. Liu, Z.L. Wang, Angewandte Chemie-International Edition, 50 (2011) 1683-1687.

[163] H.J. In, S. Kumar, Y. Shao-Horn, G. Barbastathis, Applied Physics Letters, 88 (2006).

[164] G.Y. Zheng, L.B. Hu, H. Wu, X. Xie, Y. Cui, Energy & Environmental Science, 4 (2011) 3368-3373.

[165] F.D.S. Larotonda, K.S. Matsui, S.S. Paes, J.B. Laurindo, Starch - Stärke, 55 (2003) 504-510.

[166] K. Matsui, Carbohydrate Polymers, 55 (2004) 237-243.

[167] S.R. Forrest, Nature, 428 (2004) 911-918.

[168] J.A. Rogers, T. Someya, Y.G. Huang, Science, 327 (2010) 1603-1607.

[169] G.A. Snook, P. Kao, A.S. Best, Journal of Power Sources, 196 (2011) 1-12.

[170] Y. Jin, H.Y. Chen, M.H. Chen, N. Liu, Q.W. Li, Acta Physico-Chimica Sinica, 28 (2012) 609-614.

[171] M. Berggren, D. Nilsson, N.D. Robinson, Nature Materials, 6 (2007) 3-5.

[172] Y. Liu, S. Gorgutsa, C. Santato, M. Skorobogatiy, Journal of the Electrochemical Society, 159 (2012) A349-A356.

[173] S.J. Eichhorn, Soft Matter, 7 (2011) 303-315.

[174] S.J. Eichhorn, A. Dufresne, M. Aranguren, N.E. Marcovich, J.R. Capadona, S.J. Rowan, C. Weder, W. Thielemans, M. Roman, S. Renneckar, W. Gindl, S. Veigel, J. Keckes, H. Yano, K. Abe, M. Nogi, A.N. Nakagaito, A. Mangalam, J. Simonsen, A.S. Benight, A. Bismarck, L.A. Berglund, T. Peijs, Journal of Materials Science, 45 (2010) 1-33.

[175] A. Razaq, L. Nyholm, M. Sjodin, M. Stromme, A. Mihranyan, Advanced Energy Materials, 2 (2012) 445-454.

[176] W. Chen, R.B. Rakhi, L.B. Hu, X. Xie, Y. Cui, H.N. Alshareef, Nano Letters, 11 (2011) 5165-5172.

[177] M. Paakko, J. Vapaavuori, R. Silvennoinen, H. Kosonen, M. Ankerfors, T. Lindstrom, L.A. Berglund, O. Ikkala, Soft Matter, 4 (2008) 2492-2499.

[178] W. Zhang, Y. Zhang, C.H. Lu, Y.L. Deng, Journal of Materials Chemistry, 22 (2012) 11642-11650.

[179] W.H. Chung, H.J. Hwang, S.H. Lee, H.S. Kim, Nanotechnology, 24 (2013).

[180] K. Ankireddy, S. Vunnam, J. Kellar, W. Cross, Journal of Materials Chemistry C, 1 (2013) 572-579.

[181] S. Nam, H.W. Cho, S. Lim, D. Kim, H. Kim, B.J. Sung, Acs Nano, 7 (2013) 851-856.

[182] J.J. Wu, N. Zhao, X.L. Zhang, J. Xu, Cellulose, 19 (2012) 1239-1249.

[183] G. Yang, J.J. Xie, Y.X. Deng, Y.G. Bian, F. Hong, Carbohydrate Polymers, 87 (2012) 2482-2487.

[184] M. Montazer, F. Alimohammadi, A. Shamei, M.K. Rahimi, Carbohydrate Polymers, 87 (2012) 1706-1712.

[185] G. Yang, J.J. Xie, F. Hong, Z.J. Cao, X.X. Yang, Carbohydrate Polymers, 87 (2012) 839-845.

[186] G.N. Zhang, L. Zheng, M. Zhang, S.H. Guo, Z.H. Liu, Z.P. Yang, Z.L. Wang, Energy & Fuels, 26 (2012) 618-623.

[187] J.C. Huang, H.B. Wu, D.X. Cao, G.L. Wang, Electrochimica Acta, 75 (2012) 208-212.

[188] Y. Yang, S.M. Liu, K. Kimura, Angewandte Chemie-International Edition, 45 (2006) 5662-5665.

[189] M. Sawangphruk, T. Kaewsongpol, Materials Letters, 87 (2012) 142-145.

[190] Y. Gao, D.C. Shan, F. Cao, J. Gong, X. Li, H.Y. Ma, Z.M. Su, L.Y. Qu, Journal of Physical Chemistry C, 113 (2009) 15175-15181.

[191] U. Bach, D. Lupo, P. Comte, J.E. Moser, F. Weissortel, J. Salbeck, H. Spreitzer, M. Gratzel, Nature, 395 (1998) 583-585.

[192] E.J.W. Crossland, N. Noel, V. Sivaram, T. Leijtens, J.A. Alexander-Webber, H.J. Snaith, Nature, 495 (2013) 215-219.

[193] A. Yella, H.W. Lee, H.N. Tsao, C.Y. Yi, A.K. Chandiran, M.K. Nazeeruddin, E.W.G. Diau, C.Y. Yeh, S.M. Zakeeruddin, M. Gratzel, Science, 334 (2011) 629-634.

[194] M.D. Ye, D.J. Zheng, M.Q. Lv, C. Chen, C.J. Lin, Z.Q. Lin, Advanced Materials, 25 (2013) 3039-3044.

[195] M.D. Ye, H.Y. Liu, C.J. Lin, Z.Q. Lin, Small, 9 (2013) 312-321.

[196] Y.H. Jang, X.K. Xin, M. Byun, Y.J. Jang, Z.Q. Lin, D.H. Kim, Nano Letters, 12 (2012) 1742-1742.

[197] J. Wang, Z.Q. Lin, Chemistry-an Asian Journal, 7 (2012) 2754-2762.

[198] X.K. Xin, J. Wang, W. Han, M.D. Ye, Z.Q. Lin, Nanoscale, 4 (2012) 964-969.

[199] J. Wang, Z.Q. Lin, Chemistry of Materials, 22 (2010) 579-584.

[200] M.D. Ye, X.K. Xin, C.J. Lin, Z.Q. Lin, Nano Letters, 11 (2011) 3214-3220.

[201] X.K. Xin, M. He, W. Han, J.H. Jung, Z.Q. Lin, Angewandte Chemie-International Edition, 50 (2011) 11739-11742.

[202] C.H. Siu, C.L. Ho, J. He, T. Chen, X.N. Cui, J.Z. Zhao, W.Y. Wong, Journal of Organometallic Chemistry, 748 (2013) 75-83.

[203] N. Humphry-Baker, K. Driscoll, A. Rao, T. Torres, H.J. Snaith, R.H. Friend, Nano Letters, 12 (2012) 634-639.

[204] J. Chang, C.P. Lee, D. Kumar, P.W. Chen, L.Y. Lin, K.R.J. Thomas, K.C. Ho, Journal of Power Sources, 240 (2013) 779-785.

[205] C.L. Lee, W.H. Lee, C.H. Yang, Journal of Materials Science, 48 (2013) 3448-3453.

[206] G.D. Sharma, M.K. Panda, M.S. Roy, J.A. Mikroyannidis, E. Gad, A.G. Coutsolelos, Journal of Renewable and Sustainable Energy, 5 (2013).

[207] N.C. Jeong, H.J. Son, C. Prasittichai, C.Y. Lee, R.A. Jensen, O.K. Farha, J.T. Hupp, Journal of the American Chemical Society, 134 (2012) 19820-19827.

[208] C. Magne, M. Urien, T. Pauporte, Rsc Advances, 3 (2013) 6315-6318.

[209] V. Saxena, P. Veerender, A.K. Chauhan, P. Jha, D.K. Aswal, S.K. Gupta, Applied Physics Letters, 100 (2012).

[210] G.D. Sharma, S.P. Singh, R. Kurchania, R.J. Ball, Rsc Advances, 3 (2013) 6036-6043.

[211] H. Choi, S. Kim, S.O. Kang, J.J. Ko, M.S. Kang, J.N. Clifford, A. Forneli, E. Palomares, M.K. Nazeeruddin, M. Gratzel, Angewandte Chemie-International Edition, 47 (2008) 8259-8263.

[212] C.M. Lan, H.P. Wu, T.Y. Pan, C.W. Chang, W.S. Chao, C.T. Chen, C.L. Wang, C.Y. Lin, E.W.G. Diau, Energy & Environmental Science, 5 (2012) 6460-6464.

[213] K.M. Lee, Y.C. Hsu, M. Ikegami, T. Miyasaka, K.R.J. Thomas, J.T. Lin, K.C. Ho, Journal of Power Sources, 196 (2011) 2416-2421.

[214] F. Inakazu, Y. Noma, Y. Ogomi, S. Hayase, Applied Physics Letters, 93 (2008).

[215] Z.M. Beiley, M.D. McGehee, Energy & Environmental Science, 5 (2012) 9173-9179.

[216] W.S. Jeong, J.W. Lee, S. Jung, J.H. Yun, N.G. Park, Solar Energy Materials and Solar Cells, 95 (2011) 3419-3423.

[217] J. Usagawa, S.S. Pandey, S. Hayase, M. Kono, Y. Yamaguchi, Applied Physics Express, 2 (2009).

[218] Q.Q. Miao, L.Q. Wu, J.N. Cui, M.D. Huang, T.L. Ma, Advanced Materials, 23 (2011) 2764-2768.

[219] M. Adachi, M. Sakamoto, J.T. Jiu, Y. Ogata, S. Isoda, Journal of Physical Chemistry B, 110 (2006) 13872-13880.

[220] M.G. Kang, N.G. Park, K.S. Ryu, S.H. Chang, K.J. Kim, Chemistry Letters, 34 (2005) 804-805.

[221] L.J. Meng, M.X. Wu, Y.M. Wang, W. Guo, C.Y. Ma, T.L. Ma, R. Silva, Applied Surface Science, 275 (2013) 222-226.

[222] F.Y. Ouyang, W.L. Tai, Applied Surface Science, 276 (2013) 563-570.